Charging Mechanisms of Surfactant Doped Nonpolar Liquids

Submitted in partial fulfillment of the requirements for

the degree of

Doctor of Philosophy

in

Department of Engineering

Keyi Xu

B.S., Chemical Engineering, University of Delaware

Carnegie Mellon University
Pittsburgh, PA

August 2020

ACKNOWLEDGEMENTS

I would like to thank my advisors Dennis Prieve, Jim Schneider, and Paul Sides. Without their efforts, I would not have received such a well-rounded or comprehensive PhD education. The birth of this thesis, which required 5 years of gestation, has been challenging but ultimately informative to the development of my scientific ideals. Thanks also to Lynn Walker for her compassionate advice and advocacy throughout my PhD studies.

This thesis has been enriched from the comments and feedback of my committee members Bob Tilton, Aditya Khair, and Reeja Jayan. I greatly appreciate their time and investment in my work throughout the years. I also gratefully acknowledge my funding source NSF Grant ##1511619.

Thanks to my past and present colleagues in the Prieve/Schneider research groups, CFE lab, and greater ChemE PhD student body from whom I have received countless technical and scientific insights. I am indebted to the collaborative atmosphere at CMU which has catalyzed many fruitful partnerships essential to the success of this project. I give my grateful acknowledgements to my undergraduate researchers Katrina Wong, Eileen Kim, Emma Moliter, and Joe Brauch, who have each borne the brunt of endless organic syntheses for the past 3 years with graceful enthusiasm and intellectual curiosity.

To my friends and family, who have accompanied me through the woes and triumphs of research, I express my sincerest gratitude. My utmost solidarity to my eternal comrade Rose Sun for her unwavering support and kind ear. Finally, thanks to my beloved husband Garth Devlin who had enough faith in me to carry the both of us. I

look forward towards a new chapter in our life together.

ABSTRACT

Impedance spectroscopy has been used in the literature to elucidate the charging mechanisms of inverses micelles in surfactant doped dodecane solutions. However, the existing literature has been limited in surfactant scope due to instrumental complications and surfactant purity issues. Charge adsorption on the electrode surface may obscure measurement of the double layer capacitance and hence the ionic strength.(JCIS, 449, 2-12, 2015) This charge adsorption phenomenon effectively limits the concentration range and catalog of surfactants available to the impedance spectroscopy method.(JCIS, 469, 325-337, 2016) A passivating coating of plasma polymerized octafluorocyclobutane is fabricated and determined to successfully suppress charge adsorption. An equivalent circuit representing the surfactant solution and fluoropolymer coating is derived and used to model and interpret the impedance spectra. The circuit model is determined to capture most of the experiment charge transfer processes with the exception of a small instrumental artifact at low frequencies. Analysis of the impedance spectra for Span-20, Span-80, and Span-85 in dodecane demonstrates dependency of charged micelle size on surfactant HLB number.

Charge formation in nonpolar liquids of commercial surfactants have been extensively studied in the literature; however, these surfactants are often of low purity and lack systematic changes in chemical structure. A flexible synthetic technique is developed and used to produce high-purity AOT analog surfactants with a systematic change in counterion chemistry. The charging properties of these AOT analogs are studied using impedance spectroscopy and compared to bulk micelle properties obtained from small angle neutron scattering (SANS) and dynamic light scattering

(DLS). Measured conductivity and ionic strength values for analog surfactants were an order of magnitude than those of sodium AOT despite forming micelles of similar size. This increased affinity for charged micelle formation cannot be modeled by commonly used disproportionation or charge fluctuation theories for micelle formation in nonpolar media and reveals new relationships between counterion chemistry and micelle charging not seen in commercial surfactants.

Following successful impedance spectroscopy characterization of AOT analogs, we synthesize additional surfactants of high purity and incrementally altered head groups, counterions and hydrocarbon tail chemistries. Then using electrochemical impedance spectroscopy, we identify specific chemical structures that promote charging in nonpolar liquids. These trends are contrasted with dynamic light scattering studies and highlight the pitfalls of inferring electrical properties from scattering results. Impedance spectroscopy experiments reveal that ion-pair dissociation is the chemical property essential to prediction of reverse micelle charging in nonpolar liquids for both ionic and nonionic surfactants.

Finally, we measure the zeta potential of mica and fluoropolymer surfaces immersed in solutions of synthesized surfactant using Zetaspin^{TM}. Such experiments aimed to deduce relationships between surfactant chemistry and surface charging in nonpolar liquids. The charge of mica surfaces was found to be positive in sign and highly dependent on the presence of water (from the ambient air) as well as contact time between the surface and surfactant solution. The sign and magnitude of charging of fluoropolymer surfaces was dependent on surfactant structure.

TABLE OF CONTENTS

LIST OF TABLES

LIST OF FIGURES

Chapter 1 Introduction to charging in surfactant doped nonpolar liquids

1.1 Introduction

Stability of particle suspensions in nonpolar liquids is vital to many industrial applications such as electrophoretic displays,[1,2] control of particle aggregation in tar sands,[3] preventing soot build up in engines,[4] and formulation stability in pharmaceutical products.[5] One method of ensuring particle repulsion and stability is through electrostatic repulsion from charging of the particle surface.[6] While surface charging is well understood in aqueous systems, the mechanisms of surface charging and charge formation in nonpolar liquids remain ambiguous. For industrial use, charging agents in nonpolar liquids are typically chosen on an ad-hoc basis through trial and error. As a result, the development of models to rationalize charging in nonpolar liquids is of great commercial interest. Such models would establish design rules for charging agents in commercial formulations. Examples of models discussed in the literature include charge fluctuation theory,[7,8] radial distribution functions,[9] acid-base interactions,[10–12] ion dissociation,[13] and the presence of ionic impurities[14].

One method of charging nonpolar liquids is through the additional of surfactant. These surfactants aggregate into inverse micelles with the polar head groups associated in a central core and hydrocarbon tails pointing outwards. Reverse micelles allow water and other ionic species to be solvated in the polar core, increasing the conductivity and charge stability of the solutions.[4] Literature experiments have found correlations between reverse micelle size and its ability to stabilize charge.[15,16] Because of this, scattering has been a popular method to obtain size information on reverse micelles in nonpolar media. However, scattering experiments cannot distinguish

between charged and uncharged surfactants. Another method to determine micelle size is through measurement of the Debye length using techniques such as total internal reflection microscopy (TIRM)[17] or atomic force microscopy[18]. Unfortunately, TIRM and AFM can only be used for specific surfactant-solvent systems due to buoyance issues with the levitated particle.

Electrochemical experiments are sensitive to only charged species and can be applied to a variety of surfactant-solvent systems. In these experiments, either a direct or alternating current is applied to the surfactant solution to probe time rates for charge migration inside the solution. In direct current (DC) current experiments, the transient current is measured after a step change in voltage. Integration of the transient current with time is equal to the ionic strength of solution.[19,20] In alternating (AC) current experiments such as impedance spectroscopy, the ionic strength is determined from the double layer of charge assembled next to each electrode.[15,16] DC and AC experiments have been used to characterize a wide variety of surfactants; however, undesirable electrode effects complicate and occasional completely obscure measurement of the ionic strength. In AC experiments, the existence of a persistent surface current increases the error of the integration analysis[19–22] while in DC experiments, charge adsorption sometimes prevents measurement of the double layer[15].

In Chapter 2, we resolve the undesirable electrode surface effects by fabricating a fluoropolymer coating. Through observing the disappearance of impedance spectra features characteristic of charge adsorption, we verify that the fluoropolymer is able to suppress all charge adsorption during the impedance experiment. The passivating coating is then used to expand the impedance experiments of Yezer to concentrations

and surfactants previously unfeasible for impedance spectroscopy.[15] The ionic strength, conductivity, and charged micelle size of the commercial surfactants Span-20, Span-80, and Span-85 are compared based on surfactant chemistry and ability for charge stabilization.

Another obstacle to charged characterization of charged micelles in nonpolar liquids is the low purity of commercial surfactants. For example, the conductivity of Span surfactants (sorbitan esters) are thought to arise from charged impurities in the formulation.[23] Using the synthesis technique described in Chapter 3, we were able to produce high-purity surfactants with incremental changes in surfactant chemistry. In Chapter 3, we narrow the focus of our experiments to purified commercial surfactant sodium AOT (diotcyl sodium sulfosuccinate) and two synthesized homologs $(C_8b)_2$-Asp-PTS and $(C_8b)^2$-Glu-PTS whose structures are shown in Chapter 3. Impedance spectroscopy of these experiments demonstrate that the AOT homologs were an order of magnitude more conductive than AOT in dodecane. The AOT homologs formed an order of magnitude more charged micelles than AOT. This result contradicted the commonly used charge fluctuation model of micelle charging first proposed by Eicke.[7] According to the charge fluctuation model, the probability of micelle charging is based solely on micelle size. Thus, two different micelles of the same size should have similar conductivities. In the case of the AOT homologs, they formed micelles of the same size as AOT but had ionic strengths an order of magnitude higher than AOT. Such charging trends are conjectured to arise from differences in counterion chemistry between AOT and its analogs.

Chapter 4 further expands upon the results of Chapter 3 by exploring charging

trends amongst a wider range of surfactant chemistries using impedance spectroscopy and dynamic light scattering. Surfactants were synthesized using modified recipes of the chemical reaction process introduced in Chapter 3 as well as a new procedure involving ion exchange. The synthesized surfactants were categorized based on three groups. The first group of surfactants varied only in the dissociability of the head group while maintaining the same tail chemistry. The second group of surfactants varied in tail length and degree of branching. The final group of surfactants compared the charging behavior of univalent and divalent counterions of the same surfactant structure. The solubility, micelle assembly, and charged micelle formation behavior of all three groups of surfactants differed from each other. Solubility and conductivity in dodecane was found to increase with head group dissociability. Tail group branching was determined to be essential for surfactant solubility in nonpolar liquids as confirmed by results from literature.[24] However, not all micelle solutions were conductive despite being soluble, a trend not seen in the existing nonpolar literature of surfactants.[4,6] Finally, univalent and divalent counterions formed solutions of similar ionic strength but different micelle aggregation schemes and hygroscopicity.

Chapter 5 expands upon the earlier chapters by expanding the study of surfactant solution charging to that of surface charging. Zetaspin™ experiments were conducted on the surfactants discussed in Chapters 3 and 4 to determine their ability to charge fluoropolymer and mica surfaces. Zetaspin™ is an apparatus for determining the zeta potential of planar solids contacting surfactant doped nonpolar liquids. The streaming potential arising from a rotating disc sample of mica or fluoropolymer is measured using two glassy carbon electrodes.[25] The streaming potential is then used to

calculate the surface zeta potential given conductivity information about the solution.[25] The effect of water and surface to solution contact time is also explored and determined to have strong effects on the measured zeta potential. Finally, the acid-base interaction theory adapted by Behrens from Fowkes is used to rationalize charging trends amongst the surfaces and surfactants.[26–29]

1.2 References

(1) Chen, Y.; Au, J.; Kazlas, P.; Ritenour, a; Gates, H.; McCreary, M. Electronic Paper: Flexible Active-Matrix Electronic Ink Display. *Nature* **2003**, *423* (6936), 136.

(2) Comiskey, B.; Albert, J. D.; Yoshizawa, H.; Jacobson, J. An Electrophoretic Ink for All-Printed Reflective Electronic Displays. *Nature* **1998**, *394* (6690), 253–255.

(3) Nikakhtari, H.; Vagi, L; Choi, P.; Liu, Q.; Gray, M. R.; Univ, A. Solent Screening For Non-Aqueous Extraction of Alberta Oil Sands. *Can. J. Chem. Eng.* **2013**, *91* (6), 1153–1160.

(4) Morrison, I. D. Electrical Charges in Nonaqueous Media. *Colloids and Surfaces A: Physicochemical and Engineering Aspects*. 1993, pp 1–37.

(5) Jones, S. A.; Martin, G. P.; Brown, M. B. Manipulation of Beclomethasone-Hydrofluoroalkane Interactions Using Biocompatible Macromolecules. *J. Pharm. Sci.* **2006**, *95* (5), 1060–1074.

(6) Smith, G. N.; Eastoe, J. Controlling Colloid Charge in Nonpolar Liquids with Surfactants. *Phys. Chem. Chem. Phys.* **2012**, 424–439.

(7) Eicke, H. F.; Borkovec, M.; Das-Gupta, B. Conductivity of Water-in-Oil Microemulsions: A Quantitative Charge Fluctuation Model. *J. Phys. Chem.* **1989**, *93* (1), 314–317.

(8) Hall, D. G. Conductivity of Microemulsions: An Improved Charge Fluctuation Model. *J. Phys. Chem.* **1990**.

(9) Espinosa, C. E.; Guo, Q.; Singh, V.; Behrens, S. H. Particle Charging and Charge Screening in Nonpolar Dispersions with Nonionic Surfactants. *Langmuir* **2010**.

(10) Liu, H.; Wang, S.; Xiao, Y.; Yang, Q.; Li, X. Charging Behavior of Carbon Black in a Low-Permittivity Medium Based on Acid-Base Charging Theory. *J. Mater. Chem. C* **2015**, *3* (16).

(11) Gacek, M. M.; Berg, J. C. The Role of Acid-Base Effects on Particle Charging in Apolar Media. *Adv. Colloid Interface Sci.* **2015**, *220*, 108–123.

(12) Poovarodom, S.; Berg, J. C. Effect of Particle and Surfactant Acid-Base Properties on Charging of Colloids in Apolar Media. *J. Colloid Interface Sci.* **2010**, *346* (2), 370–377.

(13) Kemp, R.; Sanchez, R.; Mutch, K. J.; Bartlett, P. Nanoparticle Charge Control in Nonpolar Liquids: Insights from Small-Angle Neutron Scattering and Microelectrophoresis. *Langmuir* **2010**.

(14) Klinkenberg, A.; Leonard van der Minne, J. *Electrostatics in the Petroleum Industry: The Prevention of Explosion Hazards*; Elsevier, 1958.

(15) Yezer, B. A.; Khair, A. S.; Sides, P. J.; Prieve, D. C. Determination of Charge Carrier Concentration in Doped Nonpolar Liquids by Impedance Spectroscopy in the Presence of Charge Adsorption. *J. Colloid Interface Sci.* **2016**, *469*, 325–337.

(16) Yezer, B. A.; Khair, A. S.; Sides, P. J.; Prieve, D. C. Use of Electrochemical Impedance Spectroscopy to Determine Double-Layer Capacitance in Doped Nonpolar Liquids. *J. Colloid Interface Sci.* **2015**, *449*, 2–12.

(17) Prieve, D. C.; Hoggard, J. D.; Fu, R.; Sides, P. J.; Bethea, R. Two Independent Measurements of Debye Lengths in Doped Nonpolar Liquids. *Langmuir* **2008**, *24* (4), 1120–1132.

(18) Kumar, B.; Crittenden, S. R. Stern Potential and Debye Length Measurements in Dilute Ionic Solutions with Electrostatic Force Microscopy. *Nanotechnology* **2013**, *24* (43), 435701.

(19) Strubbe, F.; Verschueren, A. R. M.; Schlangen, L. J. M.; Beunis, F.; Neyts, K. Generation Current of Charged Micelles in Nonaqueous Liquids: Measurements and Simulations. *J. Colloid Interface Sci.* **2006**, *300* (1), 396–403.

(20) Strubbe, F.; Prasad, M.; Beunis, F. Characterizing Generated Charged Inverse Micelles with Transient Current Measurements. *J. Phys. Chem. A* **2015**, *119* (5).

(21) Karvar, M.; Strubbe, F.; Beunis, F.; Kemp, R.; Smith, N.; Goulding, M.; Neyts, K. Charging Dynamics of Aerosol OT Inverse Micelles. *Langmuir* **2015**, *31* (40), 10939–10945.

(22) Beunis, F.; Strubbe, F.; Karvar, M.; Drobchak, O.; Brans, T.; Neyts, K.; Verschueren, A. R. M. Electric Charging of Inverse Micelles in a Nonpolar Liquid with Surfactant. *Colloids Surfaces A Physicochem. Eng. Asp.* **2014**, *440*, 10–19.

(23) Dukhin, A.; Parlia, S. Ions, Ion Pairs and Inverse Micelles in Non-Polar Media.

Curr. Opin. Colloid Interface Sci. **2013**, *18* (2), 93–115.

(24) Nave, S.; Eastoe, J.; Heenan, R. K.; Steytler, D.; Grillo, I. What Is so Special about Aerosol-OT? 2. Microemulsion Systems. *Langmuir* **2000**, *16* (23), 8741–8748.

(25) Yezer, B. A. Determination of Charge Concentration in Surfactant Doped Nonpolar Liquids, Carnegie Mellon University, 2016.

(26) Fowkes, F. M. Role of Acid-Base Interfacial Bonding in Adhesion. *J. Adhes. Sci. Technol.* **1987**.

(27) Guo, Q.; Lee, J.; Singh, V.; Behrens, S. H. Surfactant Mediated Charging of Polymer Particles in a Nonpolar Liquid. *J. Colloid Interface Sci.* **2013**.

(28) Lee, J.; Zhou, Z. L.; Alas, G.; Behrens, S. H. Mechanisms of Particle Charging by Surfactants in Nonpolar Dispersions. *Langmuir* **2015**.

(29) Lee, J.; Zhou, Z. L.; Behrens, S. H. Charging Mechanism for Polymer Particles in Nonpolar Surfactant Solutions: Influence of Polymer Type and Surface Functionality. *Langmuir* **2016**, *32* (19).

Chapter 2 Suppression of charge adsorption in impedance spectroscopy of surfactant-doped nonpolar liquids

2.1 Introduction

Surface charging in nonpolar liquids is required for a myriad of technologies such as electrically driven transport of pigment particles in e-reader displays,[1,2] control of petrochemical particle aggregation in tar sands,[3] and stabilization of active pharmaceutical ingredients in drug delivery applications.[4] While surface charging in aqueous solutions is well understood, the mechanisms for charge formation and surface charging in nonpolar solvents remain nebulous. Charge fluctuation theory,[5] radial distribution functions,[6] acid-base interactions,[7–9] ion dissociation,[10] and the presence of charged impurities[11] have all been used to model charging in nonpolar liquids.

Electroneutrality dictates that surface charging of particles must be balanced by equal and opposite charge carriers in the fluid, but the identity of these charge carriers is often ambiguous.[12] One vehicle for charge formation in nonpolar liquids is addition of surfactant. In organic solvents, surfactant molecules aggregate into inverse micelles with polar head groups associated in the central core and hydrocarbon chains extending outwards. Water and other sources of charge are sequestered into the polar cores, increasing the conductivity and degree of charge stability of the solution.[13] Beyond inverse micelles,[13] weak organic acids,[14] microemulsions of water,[5] ions,[15] and other impurities[11] are several other examples of charge carriers that can raise the conductivity of nonpolar media. These charged species can be differentiated and thus identified based on size. Historically, scattering techniques have been used to determine the size and thus identity of charge carriers,[9,16] but such experiments cannot distinguish

between charged and uncharged scatterers. Alternatively, one can isolate charge carrier size from conductivity data given ionic strength information. Ionic strength can be inferred from the Debye length with techniques such as total internal reflection microscopy (TIRM)[17] or atomic force microscopy[18]; however, the exponential decay of repulsive double-layer forces can only be measured if the forces are sufficient to levitate the particle above the substrate. Radial-distribution-function experiments are similarly restricted to specific charge carrier-solvent systems due to this particle buoyancy issue.[6]

Electrochemical experiments are a more straightforward method of determining ionic strength and size of charge carriers in nonpolar liquids. In these methods, either a direct or alternating current is applied to probe characteristic timescales of charge transfer. In direct current (DC) experiments, the transient current is measured after a step change in voltage; once all charge carriers in the bulk are exhausted, one can integrate the current with time to determine the total charge concentration. [17,19–21] In alternating current (AC) experiments such as impedance spectroscopy, the charge concentration is inferred from measuring the double layer of charge that assembles next to the electrode plates.[22,23] Despite the experimental ease of AC and DC experiments, modeling and thus interpretation of the data is often difficult or impossible due to undesirable electrode surface effects. In DC experiments, persistence of an electrode "surface current" complicates the integration analysis [24–27]. In AC impedance spectroscopy experiments, there is a competitive balance between the charge carrier adsorption rate and diffusive transport rate.[23] The adsorption rate describes how fast charge carriers in the double layer are adsorbed onto the electrode surface while the diffusive transport rate indicates how fast charge carriers in the bulk can replenish the

double layer. Yezer[23] found that in order to clearly resolve the double layer, the diffusive transport rate must be at least 10 times faster than the adsorption rate. As a result, charge carriers that aggressively absorb onto the electrode surface cannot be studied using DC or AC electrochemical techniques, considerably narrowing the sample systems applicable for study.

In the present work, we describe a passivating coating for electrode surfaces that improves the resolution and sample accessibility of impedance spectroscopy for surfactant doped nonpolar liquids. Deposition and surface treatment techniques involving oxalic acid,[28] tartaric acid,[28] aluminum oxide (Al_2O_3),[24,27,29–31] and polytetrafluoroethylene[32] have been shown to create passivating buffer layers on indium tin oxide electrodes. In particular, Al_2O_3 coatings on ITO electrodes has been used in potentiostatic, DC experiments of surfactants in nonpolar liquids with partial success.[24,27] Our impedance experiments of Span-80 doped dodecane on a 33 nm thickness layer of Al_2O_3 on ITO corroborate this partial suppression of undesirable electrode surface behavior. In contrast, impedance experiments on a coating consisting of plasma polymerized C_4F_8 was determined to completely suppress all charge adsorption effects at the electrode surface. This choice of coating was informed by prior expertise in our group with fluoropolymer as an electrically passive sealant for nonpolar solutions. The passivating coating is applied via plasma deposition of octafluorocyclobutane (C_4F_8) which is mainly utilized as a deposition as well as cleaning gas on silicon surfaces.[33–37]. Because the fluoropolymer coating was found to degrade with repeated use, the coating thickness was fabricated at the upper limitation of the STS Multiplex DRIE ICP system so as to maximize coating homogeneity and durability

over time. To evaluate the effectiveness of the passivating coating, we expand upon the impedance spectroscopy study of commercial surfactants Span-20, Span-80, and Span-85 by Yezer et al.[23]

By observing the disappearance of phenomenon at charge transfer timescales characteristic of charge adsorption, we verify the success of the fluoropolymer coating. We verify this qualitatively as the disappearance of the second semicircle in the Nyquist plot on the fluoropolymer coated electrodes. This second semicircle is indicative of samples for which there is charge adsorption onto the electrode surface.[23] The spectra on fluoropolymer electrodes are then modeled without including charge adsorption phenomenon, and values for the conductivity, charge carrier concentration, and charge carrier size are derived. These properties of the charge carriers on fluoropolymer electrodes are compared to results obtained from bare indium tin oxide electrodes. The charge carrier properties of Span-20, Span-80, and Span-85 are then compared to discern the effects of surfactant chemistry on charge stabilization.

2.2 Theory

Yezer et al.[22,23] have extensively developed the interpretation of EIS spectra of surfactant doped nonpolar liquids. With bare ITO electrodes, the impedance spectra was fit with an equivalent circuit where complex phase elements (CPEs) describe the double layer and charge desorption kinetics. Theoretically, in the absence of charge adsorption, the best fit equivalent circuit is the 4-element circuit shown in **Figure 2.1**.[22]

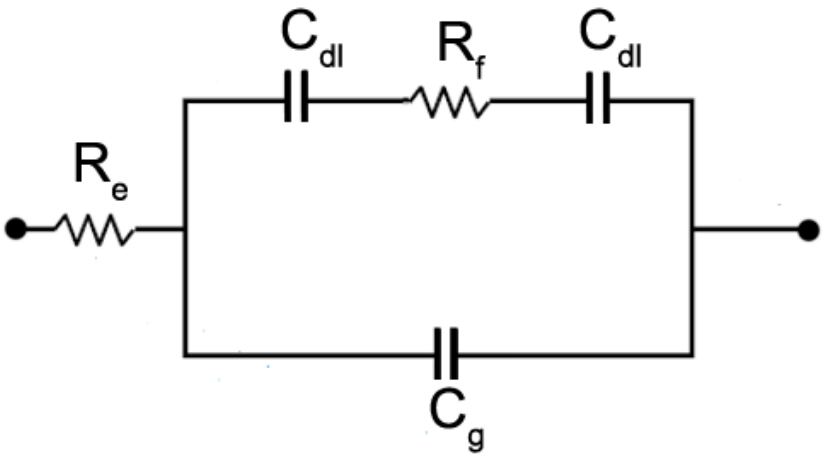

Figure 2.1. 4 element equivalent circuit without charge adsorption. [22]

The electrical properties of the sample can be derived from the impedance elements R_e (resistance of the wires), R_f (resistance of the fluid), C_g (geometric capacitance), and C_{dl} (double layer capacitance) according to the following equations.[22]

$$R_f = \frac{d}{A_f K} \tag{2.1}$$

$$C_g = \frac{\varepsilon_f A_f}{d} \tag{2.2}$$

$$C_{dl} = \frac{\varepsilon_f}{\lambda_D} \cosh\left(\frac{e\xi}{2k_B T}\right) \tag{2.3}$$

where d is the gap distance between the electrodes, A_f is the area of the solution held between the two electrodes, K is the conductivity of the solution, and ζ is the zeta potential of the electrode surface. The equation for C_{dl} assumes that all charge carriers are 1-1 electrolytes and is derived from the Guoy-Chapman model for a diffuse layer of charge accumulated at each electrode. The ionic strength of the bulk fluid can then be calculated from equations (2.3) and (2.4). In this circuit, the double layer at each

electrode plate is modeled as a capacitor with a differential capacitance that scales with the Debye length (λ_D),

$$\lambda_D = \sqrt{\frac{\varepsilon_f k_B T}{2e^2 n_0}} \tag{2.4}$$

Where ε_f is the permittivity of the solution, k_B is Boltzmann's constant, T is absolute temperature, e is the charge on one proton, and n_0 is the ionic strength (number per volume). Ultimately, the conductivity and ionic strength of the sample is used to determine the diffusion coefficient (D) and hydrodynamic radius of charge carriers.

$$D = \frac{k_B T K}{2 n_o e^2} \tag{2.5}$$

The overall impedance of this 4-element circuit is as given by Yezer *et al.* as[22]

$$Z = R_e + \left[\left(R_f + \frac{2i}{\omega C_{dl}}\right)^{-1} + \left(\frac{i}{\omega C_g}\right)^{-1}\right]^{-1} \tag{2.6}$$

where the real and imaginary parts of the impedance are given as

$$Re(Z) = R_e + \frac{R_f}{1 + 4c + 4c^2 + \Omega^2} R_f \tag{2.7}$$

and

$$Im(Z) = \frac{(2c + 4c^2)\Omega^{-1} + \Omega}{1 + 4c + 4c^2 + \Omega^2} R_f \tag{2.8}$$

where

$$c = \frac{C_g}{C_{dl}} \tag{2.9}$$

and

$$\Omega = \omega R_f C_g \tag{2.10}$$

In our experiments, the Debye length (λ_D) is assumed to be small relative to the gap distance (L) between electrodes such that

$$c = \frac{C_g}{C_{dl}} = \frac{\lambda_D}{L} \ll 1 \tag{2.11}$$

As Yezer *et al.*[22] have shown, the asymptotic form of equation (2.8) in the limit of large frequencies is

$$\lim_{\omega \to \infty} Im(Z) = \frac{1}{C_g}\omega^{-1} + O(\omega^{-3}) \tag{2.12}$$

Similarly, the asymptotic form of equation (2.7) in the limit of small frequencies and values of c is[22]

$$\lim_{\omega \to 0} \mathrm{Re(Z)} = R_f + O(\omega^2) \tag{2.13}$$

In the limit where c<<1, setting the derivative of equation (2.8) to zero results in expressions for the maximum and minimum of Im(Z) in terms of C_g, C_{dl}, and R_f.

$$\omega_{max} = \frac{1}{R_f C_g} \tag{2.14}$$

and

$$\omega_{min} = \frac{1}{R_f \sqrt{C_g \frac{C_{dl}}{2}}} \tag{2.15}$$

where the factor of 2 arises because there are two double-layer capacitors each

representing the double layer at one electrode in the equivalent circuit. Plotting *Im Z* versus ω (radians/second) in the high frequency range, C_g can be determined using a least squares regression with Origin (OriginLab Corp). Once C_g is inferred, equations (2.14) and (2.15) can be used to solve for R_f and C_{dl}.

While equations (2.14) and (2.15) accurately describe the values of C_g, C_{dl}, and R_f under conditions of suppressed charge adsorption, they fail to account for the current response arising from the fluoropolymer coating. Thus, the simple 4-element circuit introduced by Yezer *et al.* must be amended to account for the voltage drop across the fluoropolymer coating with the new impedance element C_{fp}. Thus, the equivalent circuit becomes the 5-Element shown in **Figure 2.2**.

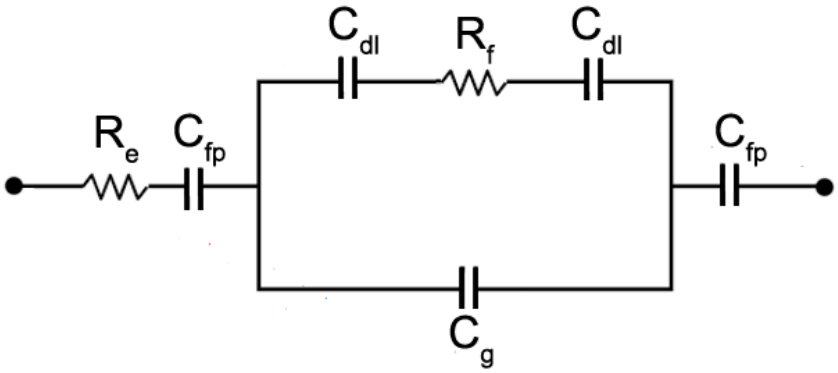

Figure 2.2. 5-Element equivalent circuit for EIS experiment on fluoropolymer electrodes.

The impedance expression that arises from the equivalent circuit shown in **Figure 2.2** is given as

$$Z(\omega) = R_e + \frac{2i}{\omega C_{fp}} + \left[\left(R_f + \frac{2i}{\omega C_{dl}}\right)^{-1} + \left(\frac{i}{\omega C_g}\right)^{-1}\right]^{-1} \tag{2.16}$$

Normalizing equation (2.16) by R_f and some algebraic manipulation results in the following expression *Im(Z)*

$$\frac{Im(Z)}{R_f} = \frac{[2b + 2(4b+1)c + 4(2b+1)c^2]\Omega^{-1} + (2b+1)\Omega}{1 + 4c + 4c^2 + \Omega^2} \tag{2.17}$$

where

$$b = \frac{C_g}{C_{fp}}, \quad c = \frac{C_g}{C_{dl}} \quad and \quad \Omega = \omega R_f C_g$$

The value of C_{fp} is defined as

$$C_{fp} = \frac{\varepsilon_{fp} A_f}{\lambda_{fp}}$$

where the value of ε_{fp} is determined from a dielectric constant of 2.3 as observed from capacitance measurements of a plasma polymerized layer of C_4F_8.[38] The value of the thickness of the fluoropolymer coating (λ_{fp}) is 33 nm as measured from white light interferometry (Zygo).

To derive an expression for the ratio between $Im(Z)_{min}$ and $Im(Z)_{max}$ ($r_{Im(Z)}$) for the fluoropolymer electrode circuit, the roots of the derivative $dIm(Z)/d\Omega$ of equation (2.17) were obtained and then substituted into equation (2.16). Thus $r_{Im(Z)}$ is determined to be:

$$r_{Im(Z)} = \frac{Im(Z_{min})}{Im(Z_{max})} = \frac{(1-s)(3+s)\sqrt{1+s-4[(2c+1)b+c]}}{(1+s)(3-s)\sqrt{1-s-4[(2c+1)b+c]}} \tag{2.18}$$

where s is defined as:

$$s = \sqrt{1 - 16[(2c+1)b + c]} \tag{2.19}$$

Plotting $Im\ Z$ versus ω (radians/second) of fluoropolymer electrodes in the high frequency range, an electrode capacitance, C_E, can be fit using a least squares regression with Origin (OrginLab Corp) in a manner similar to equation (2.12)**.** This C_E is related to C_g and C_{fp} according to the equation below.

$$\frac{1}{C_E} = \frac{1}{C_g} + \frac{1}{C_{fp}} \tag{2.20}$$

Once C_g is inferred, C_{dl} is determined from equation (2.18) through deriving a suitable value for c from the experimental value of $r_{Im(Z)}$. Finally, R_f can be calculated iteratively from equation (2.17) by fitting it to the local maximum of the *Im(Z)* spectra and known values of *b*, *c*, and C_g.

2.3 Materials and Methods

The surfactants investigated in this work were Span-20 (sorbitan monolaurate), Span-80 (sorbitan monooleate), and Span-85 (sorbitan trioleate) (Sigma-Aldrich). These nonionic surfactants consist of a polar sorbitan head group attached to a nonpolar carbon tail. Span-20 has the lowest molecular weight (MW 346.46 g/mol) with a 12-carbon tail while Span-85 is the highest molecular weight surfactant (MW 957.52 g/mol) with three 16 carbon tails attached to the head group. Span-80 has a molecular weight of 428.62 g/mol with a single 16 carbon tail. These surfactants were dissolved in anhydrous dodecane (Sigma-Aldrich). All solvent used was dehydrated to below 10 ppm of water content with molecular sieves. The surfactants were also dehydrated in a rotary evaporator for 1 hour at 60 degrees Celsius. All solutions were sparged with nitrogen until the water content dropped below the 10 ppm detection limit of the Karl Fischer water titrator prior to use. Nitrogen sparge time varied between 30 minutes to 3 hours depending on surfactant.

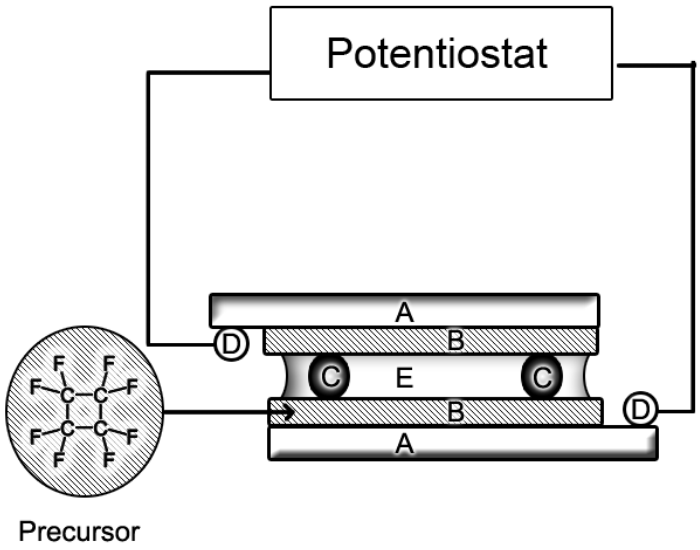

Figure 2.3. Schematic of the impedance cell. Indium tin oxide (ITO) coated glass electrodes (A) are coated with a 100 nm layer of fluoropolymer (B). The fluid (E) is held apart by 8 micron spacer beads (C). Cell is attached to the potentiostat with wire leads (D).

A schematic of the impedance cell is given in **Figure 2.3**. The impedance cell consists of two glass slides coated with 100nm thickness indium tin oxide (ITO) (Sigma-Aldrich) with wire leads attached to one end of each electrode with silver epoxy (MG Chemicals). A 33 nm fluoropolymer coating was fabricated using a STS Multiplex DRIE ICP system to deposit gaseous C_4F_8 particles onto the ITO surface (CMU Nanofabrication Lab). The fluoropolymer coating thickness was determined using a Zygo white light interferometer by measuring the surface topography of the ITO to fluoropolymer deposition boundary. This fluoropolymer thickness was chosen because it was the upper limit of the STS Multiplex DRIE ICP; although theoretically, there will be a trade-off between adsorption suppression and dielectric loss with layer thickness. In assembly of the impedance cell, a uniform gap distance between the two electrodes was maintained by adding 8 micron diameter silica particles spacers (Cospheric LLC) at a concentration of 1 mg / 5 mL surfactant solution. In total, 15 µL of spacer and

surfactant solution was injected with a gas tight syringe (Hamilton Co) to form a thin film between the two electrodes. To determine the dimensions of the cell geometry, a cell constant was defined for each assembled cell as the ratio of the surface area of the fluid to the gap distance between the electrodes. The cell constant was then calculated by calibrating the dielectric constant calculated from the impedance spectra to that of the literature value for dodecane.[39] All impedance cell assembly took place in a nitrogen inflated glove bag (Sigma-Aldrich). To conduct the impedance experiments, the wire leads of the assembled impedance cell were connected to a VersaSTAT 3 potentiostat (Princeton Applied Research) equipped with a Low Current Interface (LCI) as described in the previous work.[22] Impedance experiments were assumed to be conducted in the linear regime of the current response as shown in the previous work. [22] All impedance experiments occurred in a nitrogen-blanketed Faraday cage to limit exposure to water in ambient air. After each impedance experiment, the electrodes were rinsed with dehydrated dodecane and dried with nitrogen gas.

To determine any instrumental effects of the potentiostat on the impedance spectrum as well as the rigor of equations (2.14) and (2.15), a soldered circuit matching the simple 4-element equivalent circuit in **Figure 2.1** was assembled and tested. The soldered circuit was assembled from a series RC circuit (R_f = 100 kΩ , 0.5xC_{dl} = 470 nF) that is in parallel with a capacitor (C_g = 10 nF). In the soldered circuit, as a single capacitor having a capacitance of C_{dl}/2 was substituted in place of two double layer capacitors.

The zeta potential of the fluoropolymer coated ITO surface was necessary to calculate the ionic strength of charge carriers from the impedance spectra. Zeta

potentials of 33 nm thick fluoropolymer coated ITO glass slides were obtained from the ZetaSpin^{TM}. The ZetaSpin apparatus is as presented by Yezer.[42] The fluoropolymer slide was glued to the circular end of the ZetaSpin^{TM} spindle mount with sugar syrup. A motor spun the surface sample at 2000 rpm for the duration of 500 to 2000 seconds depending on the conductivity of the surfactant solution. The streaming potential between two points in the ZetaSpin^{TM} cell was measured with chemically inert, glassy carbon electrodes. The software (LabVIEW, National Instruments) calculated the zeta potential of the fluoropolymer surface from the streaming potential according to theory presented by Yezer.[42] All surfactant solutions were continuously sparged with nitrogen in the ZetaSpin^{TM} cell, and the water content closely monitored with a coulometric Karl-Fisher water titrator. The water content of solutions was maintained below 10 ppm at all times.

2.4 Results and Discussion

In this paper, we develop a coating that suppresses charge adsorption in impedance spectroscopy of Span doped dodecane. In cases of severe charge adsorption, impedance spectroscopy cannot be used to infer the ionic strength of certain surfactant-solvent systems. This coating greatly increases the breadth of sample systems suitable for study using impedance spectroscopy.

To investigate the effect of instrumental relics on the impedance spectra and validate the equivalent circuit presented in **Figure 2.1**, an EIS experiment was performed on a soldered circuit. The *Re(Z)* and *Im(Z)* for this soldered circuit are plotted in **Figure 2.4**.

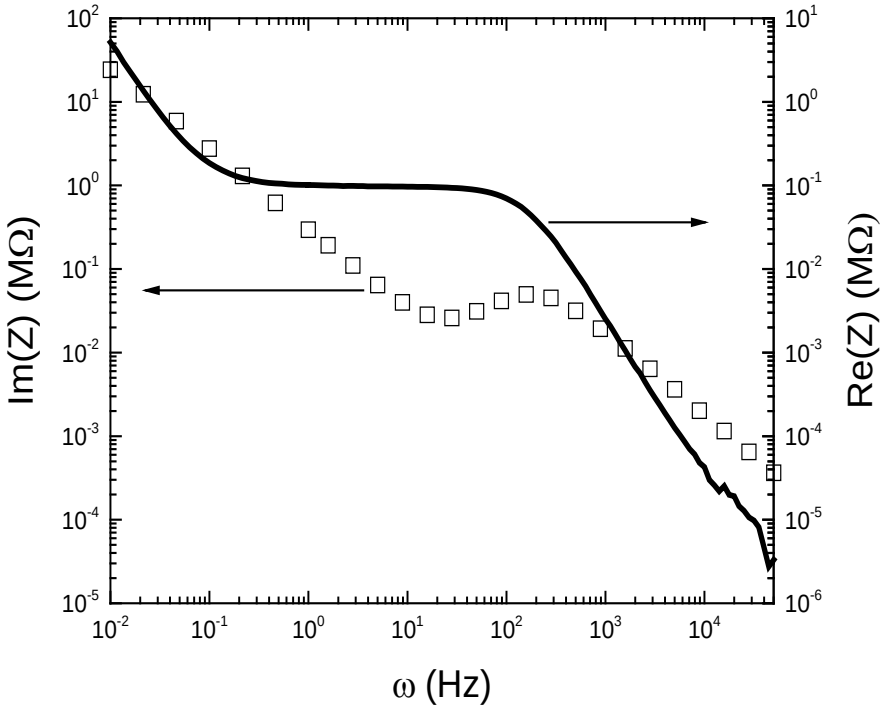

Figure 2.4. Bode plot of the imaginary and real impedance of a soldered circuit consisting of C_g = 10 nF, 0.5C_{dl} = 470 nF, and R_f = 100 kΩ. There is one maxima and one minima as predicted by equations (2.14) and (2.15).The upward drift in *Re(Z)* at low frequency is likely an instrumental effect rather than a physical consequence of the soldered circuit.

The imaginary impedance spectrum in **Figure 2.4** was analyzed using equations (2.14) and (2.15), and the derived values of C_g, C_{dl}, and R_f were within 5% of the nominal values. Although equations equations (2.14) and (2.15) were able to predict the maximum and minimum of Im(Z), the spectra showed significant deviations from theory at low frequencies. Equation (2.13) predicts that the asymptotic value of *Re(Z)* at low frequencies is equal to R_f; however, the real impedance spectrum in **Figure 2.4** is drifting upward at low frequencies. This mathematically inconsistent behavior as ω approaches zero is thought to be an instrumental relic rather than a physical consequence of the soldered circuit. As a result, the analysis method presented in the

theory section focuses on features of the impedance spectra that occur at frequencies above 1 Hz.

To determine the effectiveness of the fluoropolymer coating in passivating charge adsorption effects, we examine the Nyquist and Bode plots of the impedance spectra. The Nyquist plot for 10 mM Span-80 in dodecane on bare ITO and fluoropolymer (FP) coated electrodes is shown in **Figure 2.5**. From the Bode plots in **Figure 2.5**, the number of semicircles on ITO compared to FP electrodes indicates the absence of charge adsorption on FP electrodes. On ITO electrodes, the impedance spectrum consists of two semi-circles that transition into a linear “tail” of positive slope. This tail-like curve will be referred to as the capacitive tail as the imaginary impedance dominates the real impedance at low frequencies. The first semicircle results from a RC circuit composed C_g and R_f in parallel, while the second semicircle and capacitive tail contains information regarding C_{dl} and the charge adsorption kinetics.[22] Once the charge adsorption is suppressed by the fluoropolymer coating, the second semicircle in the Nyquist plot vanishes, and C_{dl} can be inferred from the impedance ratio between the transition of the semicircle to the capacitive tail and the radius of the first semicircle according to equation (2.18).

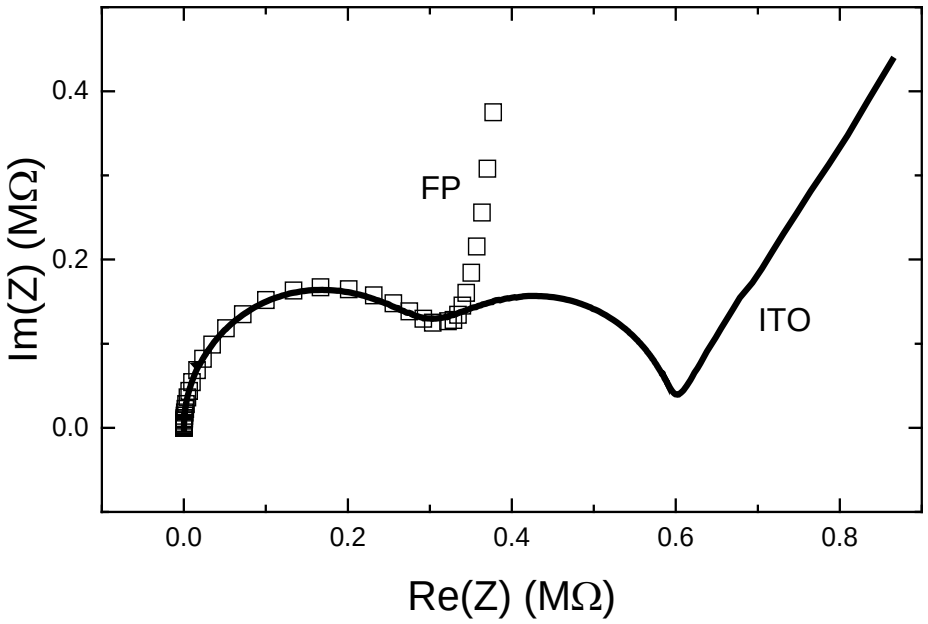

Figure 2.5. Nyquist plot comparing the impedance spectra of 10 mM Span-80 in dodecane on bare indium tin oxide (ITO) coated electrodes (black line) and fluoropolymer (FP) coated electrodes (open squares). The second semi-circle in the impedance spectra on bare ITO electrodes indicates presence of reversible charge adsorption at low frequencies.

The real and imaginary parts of the impedance spectra for 10 mM Span-80 in dodecane are shown in Bode plots **Figure 2.6** and **Figure 2.7** respectively. Because the fluoropolymer (FP) electrodes suppress charge adsorption, Im(Z) has only one minimum and one maximum, the ratio between which is as described (2.18). In contrast, the Im(Z) on ITO electrodes have two maxima and two minima as predicted by Yezer et al. indicating the presence of charge adsorption.[23] This undesirable charge adsorption at the electrode surface also manifests in the low frequency behavior of Re(Z). As $\omega \rightarrow 0$ in **Figure 2.7**, the presence of charge adsorption on ITO electrodes increases *Re(Z)* relative to that of FP electrodes. Another feature of interest in **Figure *2.7*** is that neither the *Re(Z)* of ITO or FP reach a low frequency asymptote. This demonstrates the presence of a low frequency instrumental artifact also evident in the soldered circuit.

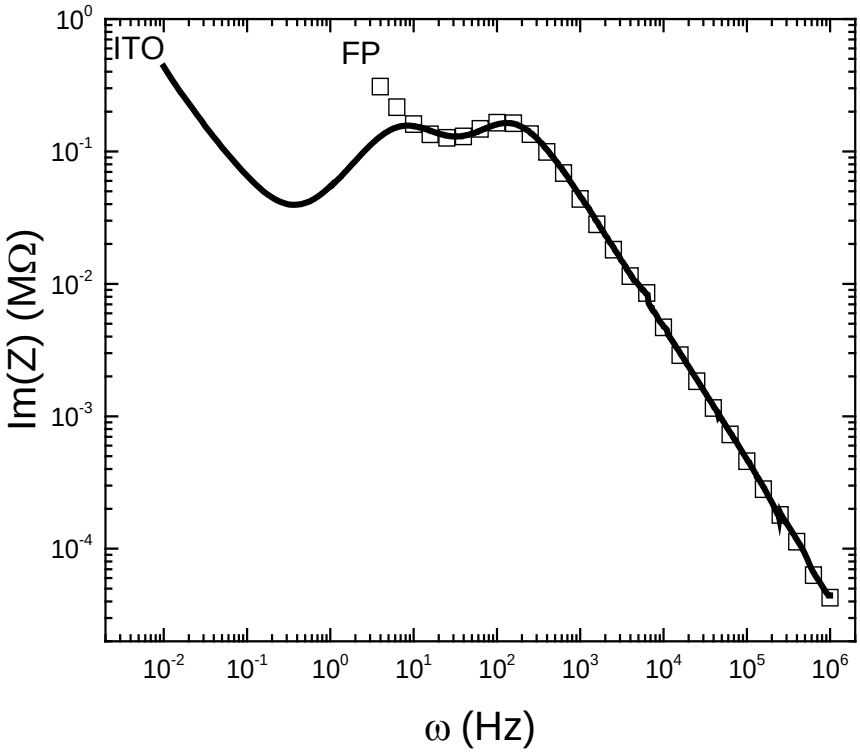

Figure 2.6. Bode plot comparing the imaginary impedance spectra of 10 mM Span-80 in dodecane on bare ITO electrodes (black line) and fluoropolymer (FP) coated electrodes (open squares). The impedance extrema unique to the ITO electrodes result from charge adsorption at low frequencies.

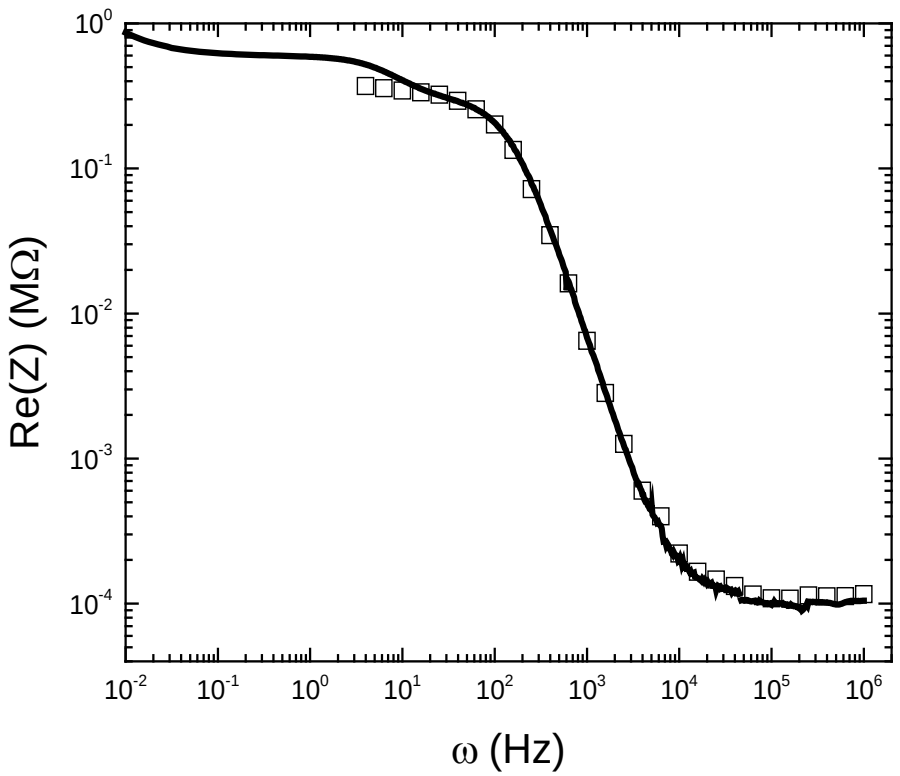

Figure 2.7. Bode plot comparing the real impedance spectra of 10 mM Span-80 in dodecane on bare ITO electrodes (black line) and fluoropolymer coated electrodes (open squares). The deviations between the two spectra arise from the presence of charge adsorption on the ITO electrodes at low frequencies.

Under conditions of severe charge adsorption, the Nyquist plot shows only one distorted semicircle with a capacitive tail because the charge adsorption kinetics obscure the double layer capacitance.[22] Such a scenario is shown experimentally for 100 mM Span-85 in dodecane on ITO electrodes in **Figure 2.8**. Although the impedance spectra on ITO and FP electrodes appear qualitatively similar with one semicircle, we will show that the difference in the Im(Z) behavior reveals the presence of charge adsorption on ITO electrodes. The experimental values of conductivity, Debye length, charge carrier concentration, and charge carrier diameter for ITO versus FP electrodes are tabulated in **Table 2.1**.

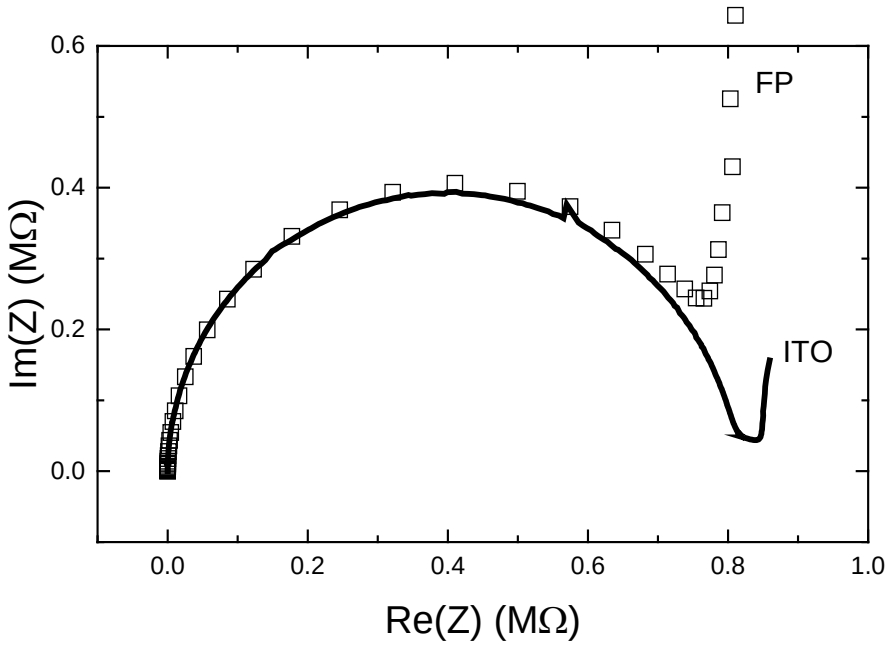

Figure 2.8. Nyquist plot comparing the impedance spectra of 100 mM Span-85 in dodecane on bare indium tin oxide (ITO) coated electrodes (black line) and fluoropolymer (FP) coated electrodes (open squares). Under these conditions, charge adsorption completely obscures the double layer capacitance, and the Nyquist plot for both electrodes shows only one semi-circle.

Table 2.1. Comparison between bare ITO electrodes and fluoropolymer coated electrodes experimental results on 10 mM Span-80 in dodecane and 100 mM Span-85 in dodecane. The span-80 spectra on ITO is fit using the equivalent circuit described in previous work while the span-85 spectra on ITO is fit assuming no charge adsorption. All error values were obtained from the standard deviation of three separately constructed impedance cells.

Concn (mM)	surfactant	Coating	conductivity (nS/m)	debye length (nm)	charge concn ($1/\mu m^3$)	d_h (nm)
10	span-80	fluoropolymer	15.4 ± 0.09	140 ± 2	73 ± 2	19 ± 1
10	span-80	ITO	15.3 ± 0.06	182 ± 8	43 ± 3	11 ± 2
100	span-85	fluoropolymer	6.0 ± 0.1	67.5 ± 0.6	311 ± 6	210 ± 10
100	span-85	ITO	5.0 ± 0.5	0.4 ± 0.1	$1.3 \pm 0.7 \times 10^7$	$10 \pm 5 \times 10^6$

In **Table 2.1**, 10 mM Span-80 in dodecane on ITO represents a case of mild charge adsorption such that both the adsorption kinetics and the double layer capacitance were calculated using the method described by Yezer.[23] In contrast, a successful passivating coating for this sample should possess an impedance spectrum that is well described by the 5-element equivalent circuit and mathematical relationships given in equations (2.16) through (2.20). Essentially, all charge transport processes on the passivating coating should be accounted for using the impedance elements C_g, R_f, C_{fp} and C_{dl}. Qualitatively, we observe the disappearance of the second semicircle in the Nyquist plot of 10 mM Span-80 indicating agreement with the 5-element equivalent circuit and the suppression of charge adsorption. Quantitatively, we examine the derived conductivity, charge concentration, and hydrodynamic diameter of Span-80 on FP electrodes and conclude they are reasonable for charged micelles. The derived conductivity for Span-80 is the same on ITO and FP electrodes while the number of charge carriers is slightly larger on FP electrodes. This indicates that while charge adsorption tends to decrease the number of charge carriers in the bulk, neutral micelles in the bulk can become charged to replace the charges lost due to adsorption. Thus, 10 mM Span-80 represents a case of mild charge adsorption because the adsorption kinetics do not obscure measurement of the double layer capacitance. In **Table 2.1**, 100 mM Span-85 in dodecane on ITO represents a case of severe charge adsorption such that the impedance spectra cannot be modeled using the method proposed by Yezer.[23] Examining the morphology of the impedance spectra in **Figure 2.8**, one might be tempted to conclude that there is no charge adsorption and use equations (2.8) and (2.9) to model the impedance spectra. Such derived results are shown in **Table 2.1** for 100

mM Span-85 in dodecane on ITO electrodes. Clearly, this method is incorrect as the calculated size of the charge carriers is larger than the physical gap distance between the two electrodes. In contrast, the impedance spectra of 100 mM Span-85 in dodecane on FP electrodes is be well modeled using equations (2.16) through (2.20) and the 5-element circuit model. The resulting values for the Debye length, charge carrier concentration, and hydrodynamic diameter are physically feasible and typical of charged micelles.[22,23]

The charging behavior of Span-20, Span-80, and Span-85 can be elucidated by the impedance spectra in **Figure 2.9** and **Figure 2.10**. Im(Z) for all surfactants tested have one minimum and one maximum as predicted by equations 16 through 20, indicating suppression of charge adsorption. The charging properties of each surfactant are tabulated in **Table 2.2.** For the purposes of comparison concentrations of surfactant were chosen so that all measured conductivities were roughly the same magnitude.

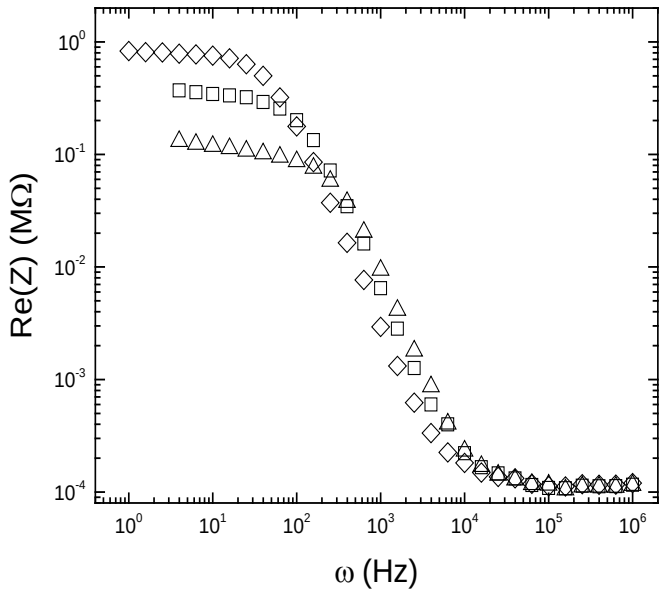

Figure 2.9. Bode plot of the real impedance spectra of 100 mM Span-85 (open diamonds), 10 mM Span-80 (open squares), and 10 mM Span-20 (open triangles) on fluoropolymer coated electrodes.

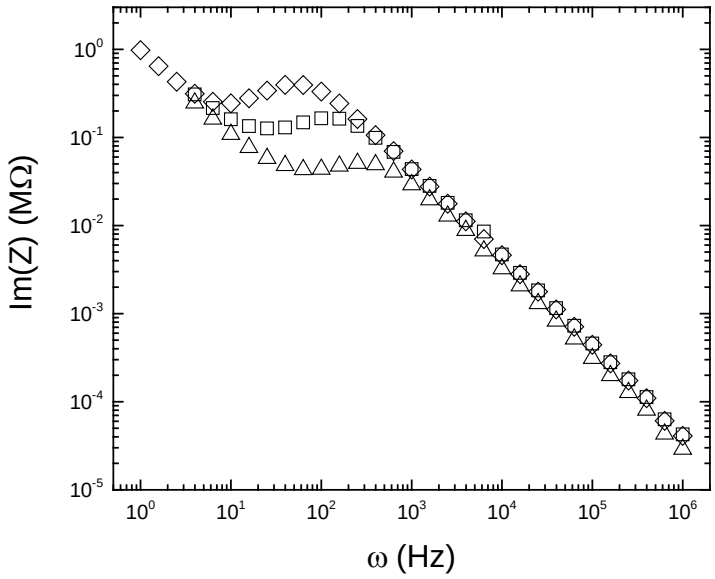

Figure 2.10. Bode plot of the imaginary impedance spectra of 100 mM Span-85 (open diamonds), 10 mM Span-80 (open squares), and 10 mM Span-20 (open triangles) in dodecane using fluoropolymer coated electrodes. Each spectra has two extrema indicating the suppression of charge adsorption by the fluoropolymer coating for Span-20, Span-80, and Span-85.

Table 2.2. Summary of experimental results of Span-20, 80, and 85 in dodecane on fluoropolymer coated electrodes. All error values were obtained from three separately constructed impedance cells.

surfactant	concn (mM)	conductivity (nS/m)	debye length (nm)	no. charge carriers ($1/\mu m^3$)	d_h (nm)	ζ (mV)
span-85	100	6.0 ± 0.1	67.5 ± 0.6	311 ± 6	210 ± 10	-11.3 ± 0.5
span-80	10	15.4 ± 0.09	140 ± 2	73 ± 2	19 ± 1	-16.7 ± 0.8
span-20	10	35 ± 6	130 ± 20	80 ± 20	10 ± 1	-5.8 ± 0.7

Span-20 100 surfactants formed the smallest micelles at 10 ± 1 nm while Span-85 1 formed the largest micelles at 210 ± 10 nm. Broadly speaking, the micelle size tended to increase as the HLB number decreased as corroborated by similar x-ray and light scattering studies in the literature.[40,41] One interpretation of this behavior is that hydrophobic surfactants pack closer together forming larger micelles with a smaller

degree of curvature. Isolating surfactant tail effects, Parent *et al*. found that di-tailed PIBS surfactant formed smaller micelles than single tailed PIBS surfactants.[40] This trend is attributed to the steric hindrance of the surfactant tail causing more curvature in the reverse micelle and hence decreasing the overall micelle size. In contrast, EIS experiments indicate Span-85, which has three 16 carbon tails, formed much larger micelles than Span-80, which has one 16 carbon tail. This discrepancy may be attributed to some solvent specific interaction between Span-85 and dodecane as well as the extreme steric challenges posed by a three tailed surfactant compared to a di-tailed surfactant in a low water environment. Overall, surfactant chemistry and structure have significant effects on micelle assembly and hence charge stabilization in nonpolar liquids.

2.5 Conclusions

Previous efforts to characterize charge carriers using impedance spectroscopy has been hindered by charge adsorption onto the electrode surface. The pinning of dissociable species due to this electrode specific surface effect is ultimately undesirable and may impact the concentration of charge carriers in the bulk. By coating the electrodes with plasma polymerized fluoropolymer, the charge adsorption effect is suppressed, and the impedance spectra can be fit by a simpler equivalent circuit.

We qualitatively verify the suppression of charge adsorption by the fluoropolymer coating through observation of the disappearance of the second semi-circle in the Nyquist plots of the impedance. Quantitatively, we find that the impedance spectra on fluoropolymer coated electrodes are well modeled by an equivalent circuit that ignores charge adsorption. Ionic strength and charge carrier size calculated from the impedance

spectra are characteristic of inverse micelles and confirm that they are source of charge in surfactant doped nonpolar liquids. Finally, we compare trends in charge carrier size across surfactants and find good agreement with literature results indicating that charge carrier size increases with decrease in surfactant HLB number. This is thought to arise from the surfactant hydrophobicity decreasing the degree of curvature in micelle formation.

2.6 Acknowledgements

We thank Norman Gottron and Mason Risley at the Carnegie Mellon Nanofabrication Facility for the plasma deposition expertise and manufacturing of the C_4F_8 coating. Thanks to Bugra Ozutemiz and Dr. Burak Ozdoganlar at the mechanical engineering department at Carnegie Mellon for access and training on the white light interferometer. We also gratefully acknowledge financial support through NSF grant #1511619.

2.7 References

(1) Chen, Y.; Au, J.; Kazlas, P.; Ritenour, a; Gates, H.; McCreary, M. Electronic Paper: Flexible Active-Matrix Electronic Ink Display. *Nature* **2003**, *423* (6936), 136.

(2) Comiskey, B.; Albert, J. D.; Yoshizawa, H.; Jacobson, J. An Electrophoretic Ink for All-Printed Reflective Electronic Displays. *Nature* **1998**, *394* (6690), 253–255.

(3) Nikakhtari, H.; Vagi, L; Choi, P.; Liu, Q.; Gray, M. R.; Univ, A. Solent Screening For Non-Aqueous Extraction of Alberta Oil Sands. *Can. J. Chem. Eng.* **2013**, *91* (6), 1153–1160.

(4) Jones, S. A.; Martin, G. P.; Brown, M. B. Manipulation of Beclomethasone-Hydrofluoroalkane Interactions Using Biocompatible Macromolecules. *J. Pharm. Sci.* **2006**, *95* (5), 1060–1074.

(5) Eicke, H. F.; Borkovec, M.; Das-Gupta, B. Conductivity of Water-in-Oil Microemulsions: A Quantitative Charge Fluctuation Model. *J. Phys. Chem.* **1989**, *93* (1), 314–317.

(6) Espinosa, C. E.; Guo, Q.; Singh, V.; Behrens, S. H. Particle Charging and Charge Screening in Nonpolar Dispersions with Nonionic Surfactants. *Langmuir* **2010**.

(7) Liu, H.; Wang, S.; Xiao, Y.; Yang, Q.; Li, X. Charging Behavior of Carbon Black in a Low-Permittivity Medium Based on Acid-Base Charging Theory. *J. Mater. Chem. C* **2015**, *3* (16).

(8) Gacek, M. M.; Berg, J. C. The Role of Acid-Base Effects on Particle Charging in Apolar Media. *Adv. Colloid Interface Sci.* **2015**, *220*, 108–123.

(9) Poovarodom, S.; Berg, J. C. Effect of Particle and Surfactant Acid-Base Properties on Charging of Colloids in Apolar Media. *J. Colloid Interface Sci.* **2010**, *346* (2), 370–377.

(10) Kemp, R.; Sanchez, R.; Mutch, K. J.; Bartlett, P. Nanoparticle Charge Control in Nonpolar Liquids: Insights from Small-Angle Neutron Scattering and Microelectrophoresis. *Langmuir* **2010**.

(11) Klinkenberg, A.; Leonard van der Minne, J. *Electrostatics in the Petroleum Industry: The Prevention of Explosion Hazards*; Elsevier, 1958.

(12) Gacek, M. M.; Berg, J. C. Effect of Surfactant Hydrophile-Lipophile Balance (HLB) Value on Mineral Oxide Charging in Apolar Media. *J. Colloid Interface Sci.* **2015**, *449*, 192–197.

(13) Morrison, I. D. Electrical Charges in Nonaqueous Media. *Colloids Surfaces A Physicochem. Eng. Asp.* **1993**, *71* (1), 1–37.

(14) Bombard, A. J. F.; Dukhin, A. Ionization of a Nonpolar Liquid with an Alcohol. *Langmuir* **2014**, *30* (15), 4517–4521.

(15) Pontiga, F.; Castellanos, A. Electrical Conduction of Electrolyte Solutions in Nonpolar Liquids. *IEEE Trans. Ind. Appl.* **1996**, *32* (4), 816–824.

(16) Schmidt, J.; Prignitz, R.; Peschka, D.; M??nch, A.; Wagner, B.; Bonsch, E.; Peukert, W. Conductivity in Nonpolar Media: Experimental and Numerical Studies on Sodium AOT-Hexadecane, Lecithin-Hexadecane and Aluminum(III)-3,5-Diisopropyl Salicylate-Hexadecane Systems. *J. Colloid Interface Sci.* **2012**, *386* (1), 240–251.

(17) Prieve, D. C.; Hoggard, J. D.; Fu, R.; Sides, P. J.; Bethea, R. Two Independent Measurements of Debye Lengths in Doped Nonpolar Liquids. *Langmuir* **2008**, *24* (4), 1120–1132.

(18) Kumar, B.; Crittenden, S. R. Stern Potential and Debye Length Measurements in Dilute Ionic Solutions with Electrostatic Force Microscopy. *Nanotechnology* **2013**,

24 (43), 435701.

(19) Beunis, F.; Strubbe, F.; Karvar, M.; Drobchak, O.; Brans, T.; Neyts, K. Inverse Micelles as Charge Carriers in Nonpolar Liquids: Characterization with Current Measurements. *Current Opinion in Colloid and Interface Science*. 2013, pp 129–136.

(20) Kim, J.; Anderson, J. L.; Garoff, S.; Schlangen, L. J. M. Ionic Conduction and Electrode Polarization in a Doped Nonpolar Liquid. *Langmuir* **2005**, *21* (19), 8620–8629.

(21) Kornilovitch, P.; Jeon, Y. Transient Electrophoretic Current in a Nonpolar Solvent. *J. Appl. Phys.* **2011**, *109* (6).

(22) Yezer, B. A.; Khair, A. S.; Sides, P. J.; Prieve, D. C. Use of Electrochemical Impedance Spectroscopy to Determine Double-Layer Capacitance in Doped Nonpolar Liquids. *J. Colloid Interface Sci.* **2015**, *449*, 2–12.

(23) Yezer, B. A.; Khair, A. S.; Sides, P. J.; Prieve, D. C. Determination of Charge Carrier Concentration in Doped Nonpolar Liquids by Impedance Spectroscopy in the Presence of Charge Adsorption. *J. Colloid Interface Sci.* **2016**, *469*, 325–337.

(24) Karvar, M.; Strubbe, F.; Beunis, F.; Kemp, R.; Smith, N.; Goulding, M.; Neyts, K. Investigation of Various Types of Inverse Micelles in Nonpolar Liquids Using Transient Current Measurements. *Langmuir* **2014**, *30* (41), 12138–12143.

(25) Beunis, F.; Strubbe, F.; Karvar, M.; Drobchak, O.; Brans, T.; Neyts, K.; Verschueren, A. R. M. Electric Charging of Inverse Micelles in a Nonpolar Liquid with Surfactant. *Colloids Surfaces A Physicochem. Eng. Asp.* **2014**, *440*, 10–19.

(26) Strubbe, F.; Verschueren, A. R. M.; Schlangen, L. J. M.; Beunis, F.; Neyts, K. Generation Current of Charged Micelles in Nonaqueous Liquids: Measurements and Simulations. *J. Colloid Interface Sci.* **2006**, *300* (1), 396–403.

(27) Karvar, M.; Strubbe, F.; Beunis, F.; Kemp, R.; Smith, N.; Goulding, M.; Neyts, K. Charging Dynamics of Aerosol OT Inverse Micelles. *Langmuir* **2015**, *31* (40), 10939–10945.

(28) Wu, Y. F.; Ru, Y. L. Electrochemical Polishing of ITO Films. *Microelectron. Eng.* **2010**, *87* (12), 2549–2554.

(29) Voigt, M.; Sokolowski, M. Electrical Properties of Thin Rf Sputtered Aluminum Oxide Films. *Mater. Sci. Eng. B* **2004**, *109* (1), 99–103.

(30) Liu, P.; Singh, V. P.; Rajaputra, S. Barrier Layer Non-Uniformity Effects in Anodized Aluminum Oxide Nanopores on ITO Substrates. *Nanotechnology* **2010**,

21 (11), 115303.

(31) Foong, T. R. B.; Sellinger, A.; Hu, X. Origin of the Bottlenecks in Preparing Anodized Aluminum Oxide (AAO) Templates on ITO Glass. *ACS Nano* **2008**, *2* (11), 2250–2256.

(32) Kang, B.; Tan, L. W.; Silva, S. R. P. Ultraviolet-Illuminated Fluoropolymer Indium-Tin-Oxide Buffer Layers for Improved Power Conversion in Organic Photovoltaics. *Org. Electron. physics, Mater. Appl.* **2009**, *10* (6), 1178–1181.

(33) Gao, J. X.; Yeo, L. P.; Chan-Park, M. B.; Miao, J. M.; Yan, Y. H.; Sun, J. B.; Lam, Y. C.; Yue, C. Y. Antistick Postpassivation of High-Aspect Ratio Silicon Molds Fabricated by Deep-Reactive Ion Etching. *J. Microelectromechanical Syst.* **2006**, *15* (1), 84–93.

(34) Andersson, H.; Van der Wijngaart, W.; Griss, P.; Niklaus, F.; Stemme, G. Hydrophobic Valves of Plasma Deposited Octafluorocyclobutane in DRIE Channels. *Sensors Actuators, B Chem.* **2001**, *75* (1–2), 136–141.

(35) Vogelsang, A.; Ohl, A.; Foest, R.; Weltmann, K. D. Fluorocarbon Plasma Polymer Deposition by an Atmospheric Pressure Microplasma Jet Using Different Precursor Molecules - A Comparative Study. *Plasma Process. Polym.* **2013**, *10* (4), 364–371.

(36) Allgood, C. C. Fluorinated Gases for Semiconductor Manufacture: Process Advances in Chemical Vapor Deposition Chamber Cleaning. *J. Fluor. Chem.* **2003**, *122* (1), 105–112.

(37) Yeo, L. P.; Yan, Y. H.; Lam, Y. C.; Chan-Park, M. B. Design of Experiment for Optimization of Plasma-Polymerized Octafluorocyclobutane Coating on Very High Aspect Ratio Silicon Molds. *Langmuir* **2006**, *22* (24), 10196–10203.

(38) Endo, K.; Tatsumi, T. Fluorinated Amorphous Carbon Thin Films Grown from C4F8 for Multilevel Interconnections of Integrated Circuits. *Nec Research & Development*. 1997, pp 287–293.

(39) Wohlfarth, C. W. Permittivity (Dielectric Constant) of Liquids Christian Wohlfarth. *CRC Handb. Chem. Phys.* **2016**, 6-187-6–208.

(40) Parent, M. E.; Yang, J.; Jeon, Y.; Toney, M. F.; Zhou, Z. L.; Henze, D. Influence of Surfactant Structure on Reverse Micelle Size and Charge for Nonpolar Electrophoretic Inks. *Langmuir* **2011**, *27* (19), 11845–11851.

(41) Shrestha, L. K.; Dulle, M.; Glatter, O.; Aramaki, K. Structure of Polyglycerol Oleic Acid Ester Nonionic Surfactant Reverse Micelles in Decane: Growth Control by Headgroup Size. *Langmuir* **2010**, *26* (10), 7015–7024.

(42) Yezer, B. A. Determination of Charge Concentration in Surfactant Doped Nonpolar Liquids, Carnegie Mellon University, 2016. Thesis.

Chapter 3 Enhanced charging of nonpolar media with various surfactant counterions

3.1 Introduction

Surface charging in nonpolar liquids ensures particle stability for many oil-based formulations. Introducing electrostatic repulsion between particles is vital to control of particle aggregation in tar sands,[1] stabilization of active pharmaceutical ingredients in drug delivery applications,[2] and prevention of soot build-up in engines.[3] This is accomplished through addition of dopant surfactants that form charged micelles in solution. While the mechanisms behind surface charging and charge formation in aqueous systems have been studied comprehensively, similar models for nonpolar liquids are primarily developed on a limited surfactant or surface specific basis. For example, acid-base interactions have been used to model surface charging on mineral oxides by the commercial surfactants AOT (diotcyl sodium sulfosuccinate),[4] Spans (sorbitan esters), and OLOA (poly-isobutylene succinimide)[5] while radial distribution functions have been used to model surface charging of PMMA particles by Spans[6] and AOT.[7]

For some ionic surfactants, formation of charge in nonpolar liquids can be modeled through ionic dissociation, just as in aqueous systems. Kemp found that at concentrations of sodium AOT below the critical micelle concentration, the fluid conductivity was as predicted by a simple ion dissociation model consisting of the surfactant and its sodium counterion.[8] In contrast to the dissociation model, the disproportionation model asserts that charging is a result of reverse micelles rather individual surfactants. In nonpolar liquids, surfactants assemble into reverse micelles

with water, ions, and polar head groups sequestered in an internal core and tails extended outwards to form a hydrocarbon shell. The disproportionation model predicts that Brownian collisions between two neutral micelles can result in an exchange of charge from one micelle to the other. Thus, two neutral micelles can leave a Brownian collision with equal and opposite charges if an ion is exchanged between the two. A key conclusion of the disproportionation model is that the fraction of charged micelles is consistent across surfactant concentrations if the micelle size remains constant. From the mass action laws of the disproportionation model, the surfactant concentration is proportional to fluid conductivity with a proportionality coefficient of one.[9] This relationship is observed in experimental literature data of AOT, Span, and OLOA surfactants.[8,10,11]

Eicke expands upon Brownian collisions being the impetus for micelle charging in an adapted “charge fluctuation” model for water-in-oil microemulsions.[12] During a micelle collision, Brownian forces would encourage the exchange of charge while the energy required to charge a neutral micelle would hinder the exchange of charge. Eicke approximates this activation energy to charging as the work required to add a point charge to a conductive metal sphere of radius *r* (Born energy of solvation).[12] More work is required to charge a small sphere compared to a large sphere because of the magnitude of the localized surface charge density. The charge fluctuation model is based solely on micelle size and predicts that the likelihood of a micelle acquiring charge increases with its size. Eicke et al. found good agreement between the predicted and experimental conductivity for AOT micelles of a certain size range.[12]

The majority of literature experiments focus on surface charging and charge

formation behavior of commercial surfactants in nonpolar liquids. While proprietary surfactants are readily available on the market and therefore of great industrial interest, they are often low in purity and offer little systematic differences in surfactant structures. As a result, it is difficult to attribute trends in charge formation to specific surfactant or micelle properties. For example, the conductivity of Span surfactants are conjectured to arise from dissociable impurities present in the proprietary formulation.[9] It is therefore difficult to discern whether the reverse micelles or the dissociable impurities are responsible any charging trends uncovered in the data.

In this paper, we introduce a flexible synthetic technique for production of high purity AOT analog surfactants. This synthesis technique allows for easy control of surfactant tail length, degree of branching, headgroup chemistry, and counterion composition. By synthesizing a catalogue of AOT analogs with incremental differences in surfactant chemistry, one can isolate specific structure-function relationships between surfactant and charging behavior. Two AOT analog surfactant are produced using the mentioned synthetic technique, and their charging properties are measured and compared to those of AOT. Surfactant solution conductivity and ionic strength are determined using electrochemical impedance spectroscopy in the method described in Chapter 2. Resulting comparisons between AOT and synthesized AOT analogs reveal order of magnitude difference in conductivity and ionic strength at similar surfactant concentrations. This paper reveals new relationships between surfactant and counterion chemistry and charging behavior not considered in the leading disproportionation or charge fluctuation theories for micelle charging.

3.2 Materials and Methods

3.2.1 Materials

Dioctyl sulfosuccinate sodium (Sigma-Aldritch) and two synthesized AOT analogs were the ionic surfactants studied in this work. Dioctyl sulfosuccinate sodium (MW: 445.6 g/mol) consists of a sodium counterion with a sulfosuccinate surfactant while the synthesized surfactants consist of a *para*-toluene sulfate (PTS) counterion with an aminosuccinate surfactant. Both surfactants have a two tailed branched structure and readily form reverse micelles in dodecane. The structures of the surfactants are shown in **Figure 3.1**. $(C_8b)_2$-Asp-PTS has the same number of carbons in its backbone structure as sodium dodecyl sulfate (AOT). $(C_8b)_2$-Glu-PTS has an additional methylene group compared to AOT and $(C_8b)_2$-Asp-PTS.

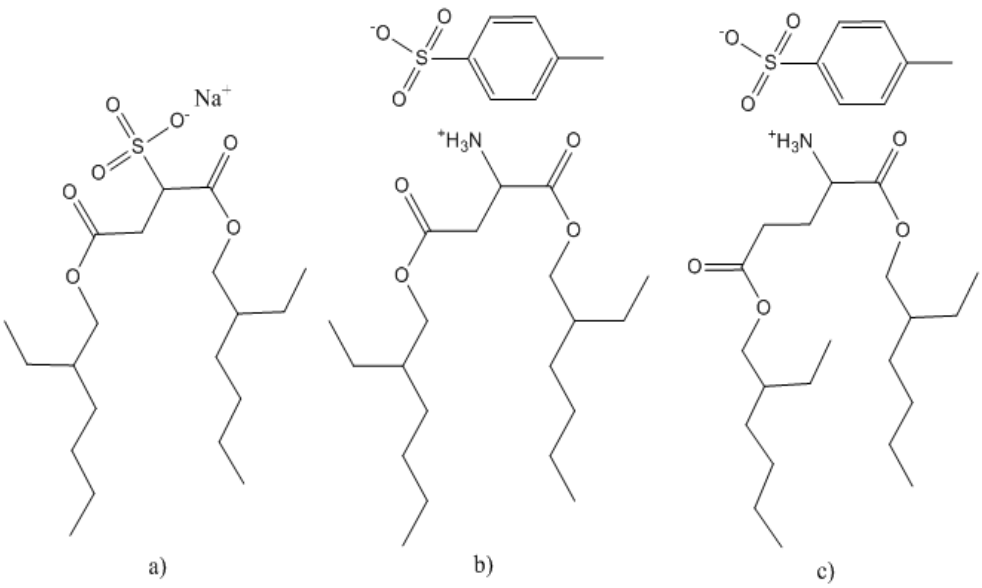

Figure 3.1. Structure of a) dioctyl sulfosuccinate sodium (AOT), b) $(C_8b)_2$-Asp-PTS, and c) $(C_8b)_2$-Glu-PTS.

These surfactants were then dissolved in anhydrous dodecane (Alfa Aesar). Water was removed from the dodecane solvent with the aid of molecular sieves until the

solvent water content was below 10 ppm. Rotary evaporation and vacuum drying were also used to dehydrate the commercial and synthesized surfactants. All solutions were nitrogen sparged prior to the start of the experiment to minimize water content to below 10 ppm.

The AOT analog surfactants $(C_8b)_2$-Asp-PTS and $(C_8b)_2$-Glu-PTS were synthesized using an esterification reaction of two 2-ethyl-1hexanol by an amino acid. Aspartic and glutamic acids were chosen because they resulted in reaction products that closely resembled AOT. The reaction is catalyzed by *para*-toluene sulfonic acid, which remains in the product as the surfactant counterion. The synthesis is carried out under reflux in toluene for 4 hours to remove water from the reaction product with each reaction yielding about 10g of product. Purification of the product was accomplished through flash column chromatography (Combiflash) in a silica gel column and subsequent rotary evaporation for 5 hours. Confirmation of the surfactant molecular mass was accomplished through electrospray ionization (Thermo Scientific LTQ-XL Linear Ion Trap Mass Spectrometer). All synthesized surfactants were stored in a lyophilizer for one week prior to use to allow evaporation of any volatile impurities.

2.2.2 Methods

The cell used in the impedance spectroscopy experiments consists of two glass slides coated sequentially with a 100 nm thickness layer of indium tin oxide (ITO) and a 33 nm thickness layer of fluoropolymer. The fluoropolymer layer was deposited in a plasma polymerization process of a C_4F_8 precursor using a STS Multiplex DRIE ICP system. A wire lead was attached to one end of each impedance slide using silver epoxy (MG Chemicals). The cell assembly process was as reported in Chapter 2. The

two ITO slides are held apart at a uniform gap distance with about 18 μL of surfactant solution injected in between. The gap is maintained with the aid of 8 μm silica spacer beads that are added to the surfactant solution at a concentration of 0.2 mg/mL. Next, the impedance cell is connected to a VersaSTAT 3 potentiostat (Princeton Applied Research) equipped with a Low Current Interface. The potentiostatic procedure is as described in previous works.[10] The exact geometry of the impedance cell gap is calculated by calibrating the dielectric constant derived from the impedance spectra to the literature value for dodecane.[13] Measures were taken to limit water exposure from the ambient air by assembling the impedance cells in a nitrogen inflated glove bag (Sigma-Aldrich) and conducting the impedance spectroscopy experiment in a nitrogen blanked Faraday cage.

The analysis method for the impedance spectra has been rigorously described by prior papers in the literature.[10,11] The equivalent circuit for the experimental set up is as presented in Chapter 2 and results in the following expression for the imaginary component of the impedance Im(Z).

$$\frac{Im(Z)}{R_f} = \frac{[2b + 2(4b+1)c + 4(2b+1)c^2]\Omega^{-1} + (2b+1)\Omega}{1 + 4c + 4c^2 + \Omega^2} \tag{3.1}$$

where

$$b = \frac{C_g}{C_{fp}}, \quad c = \frac{C_g}{C_{dl}}, \quad and \quad \Omega = \omega R_f C_g$$

The value of C_{fp} is defined as

$$C_{fp} = \frac{\varepsilon_{fp} A_f}{\lambda_{fp}}$$

where the value of ε_{fp} is determined from a dielectric constant of 2.3 as observed from capacitance measurements of a plasma polymerized layer of C_4F_8.[14] The value of the thickness of the fluoropolymer coating (λ_{fp}) is 33 nm as measured from white light

interferometry (Zygo).

The parameters C_g, C_{dl}, and R_f are related to the fluid electrical properties by the following equations.

$$R_f = \frac{d}{A_f K} \tag{3.2}$$

$$C_g = \frac{\varepsilon_f A_f}{d} \tag{3.3}$$

$$C_{dl} = \frac{\varepsilon_f}{\lambda_D} \cosh\left(\frac{e\xi}{2k_B T}\right) \tag{3.4}$$

where d is the gap distance between the electrodes, A_f is the area of the solution held between the two electrodes, K is the conductivity of the solution, and ζ is the zeta potential of the electrode surface. The equation for C_{dl} assumes that all charge carriers are 1-1 electrolytes and is derived from the Guoy-Chapman model for a diffuse layer of charge accumulated at each electrode. The ionic strength of the bulk fluid can then be calculated from equation (3.5).

$$\lambda_D = \sqrt{\frac{\varepsilon_f k_B T}{2e^2 n_0}} \tag{3.5}$$

Where ε_f is the permittivity of the solution, k_B is Boltzmann's constant, T is absolute temperature, e is the charge on one proton, and n_0 is the ionic strength (number per volume). Ultimately, the conductivity and ionic strength of the sample is used to determine the diffusion coefficient (D) and hence the hydrodynamic radius of charge carriers from the Stokes-Einstein relation.

$$D = \frac{k_B T K}{2n_o e^2} \tag{3.6}$$

C_g, C_{dl}, and R_f, are obtained from the extrema of the imaginary component of the

impedance spectra. The roots of the derivative dIm(Z)/dΩ of equation (3.1) were obtained and then substituted back into equation (3.1). Thus the ratio between the Im(Zmin) and Im(Zmax), $r_{Im(Z)}$ is determined to be

$$r_{Im(Z)} = \frac{Im(Z_{min})}{Im(Z_{max})} = \frac{(1-s)(3+s)\sqrt{1+s-4[(2c+1)b+c]}}{(1+s)(3-s)\sqrt{1-s-4[(2c+1)b+c]}} \quad (3.7)$$

where *s* is defined as:

$$s = \sqrt{1-16[(2c+1)b+c]} \quad (3.8)$$

Plotting Im Z versus ω (radians/second) of fluoropolymer electrodes in the high frequency range, an electrode capacitance, C_E, can be fit using a least squares regression with Origin (OrginLab Corp) as described in Chapter 2**.** This C_E is related to C_g and C_{fp} according to the equation below.

$$\frac{1}{C_E} = \frac{1}{C_g} + \frac{1}{C_{fp}} \quad (3.9)$$

Once C_g is inferred, C_{dl} is determined from equation (3.7) through deriving a suitable value for *c* from the experimental value of $r_{Im(Z)}$. Finally, R_f can be calculated iteratively from equation (3.1) by fitting it to the local maximum of the Im(Z) spectra and known values of *b, c*, and C_g.

In order to calculate the number of charge carriers in solution from the impedance spectra, Zetaspin™ experiments were necessary to determine the zeta potential of the fluoropolymer coated ITO slides. Zetaspin™ involves measurement of the streaming potential between two inert, glassy carbon electrodes immersed in surfactant solution. The software (LabVIEW, National Instruments) then calculates the zeta potential of the electrode surface from the measured streaming potential.[15] The sample preparation and procedure for these Zetaspin™ experiments were as described

by the previous work.[15] All solutions were maintained at a water content below 10 ppm according to a coulometric Karl-Fisher water titrator.

To compare the EIS derived charge carrier sizes to the hydrodynamic micelle size, dynamic light scattering experiment were performed on the surfactant solutions. A Malvern ZetaSizer Nano ZSP (Malvern Instruments, Malvern, UK) used phase analysis light scattering (PALS) to correlate temporal scattering fluctuations to hydrodynamic size information. All solutions were sparged with nitrogen and prepared in a nitrogen glove bag to keep the water content below detectability limit at all times. Sparging times varied between 30 minutes to 3 hours depending on surfactant and ambient humidity conditions. Both solvent and solution were filtered prior to light scattering using a 250 nm PTFE syringe filter (VWR International).

SANS measurements were carried out on the NGB 10 m small-angle neutron scattering instrument at the NIST Center for Neutron Research in Gaithersburg, MD, USA. Samples were loaded into 2mm path length demountable titanium cells with quartz windows and Teflon o-rings. Three instrument configurations with neutron wavelengths $\lambda = 6$ Å^{-1} or 10 Å^{-1} and a wavelength spread $\frac{\Delta\lambda}{\lambda} = 0.14$ were utilized to collect SANS spectra covering a *Q*-range from 0.004 Å^{-1} to 0.5Å^{-1}, where $Q = \frac{4\pi}{\lambda}\sin\theta$ is the scattering wave vector and 2θ the total scattering angle. After accounting for transmission, background, empty cell scattering, and detector efficiency, the data were reduced to absolute scale using standard NCNR reduction macros in Igor Pro.[16]

3.3 Results and Discussion

3.3.1 Surfactant Conductivity

Surfactant conductivity has been widely measured in the literature as an easy

way to characterize the charging behavior of micelles in nonpolar liquids. A popular mechanism for the origin of charge and hence conductivity in surfactant solutions is the disproportionation theory.[3] In this model, two neutral micelles undergo a Brownian collision such that a dissociated ion is exchanged between the two micelles. The two neutral micelles thus leave the collision as one positively charged micelle and one negatively charged micelle. One important assumption in the disproportionation model is that surfactant chemistry does not impact the charging behavior of micelles. Prior work in the microemulsion community has observed the strong dependence of bulk conductivity values to the ratio of water to surfactant molecules in solution. This behavior is often modeled in the literature by a charge fluctuation model introduced by Eicke *et al.*[12] The charge fluctuation model is based solely on micelle size and predicts that the likelihood of a micelle acquiring charge after a collision increases with its size. As the water to surfactant ratio increases, the micelles become swollen with water resulting in more micelles acquiring charge and raising the overall conductivity of the solution. Despite the simplicity of this one parameter model, Eicke et al. found good agreement between the predicted and experimental conductivity for Na-AOT micelles larger than 16 nm in iso-octane.[12] Later refinements to Eicke's model by Hall et al. resulted in good agreement between predicted and measured conductivity of Na-AOT in iso-octane for micelle sizes as small as 3 nm.[17] It is important to note however, that these measurements were taken in water logged surfactant solutions with measurements taken at ambient humidity.

A Model DT non-aqueous conductivity meter (Dispersion Conductivity Inc.) was used to compare the molar conductivity values of the synthesized AOT anlog

surfactants with several other commercial surfactants soluble in dodecane. The molar conductivities of the commercial surfactant solutions shown in **Figure 3.2** reveal the strong dependence between micelle size and molar conductivity.

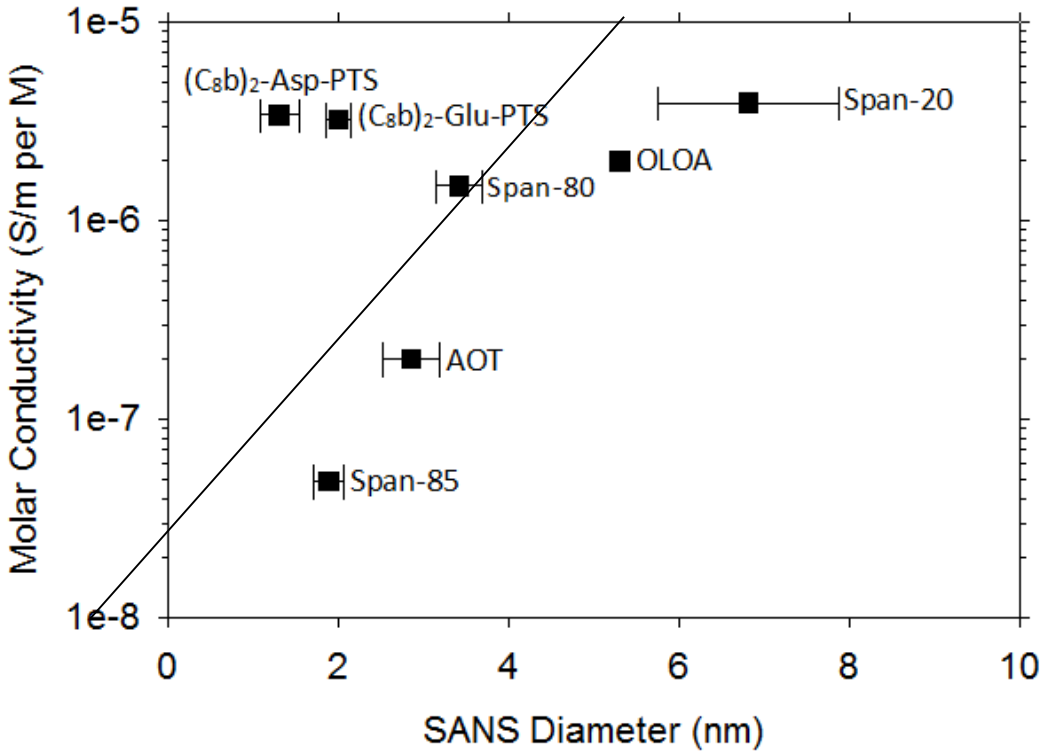

Figure 3.2. Molar conductivity of synthesized AOT analogs and several commercial surfactants in dodecane. Micelle diameters from small-angle scattering experiments of OLOA[18] and the Span[19] surfactants are taken from literature. The black line is meant to guide the eye and is not a linear fit of the data.

Examining the synthesized surfactants consisting of AOT (Sigma-Aldritch), OLOA (Chevron), and Spans (Croda International), a clear trend between molar conductivity and micelle diameter emerges. For the commercial surfactants AOT, OLOA, and the Spans, the molar conductivity increases with surfactant size. This is consistent with the charge fluctuation model of micelle charging in which the probability of a micelle becoming charged is solely reliant on the size of micelles in solution.[20] Meanwhile, the synthesized AOT analog surfactants have the largest molar conductivities while forming micelles of the smallest sizes. This type of charging

behavior directly contradicts the charge fluctuation theory and distinguishes the synthesized AOT analogs from all commercial surfactants. EIS experiments reveal that the large molar conductivity of the AOT analogs is attributed to ionic strength rather than micelle size. AOT analogs form a greater number of charged micelles in solution than commercial surfactants. As seen in **Figure 3.2**, AOT follows the same charging trends as the nonionic surfactants OLOA and the Spans which suggests that the sodium counterion of AOT is too tightly bound to the surfactant to be dissociated. As a result, AOT behaves as a nonionic surfactant despite the presence of the sodium counterion. In contrast, the AOT analog surfactants have bulky organic PTS counterions which could dissociate more easily and have higher solubility in the non-polar solvent, both potentially resulting in, a larger ionic strength than AOT. The difference in charging behavior of $(C_8b)_2$-Asp-PTS and $(C_8b)_2$-Glu-PTS from commercial surfactants is accentuated in **Figure 3.3**.

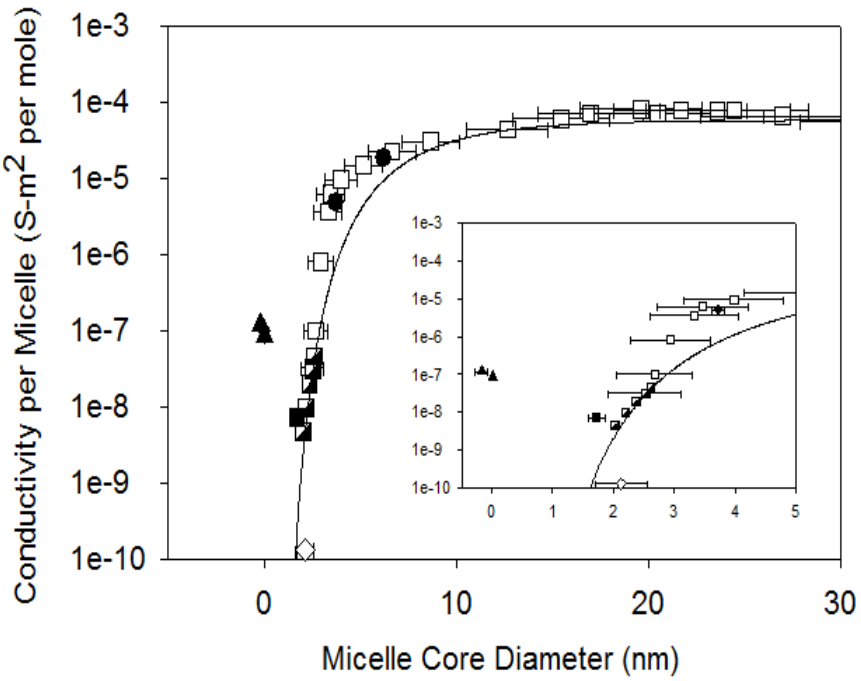

Figure 3.3. Conductivity per micelle as a function of micelle diameter for sodium AOT

from Berg (half-filled squares),[21] Eicke (open squares),[12] and experiment (closed squares), sodium DEHP (closed squares),[22] calcium AOT (open diamond), and AOT analogs (closed triangles). Line is charge fluctuation theory predictions from Hall.[17] All AOT and DEHP surfactants agree with theory while AOT analog data do not.

The solid line in **Figure 3.3** illustrates conductivity per micelle as calculated from Hall's refinement of Eicke's charge fluctuation theory.[17] Hall's modification accounts for the discretization of charge and uses the micelle core radius as the basis of its derivations. Literature data of sodium AOT and its phosphate analog sodium bis(2-ethylhexyl)phosphate (DEHP) suspensions fit remarkably well with theory for micelles as small as 3 nm. A conductivity probe (Dispersion Conductivity Inc.) was used to measure conductivity of Na AOT, Ca AOT, and the AOT analogs. These values agreed well with the theory with the exception of the AOT analogs $(C_8b)_2$-Asp-PTS and $(C_8b)_2$-glu-PTS. The conductivity of the AOT analogs are many orders of magnitude higher than predicted despite having the smallest micelle size. This directly contradicts the charging behavior predicted by charge fluctuation theory and reveals charging phenomenon unaccounted for by current theories in the literature. It is important to note, however, that the model approaches a vertical slope at small micelle sizes. Any conductivity predictions will therefore vary several orders of magnitude with nanometer deviations in micelle size.

Conductivity values of surfactant solutions can also be derived from measurements of electrical resistance during EIS. Fluid resistances (R_f) from the impedances data were fit according to equation (3.1). The conductivity of the surfactant solutions was then derived from R_f and the overlap area of the impedance cell according to equation (3.2). The impedance derived conductivity of each surfactant solutions is shown in **Figure 3.4**.

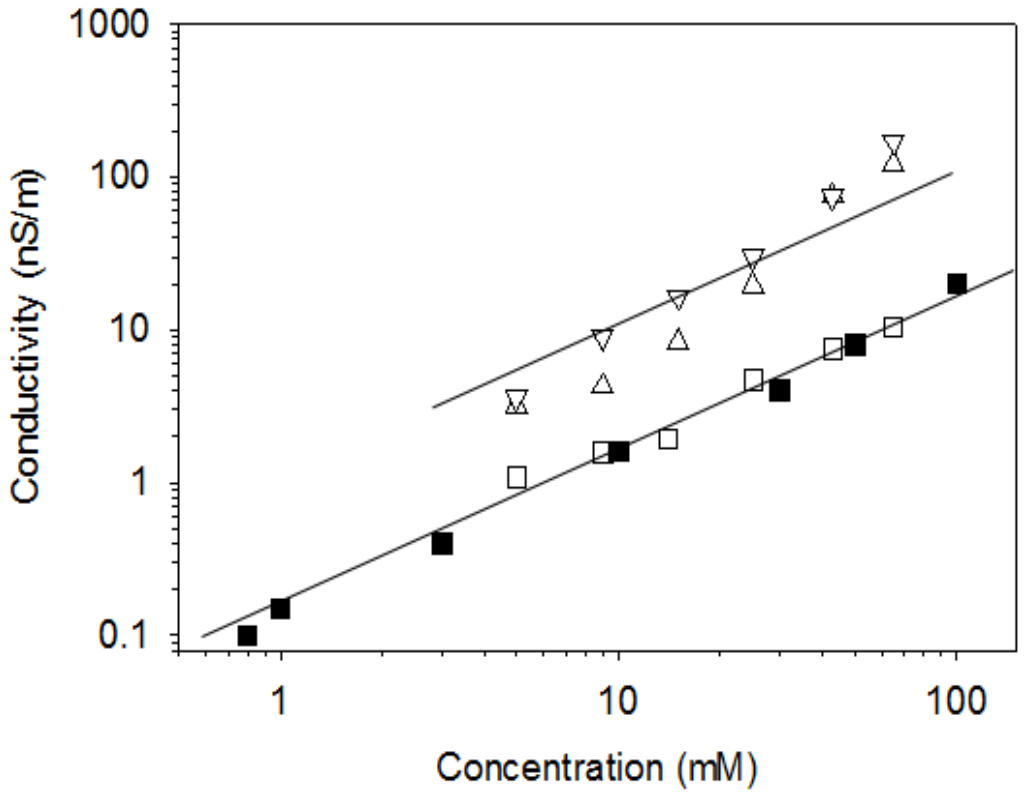

Figure 3.4. Conductivity of sodium AOT (open squares), $(C_8b)_2$-Glu-PTS (open upright trianges), and $(C_8b)_2$-Asp-PTS (open inverted triangles) with trend lines of slope 1. Conductivity values of AOT in dodecane from experiments by Dufresne and Bartlett are shown as filled squares.[7,8]

The conductivity behavior of AOT with respect to surfactant concentration is well documented in the literature. EIS conductivity measurements of AOT match those taken by a commercial conductivity meters.[7,8] Regression of the conductivity versus AOT concentration data yields a line of slope unity just as observed by Dufresne and Bartlett.[7,8] Of particular interest is that the literature and experimental conductivities of AOT match despite the differences in sample preparation and water content of solution. Water was rigorously excluded from the EIS experiments such that the water content was maintained below 15 ppms at all times while experiments described in the literature were conducted under ambient humidity. Overall however, the good agreement between the experimental and literature results indicates that the impedance model

described by equation (3.1) accurately describes the charge transfer processes in the impedance cell. EIS is therefore a reliable and reproducible method to determine conductivity of surfactant doped nonpolar solutions.

Examining the trends in **Figure 3.4**, the conductivities of all three surfactants were found to be proportional to the total surfactant concentration. While the chemical structures of all three surfactants are similar, the AOT analog solutions were an order of magnitude more conductive than AOT solutions of the same concentration. The AOT data is well fit by a line of slope unity while the AOT analog slopes are not. The AOT conductivity behavior correlates with predictions from the disproportionation model of micelle charging and suggests that surfactant chemistry does not play a role in micelle charging of AOT. As the concentration of $(C_8b)_2$-Asp-PTS and $(C_8b)_2$-Glu-PTS increase, the solution conductivity increases by a proportionality constant that is steeper than unity. This behavior implies that surfactant chemistry is a crucial determinant of the charging behavior of AOT analogs.

3.3.2 Ionic Strength

The ionic strengths of surfactant solutions were derived from the capacitance of the double layer (C_{dl}) and the zeta potential (ζ) of the electrode surface according to equations (3.4) and (3.5). Ionic strengths for AOT and the AOT analogs are shown in **Figure 3.5**.

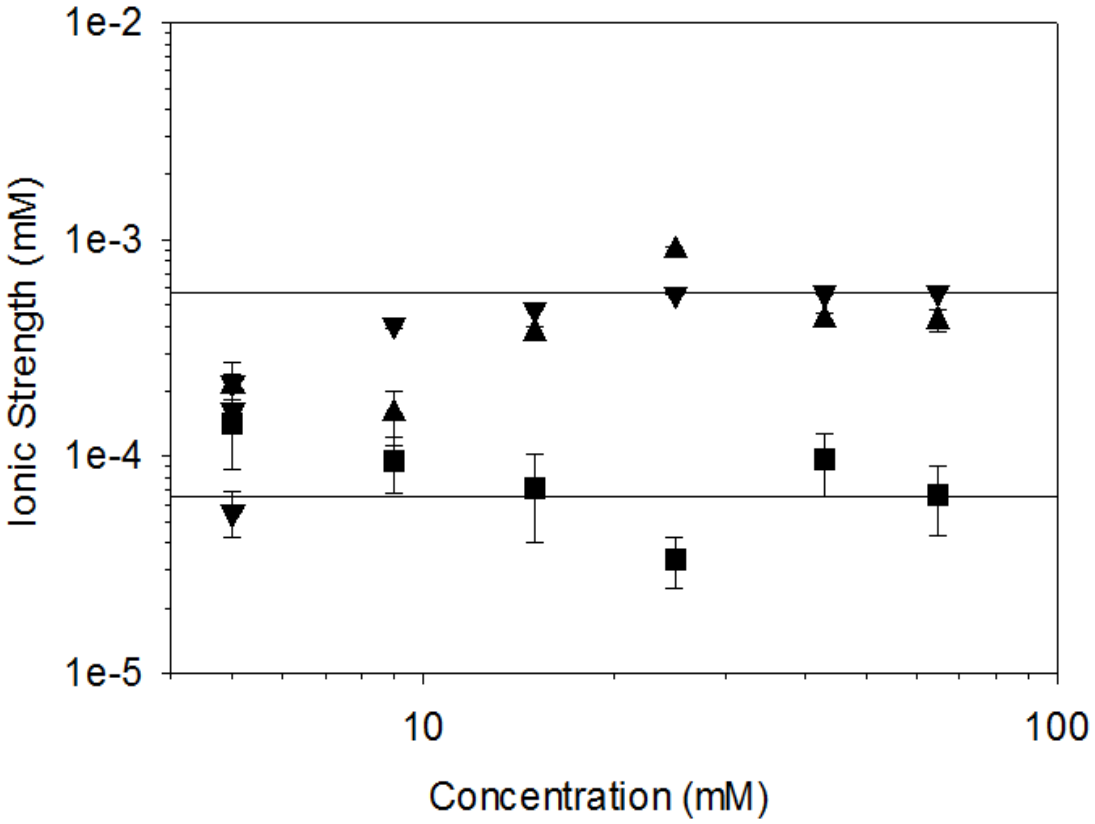

Figure 3.5. Ionic strength of AOT (squares), $(C_8b)_2$-Glu-PTS (upright triangles), and $(C_8b)_2$-Asp-PTS (inverted triangles). Horizontal lines represent the average ionic strength of surfactant concentrations above 15 mM.

Figure 3.5 indicates that the ionic strengths of all three surfactant solutions plateaus to a constant value at surfactant concentrations above 15 mM. For the AOT analog surfactants, this ionic strength plateau is $6 \pm 1 \times 10^{-4}$ mM while for the AOT surfactants, it is $7 \pm 3 \times 10^{-5}$ mM. The low ionic strength and charged micelle population is responsible for the low conductivity of nonpolar solutions compared to typical aqueous solutions. Using an AOT aggregation number of 22 from neutron scattering experiments, only 60 ppm of total micelles are charged at a surfactant concentration of 25 mM.[23] Assuming the same aggregation number for the AOT analog surfactants, the number of charged micelles in an equivalent concentration of AOT analog solution is 500 ppm.

From **Figure 3.1**, the chemical structures of AOT and the AOT analog surfactants are identical with the exception of a much bulkier counterion and slightly smaller head group for the AOT analog surfactants. The ionic strength data shown in **Figure 3.5** indicate that these small changes in chemical structure strongly affect the number of charged micelles in solution. One possibility for the observed charging behavior is that the dissociation likelihood of sodium AOT is less than that of $(C_8b)_2$-Glu-PTS or $(C_8b)_2$-Asp-PTS. The larger surface charge density of a tiny sodium counterion compared to the larger sized PTS counterion could result in sodium counterions being more tightly bound to their surfactant counterparts than PTS counterions. PTS counterions are also more nonpolar in nature than sodium and may allow for easier dissociation into the dodecane solvent. Another notable trend in **Figure 3.5** is the relative insensitivity of the ionic strength to surfactant concentration. There are a few possible explanations for this phenomenon. The charge carriers in solution are essentially becoming saturated despite the addition of more surfactant. This could arise when the solution is sufficiently saturated such that the collision rate between neutral micelles is equal to the recombination rate of two charged micelles. Another possibility is that the number of charge carriers is limited by the severely dehydrated nature of the surfactant solutions. Low water content could prevent dissociation of ions in the polar core resulting in no ions being available for exchange during micelle collisions.

3.3.3 Micelle Size

Micelle size was derived using three different experimental methods for comparison purposes. The hydrodynamic diameter of charged micelles was obtained from conductivity and ionic strength values from EIS and equation (3.6). Hydrodynamic

size information for the entire micelle population, both charged and neutral, was evaluated from dynamic light scattering (DLS) experiments. The comparison between these two different techniques for the AOT and AOT analogs are shown in **Figure 3.6** and **Figure 3.7** respectively.

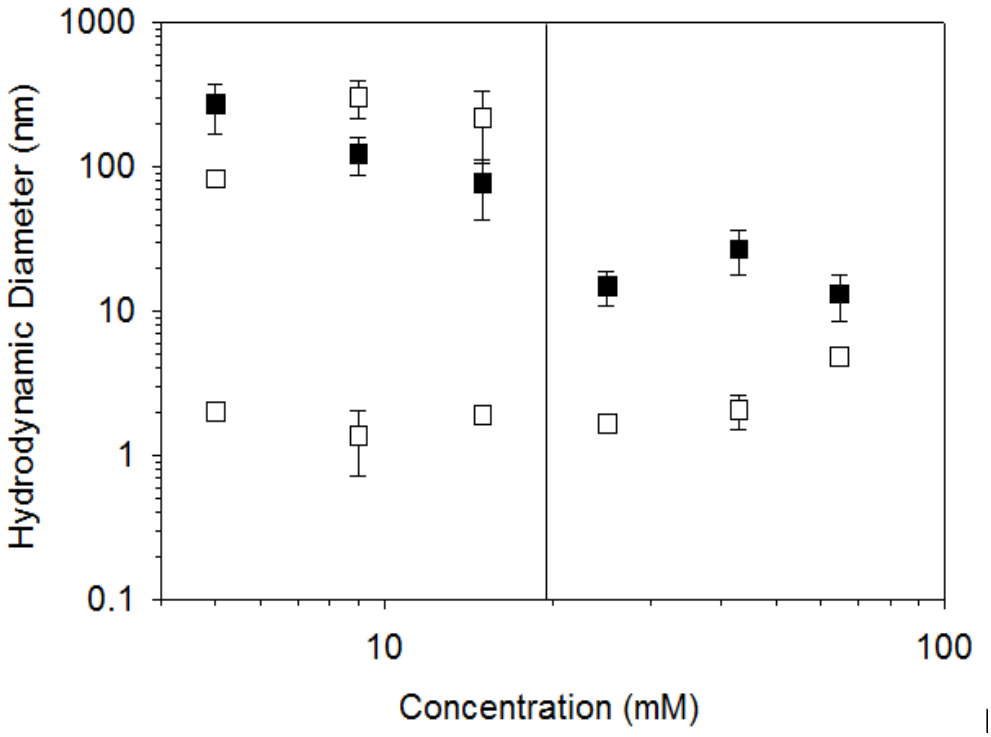

Figure 3.6. Hydrodynamic diameter of AOT micelles in dodecane obtained from EIS (filled squares) and DLS (open squares) experiments. The DLS results are the number average micelle diameters while the EIS results are the sizes of charged micelles. The black line indicates a transition from a bimodal to unimodal micelle population at a surfactant concentration between 15 mM and 25 mM.

Examining the EIS results in **Figure 3.6**, the hydrodynamic size of the charged AOT micelles decrease with surfactant concentration. This trend arises because the conductivity of the AOT solutions increase with concentration while the ionic strength remains relatively constant. The increase in conductivity with surfactant concentration results from smaller charge carriers being able to travel faster through the solvent rather than an increase in the overall ionic strength. The decrease in charge carrier size with concentration is also corroborated by the dynamic light scattering data. At AOT

concentrations below 15 mM, the raw correlation functions from DLS displayed two distinct delay times which is characteristic of a bimodal population distribution. The AOT micelles appear to form a smaller micelle population of about 2 nm in diameter in addition to a larger sized micelle population that is about 200 nm in diameter. The larger sized micelle population might be vesicle or rod type structures that have been observed in DLS of aqueous surfactant emulsions.[25] Comparisons between the EIS and DLS size data indicate that at AOT concentrations below 15 mM, the larger of the two micelle populations are the bearers of charge. This agrees well with previous experimental results from the surfactant doped nonpolar liquid and microemulsion literature. Yezer et al. have reported that the largest micelles in a unimodal population distribution are the bearers of charge for the surfactant OLOA in dodecane.[10] Such trends are also common in the microemulsion literature where this behavior is rationalized in terms of charge fluctuation theory. Above 15 mM, the DLS data in **Figure 3.6** show a transition from a bimodal micelle distribution to a unimodal one. The larger of the two micelle populations disappears until only the micelles with a number average diameter of 2 nm remain. Meanwhile, the EIS results indicate that the charged micelles are about 10 nm in diameter and are significantly larger than the average micelle diameter of 2 nm. The observation of the largest micelles in the population being the bearers of charge thus continues to persist even as the micelle distribution transitions from bimodal to unimodal. Such behavior emphasizes the importance of experimental techniques that are sensitive to charged micelles rather than the entire micelle population. As shown in **Figure 3.6**, the DLS data alone do not reveal the charging trends in surfactant doped nonpolar liquids because the charged micelles consist of only

a fraction of the entire micelle population.

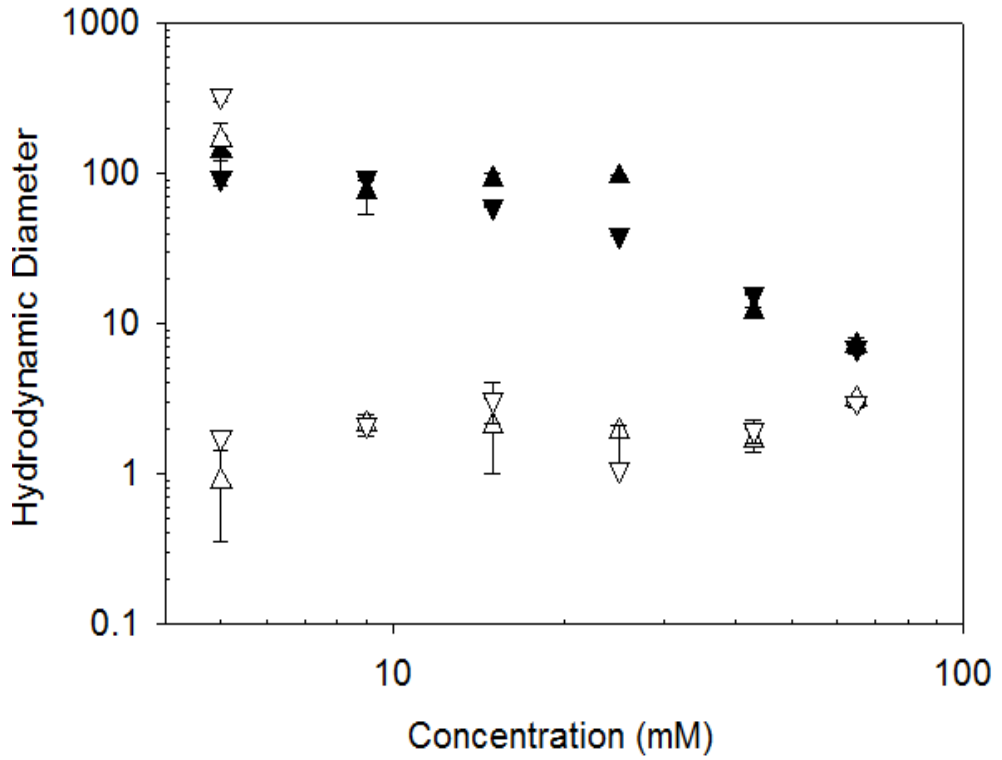

Figure 3.7. Hydrodynamic diameter of $(C_8b)_2$-Glu-PTS (upright triangles) and $(C_8b)_2$-Asp-PTS (inverted triangles) micelles obtained from EIS (closed symbols) and DLS (open symbols). DLS results are sensitive to entire micelle population while EIS results refer to charged micelles only.

The hydrodynamic diameters of the AOT analogs are shown in **Figure 3.7** with similar behavior between the two surfactants. The EIS derived sizes of the charged micelles indicate that the charged micelles decrease in size with surfactant concentration. This is consistent with the behavior of charged AOT micelles and reveals that the increase in solution conductivity with surfactant concentration is again due to smaller micelles being able to migrate faster through the organic solvent. The DLS results in **Figure 3.7** demonstrate that there is a bimodal to unimodal micelle distribution transition occurring between a surfactant concentration of 5 mM and 9 mM. Furthermore at concentrations where the micelles form a bimodal distribution, the EIS experiments indicate that the larger population of micelles are the bearers of charge. At

concentrations above 9 mM, the micelles of $(C_8b)_2$-Glu-PTS and $(C_8b)_2$-Asp-PTS are assembled into a unimodal population distribution. A close examination of the DLS derived micelle population distribution reveals no micelles in the size range indicated by EIS for surfactant concentrations between 9 mM to 25 mM. This could be due to a variety of instrument related limitations such as the low refractive index contrast between the surfactant and solvent as well as the signal noise occurring in the correlation function at delay times indicative of larger sized structures. To circumvent such light scattering related challenges, neutron scattering experiments of AOT and $(C_8b)_2$-Asp-PTS were conducted as shown in **Figure 3.8** and **Figure 3.9**.

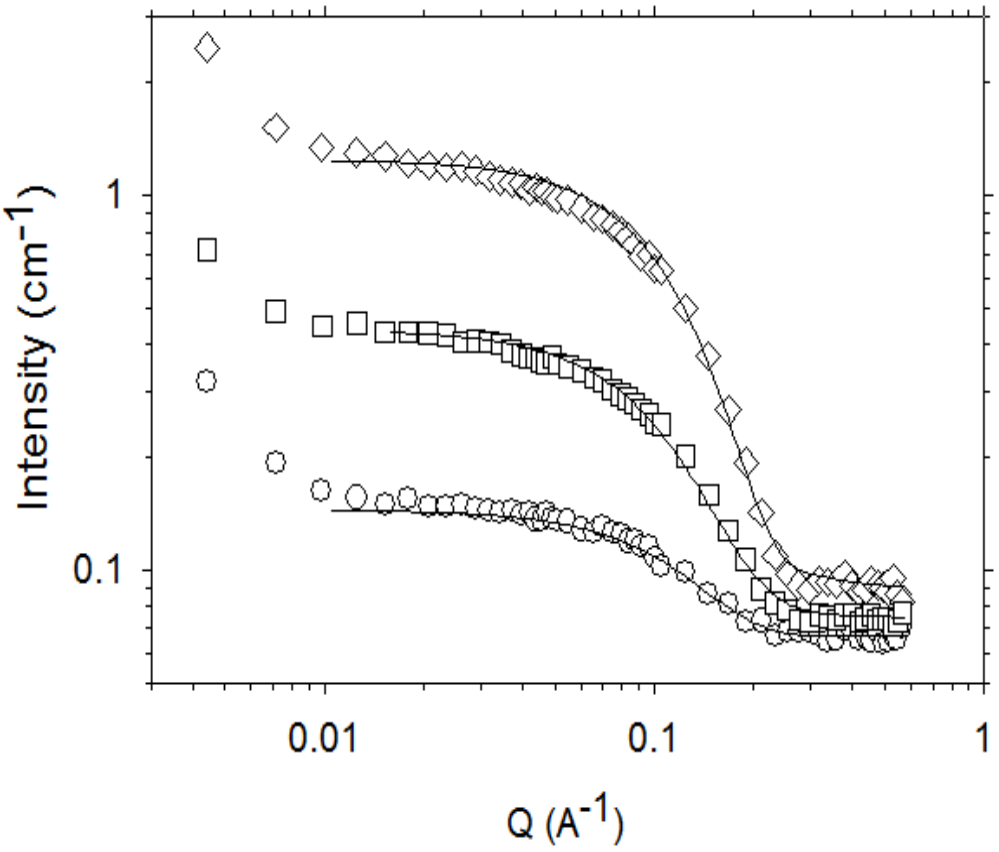

Figure 3.8. Intensity as a function of the scattering vector Q for a small angle neutron scattering experiment of 5 mM (open circles), 20 mM (open squares), and 65 mM (open diamonds) AOT in dodecane. Model fitting of the data to a Schultz distribution of spherical micelles are shown as lines.

All surfactants formed reverse micelles in solution that were well modeled by a spherical form factor with a small Schultz polydispersity. The neutron scattering data for AOT is shown in **Figure 3.8** where the intensity data is fit by spherical models with an average radius of 14 ± 2 angstroms and an average Schultz polydispersity of .21 ± 0.07. Overall, the model fits are consistent with previous neutron scattering experiments for AOT in the literature.[23,24] As corroborated by the light scattering data, the AOT micelle population at around 3 nm persists at all surfactant concentration. The upturn in intensity at low Q in **Figure 3.8** provides evidence for the existence of AOT structures larger than the 3 nm spherical micelles. Thus, the neutron scattering experiments of AOT in dodecane reveal the presence of larger aggregates in solution consistent with the bimodal distribution seen in the dynamic light scattering data.

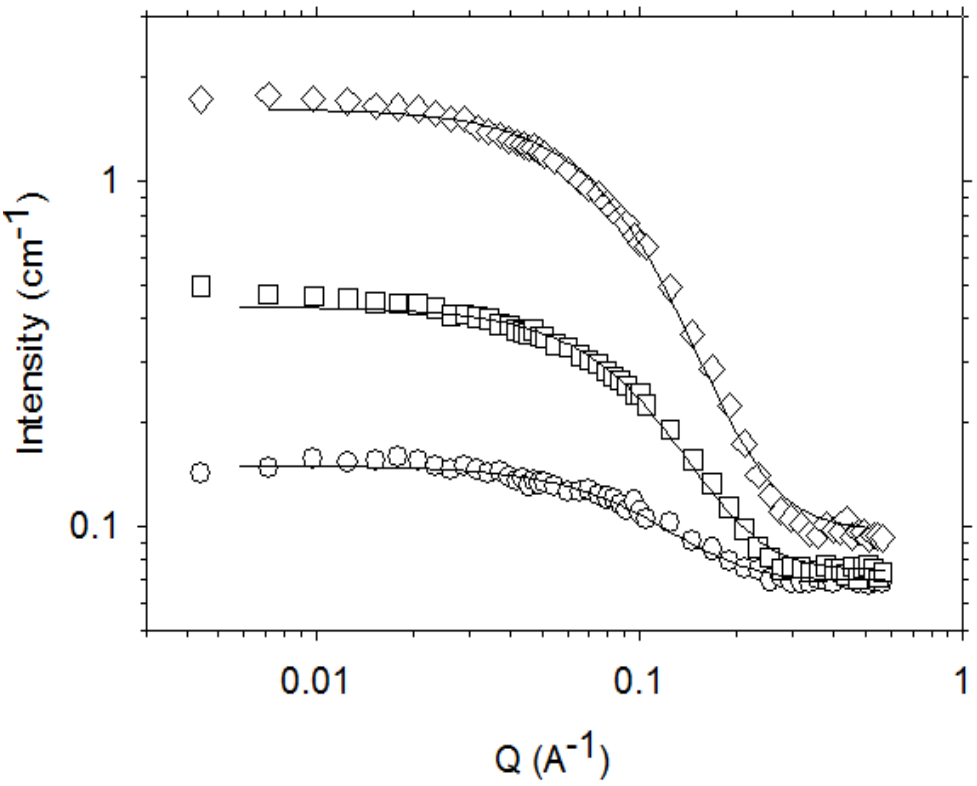

Figure 3.9. Intensity as a function of the scattering vector *q* for a small angle neutron

scattering experiment of 5 mM (open circles), 20 mM (open squares), and 65 mM (open diamonds) ($C_8b)_2$-Asp-PTS in dodecane. Model fitting of the data to a Schultz distribution of spherical micelles are shown as lines.

The intensity as a function of scattering vector Q data for ($C_8b)_2$-Asp-PTS is shown in **Figure 3.9**. The intensity data in **Figure 3.9** were fit with spherical form factors of average radius 7 ± 1 angstroms and average Schultz polydispersity of 0.6 ± 0.1. A micelle size distribution was calculated from the EIS data and the Schultz polydispersity of this hypothetical micelle distribution compared with the SANS results. First, the fraction charged of the micelle population was determined from the ionic strength and micelle concentration. Next, a Schultz distribution was derived that matched the fraction charged calculated from EIS. Such calculations yielded an average Schultz polydispersity of 0.8 ± 0.1 which is within experimental error of the polydispersity obtained from SANS measurements.

The SANS measurements for AOT and the AOT analogs reveal large sized aggregates consistent with the bimodal population seen in dynamic light scattering experiments; however, the SANS data do not show a strict transition from a bimodal to unimodal micelle distribution as observed in the dynamic light scattering data. One possibility to reconcile the SANS and DLS results is by considering the contrast and signal strength differences between the two experimental methods. From the ionic strength data, it is clear that the charged micelle fraction is less than one percent, and that the charged fraction are comprised of the largest micelles in the total distribution regardless of the distribution shape. Due to the low contrast in refractive index between surfactant and solvent, the dynamic light scattering experiments may not be sensitive enough to track the charged micelle population especially as they are so few in number.

In contrast, there is much better resolution between the solvent and the surfactant in SANS experiments due to the usage of deuterated solvent. Another difference between the SANS and DLS data is that the large micelle sizes measured using DLS was not the same values as those measured by SANS. One possibility of resolving this discrepancy is that the *q* range was instrumentally limited. The large AOT micelles had diameters between 100 and 300 nm on DLS which corresponds to a *q* of 0.006 to 0.002 A^{-1}. As observed in **Figure 3.8**, there is an increase in the scattering intensity around *q* = 0.006 A^{-1}; however, there was not enough data around that *q* range to obtain a full fit for the structures in that *q* range. The large $(C_8b)_2$-Asp-PTS micelles had diameters ranging from 300 to 400 nm which corresponds to a *q* range of 0.002 to 0.0016 A^{-1}. Such scattering vector (A) ranges are below the instrumental resolution shown in **Figure 3.9**. Overall, the different micelle size distributions measured by the SANS and DLS experiments emphasize the challenge of isolating charged micelle behavior from that of the total micelle population. EIS is therefore a more direct measurement of the charging behavior of micelles in nonpolar liquids. Ultimately, AOT and its two synthesized analogs form similarly sized micelles in solution indicating that conductivity related differences between the three surfactants are due to surfactant and counterion chemistry rather than micelle size.

3.4 Conclusions

Previous literature experiments regarding surfactant charging in nonpolar media have focused on proprietary surfactants. While of industrial importance, these surfactants are often low purity and offer little systematic differences in surfactant chemistry. Through development of a high purity, synthetic technique for AOT analog

surfactants, we isolate and demonstrate specific relationships between counterion chemistry and micelle charging behavior. Two AOT analog surfactants were synthesized, and their charging properties were measured using impedance spectroscopy. Comparing charging behavior of AOT and AOT analogs reveal novel relationships between counterion hardness and charged micelle formation.

The major structural difference between AOT and its synthetic analogs was counterion hardness. The synthesized analogs had a larger, hydrophilic para-toluene sulfonate counterion while the commercial AOT surfactants had smaller, highly ionic metal counterions. The change in counterion chemistry resulted in the AOT analogs having conductivities and ionic strengths that were an order of magnitude larger than those of sodium AOT. The dramatic increase in charging efficiency could not be modeled with the leading disproportionation and charge fluctuation theories for charged micelle formation. In contrast, AOT surfactants with harder metal counterions of sodium or calcium have similar conductivities per micelle and are readily fit by the charge fluctuation model.

Water was carefully monitored and controlled to be below 10 ppm at all times during the course of impedance spectroscopy experiments. Despite the efforts taken to remove water from the surfactant solutions, water was found to have little effect on the charging properties of sodium AOT compared to those obtained from ambient humidity experiments from the literature.

3.5 Acknowledgements

We thank Norman Gottron and Mason Risley at the Carnegie Mellon Nanofabrication Facility for the plasma deposition expertise and manufacturing of the

C_4F_8 coating. Thanks to Bugra Ozutemiz and Dr. Burak Ozdoganlar at the mechanical engineering department at Carnegie Mellon for access and training on the white light interferometer. Another thank you to John Riley at NIST for the SANS measurements and undergraduate researcher Katrina Wang for synthesis of the AOT analogs. We also gratefully acknowledge financial support through NSF grant #1511619.

3.6 References

(1) Nikakhtari, H.; Vagi, L; Choi, P.; Liu, Q.; Gray, M. R.; Univ, A. Solent Screening For Non-Aqueous Extraction of Alberta Oil Sands. *Can. J. Chem. Eng.* **2013**, *91* (6), 1153–1160.

(2) Jones, S. A.; Martin, G. P.; Brown, M. B. Manipulation of Beclomethasone-Hydrofluoroalkane Interactions Using Biocompatible Macromolecules. *J. Pharm. Sci.* **2006**, *95* (5), 1060–1074.

(3) Morrison, I. D. Electrical Charges in Nonaqueous Media. *Colloids and Surfaces A: Physicochemical and Engineering Aspects*. 1993, pp 1–37.

(4) Michor, E. L.; Berg, J. C. Temperature Effects on Micelle Formation and Particle Charging with Span Surfactants in Apolar Media. *Langmuir* **2015**, *31* (35).

(5) Gacek, M. M.; Berg, J. C. Effect of Surfactant Hydrophile-Lipophile Balance (HLB) Value on Mineral Oxide Charging in Apolar Media. *J. Colloid Interface Sci.* **2015**, *449*, 192–197.

(6) Espinosa, C. E.; Guo, Q.; Singh, V.; Behrens, S. H. Particle Charging and Charge Screening in Nonpolar Dispersions with Nonionic Surfactants. *Langmuir* **2010**.

(7) Hsu, M. F.; Dufresne, E. R.; Weitz, D. A. Charge Stabilization in Nonpolar Solvents. *Langmuir* **2005**.

(8) Kemp, R.; Sanchez, R.; Mutch, K. J.; Bartlett, P. Nanoparticle Charge Control in Nonpolar Liquids: Insights from Small-Angle Neutron Scattering and Microelectrophoresis. *Langmuir* **2010**.

(9) Dukhin, A.; Parlia, S. Ions, Ion Pairs and Inverse Micelles in Non-Polar Media. *Curr. Opin. Colloid Interface Sci.* **2013**, *18* (2), 93–115.

(10) Yezer, B. A.; Khair, A. S.; Sides, P. J.; Prieve, D. C. Use of Electrochemical Impedance Spectroscopy to Determine Double-Layer Capacitance in Doped Nonpolar Liquids. *J. Colloid Interface Sci.* **2015**, *449*, 2–12.

(11) Yezer, B. A.; Khair, A. S.; Sides, P. J.; Prieve, D. C. Determination of Charge

Carrier Concentration in Doped Nonpolar Liquids by Impedance Spectroscopy in the Presence of Charge Adsorption. *J. Colloid Interface Sci.* **2016**, *469*, 325–337.

(12) Eicke, H. F.; Borkovec, M.; Das-Gupta, B. Conductivity of Water-in-Oil Microemulsions: A Quantitative Charge Fluctuation Model. *J. Phys. Chem.* **1989**, *93* (1), 314–317.

(13) Wohlfarth, C. W. Permittivity (Dielectric Constant) of Liquids Christian Wohlfarth. *CRC Handb. Chem. Phys.* **2016**, 6-187-6–208.

(14) Endo, K.; Tatsumi, T. Fluorinated Amorphous Carbon Thin Films Grown from C4F8 for Multilevel Interconnections of Integrated Circuits. *Nec Research & Development*. 1997, pp 287–293.

(15) Yezer, B. A. Determination of Charge Concentration in Surfactant Doped Nonpolar Liquids, Carnegie Mellon University, 2016. Thesis.

(16) Kline, S. R. Reduction and Analysis of SANS and USANS Data Using IGOR Pro. *J. Appl. Crystallogr.* **2006**.

(17) Hall, D. G. Conductivity of Microemulsions: An Improved Charge Fluctuation Model. *J. Phys. Chem.* **1990**.

(18) Parent, M. E.; Yang, J.; Jeon, Y.; Toney, M. F.; Zhou, Z. L.; Henze, D. Influence of Surfactant Structure on Reverse Micelle Size and Charge for Nonpolar Electrophoretic Inks. *Langmuir* **2011**, *27* (19), 11845–11851.

(19) Michor, E. L.; Ponto, B. S.; Berg, J. C. Effects of Reverse Micellar Structure on the Particle Charging Capabilities of the Span Surfactant Series. *Langmuir* **2016**.

(20) Prieve, D. C.; Yezer, B. A.; Khair, A. S.; Sides, P. J.; Schneider, J. W. Formation of Charge Carriers in Liquids. *Adv. Colloid Interface Sci.* **2017**.

(21) Michor, E. L.; Berg, J. C. Extension to the Charge Fluctuation Model for the Prediction of the Conductivity of Apolar, Reverse Micellar Systems. *Langmuir* **2012**, *28* (45), 15751–15755.

(22) Feng, K. I.; Schelly, Z. A. Equilibrium Properties of Crystallites and Reverse Micelles of Sodium Bis(2-Ethylhexyl) Phosphate in Benzene. *J. Phys. Chem.* **1995**.

(23) Kotlarchyk, M.; Huang, J. S.; Chen, S. H. Structure of AOT Reversed Micelles Determined by Small-Angle Neutron Scattering. *J. Phys. Chem.* **1985**, *89* (20), 4382–4386.

(24) Smith, G. N.; Brown, P.; James, C.; Rogers, S. E.; Eastoe, J. The Effect of Solvent and Counterion Variation on Inverse Micelle CMCs in Hydrocarbon Solvents. *Colloids Surfaces A Physicochem. Eng. Asp.* **2016**.

(25) Thomas, H. G.; Lomakin, A.; Blankschtein, D.; Benedek, G. B. Growth of Mixed Nonionic Micelles. *Langmuir* **1997**.

Chapter 4 Dependence of surfactant doped nonpolar media conductivity on surfactant dissociability

4.1 Introduction

Surface charging of particles by surfactants in nonpolar media is of interest in a diverse range of fields such as oil recovery,[1] reflective displays,[2,3] and drug delivery.[4] Certain surfactants in nonpolar liquids are capable of charging particles through assembly into reverse micelles with water, ions, and polar head groups sequestered in an internal core and surfactant tails extended outwards to form a hydrocarbon shell.[5,6] These reverse micelles acquire charge during Brownian collisions in which a free ion is exchanged from one neutrally charged micelle to another, resulting in two oppositely charged micelles.[7] Attempts have been made to quantitatively model these collisions, termed the disproportion mechanism for charge formation, using a charge-fluctuation model first proposed by Eicke.[8–10] The charge fluctuation model is a one parameter model that predicts surfactant charging of nonpolar media based on micelle size.[8,9] While the charge fluctuation model has been shown to predict conductivity of bis-(2-ethylhexyl) sulfosuccinate (AOT) doped nonpolar solutions,[8] it cannot predict charging behavior of the $(C_8b)_2$-Asp-PTS and $(C_8b)_2$-Glu-PTS surfactants discussed in Chapter 3. Therefore, some factor beyond micelle size must be accounted for to describe the charging of $(C_8b)_2$-Asp-PTS and $(C_8b)_2$-Glu-PTS surfactants.

Ionic strength results in Chapter 3 indicated that counterion size may be the key factor in differentiating the charging of $(C_8b)_2$-Asp-PTS and $(C_8b)_2$-Glu-PTS from sodium AOT micelles. That is, larger organic counterions like para-toluene sulfonate (PTS) are more likely to be dissociated from their ionic surfactant counterpart while inside the

micelle core and during micelle collisions than small metallic ions like sodium. This increased likelihood of charge transfer during micelle collisions could be responsible for the superior charging ability of $(C_8b)_2$-Asp-PTS and $(C_8b)_2$-Glu-PTS compared to AOT micelles. Studies in literature have also explored the effect of surfactant counterion and chemical structure for AOT and AOT homologue surfactants. Eastoe[11–13] has used counterion exchange techniques to produce a palette of AOT compounds with different univalent and divalent metal counterions and concluded that metal counterion size changed the shape of assembled micelles. Similar experiments conducted for bis-(2-ethylhexyl) phosphorate (DEHP), a phosphate head group homologue of AOT, demonstrate that reverse micelle shape of DEHP is also dependent on counterion chemistry.[14] Although these micelle size and shape variations are useful for understanding self-assembly of surfactants in nonpolar media, they do not elucidate the charging properties that are vital to the viability of such surfactants for industrial applications. EIS experiments on such samples would allow direct measurement of surfactant electrical properties rather than those inferred from shape measurements using scattering techniques. Parent et al. have developed a synthetic technique to modify the head group of non-ionic surfactant polyisobutylene succinimide (PIB) by incrementally increasing the length of polyamide chains in the succinimide head.[15] Doping nonpolar media with PIBs, they measured an enhanced conductivity of the nonpolar liquid despite PIBs being non-ionic. While giving no explanation for the origin of charge, they do conclude that non-ionic surfactants with larger head groups tend to form larger micelles in solution than smaller head group counterparts, resulting in higher ionic strengths for large micelles as predicted by charge-fluctuation theory.[15] However, it

is unclear whether these conclusions can be extended more universally to both ionic and non-ionic surfactants.

In this study, we use the synthetic method developed in Chapter 3 and ion-exchange to synthesize a series of surfactants with incrementally altered head groups, counterions, and hydrocarbon tail chemistries. The conductivity and ionic strength of these surfactants are measured using EIS to reveal specific structure-function relationships key to charging of micelles in non-polar liquids. Surfactant chemistry modifications span both ionic and non-ionic surfactants. Dynamic light scattering measurements are also taken for all surfactants so as to correlate surfactant assembly with surfactant charging.

4.2 Materials and Methods

4.2.1 Materials

A variety of synthesized and commercial surfactants were investigated to determine the relationship between surfactant chemical structure and charging behavior in dodecane. Surfactants were categorized into three different groups. The first group of surfactants were selected to examine how head group chemistry impacts formation of charged micelles in nonpolar liquids. A series of surfactants with increasingly non-dissociable head groups were synthesized to accomplish this aim. The chemical structures of group 1 surfactants are shown in **Figure 4.1**.

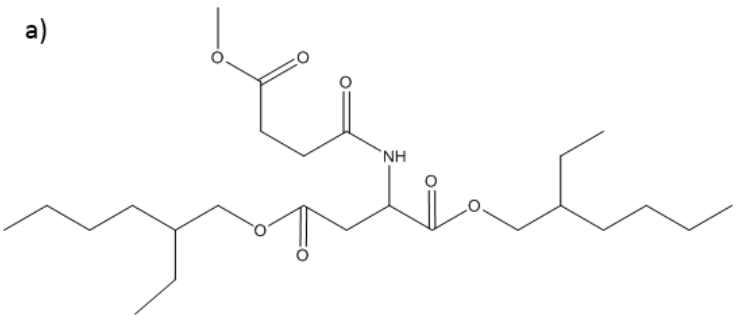

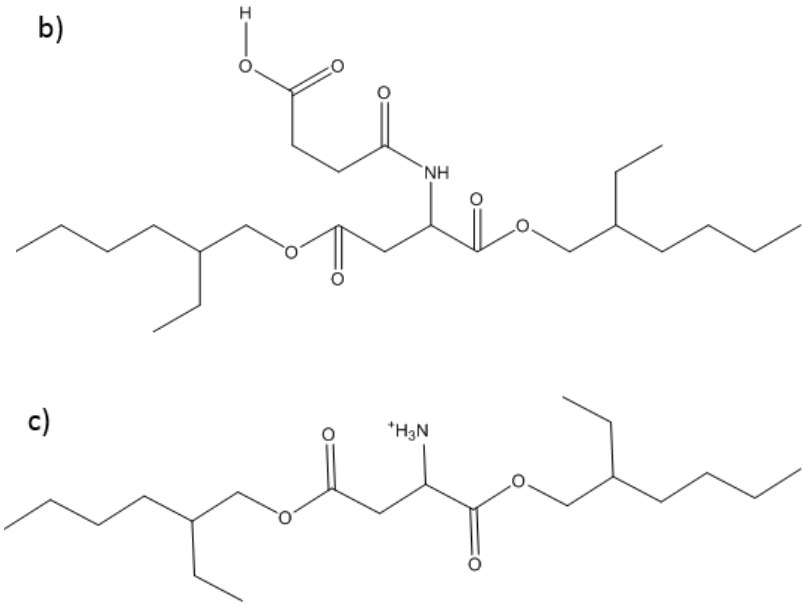

Figure 4.1. Group 1 sufactants consisting of a) $(C_8b)_2$-Asp-Methyl, b) $(C_8b)_2$-Asp-COOH, and c) $(C_8b)_2$-Asp-PTS. The three structures are shown in order of increasing dissociability.

The tail structure between the three surfactant groups were kept constant while small changes in head group chemistry were imposed. The non-ionic surfactants $(C_8b)_2$-Asp-Methyl has a completely non-dissociable head group while $(C_8b)_2$-Asp-COOH has a potentially dissociable hydrogen. Dukhin has measured conductivity of alcohols in nonpolar liquid due to proton dissociation of the hydroxyl group which could also occur for $(C_8b)_2$-Asp-COOH.[16] In contrast, $(C_8b)_2$- Asp-PTS is a true ionic surfactant with a charged polar head and a para-toluene sulfonate counterion. The next group of surfactants were chosen based on incremental changes in tail group chemistry. They are shown in **Figure 4.2**.

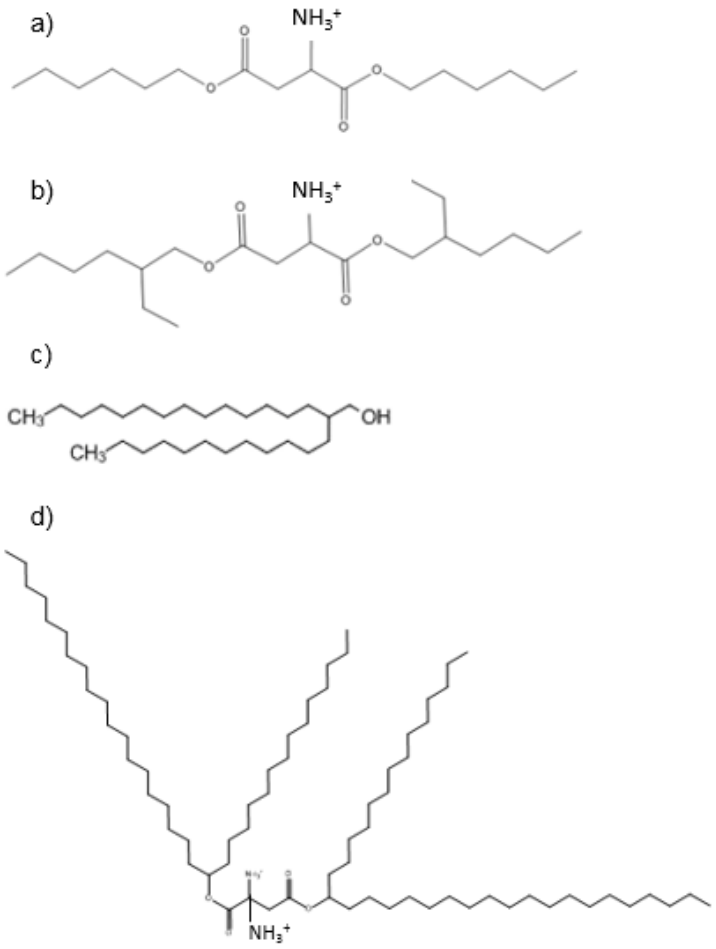

Figure 4.2. Group 2 structures a) C_6-Asp-PTS, b) $(C_8b)_2$-Asp-PTS, c) I-28, and I-34T-Asp-PTS. All surfactants with the exception of I-28 have a para-toluene sulfonate counterion.

The surfactants in **Figure 4.2** are vary in both carbon tail length as well as the degree of branching. C_6-Asp-PTS has the shortest tail with no branching while $(C_8b)_2$-Asp-PTS has a branch on the second carbon. I-28 is a long chain alcohol with 14 carbons in each tail. Although it is not a surfactant in the typical sense, the polar nature of the alcohol group coupled with the two hydrocarbon chains could act sufficiently amphiphilic in nonpolar liquids.[16] Finally, I-34T-Asp-PTS shares the same amino polar head group as C_6-Asp-PTS and $(C_8b)_2$-Asp-PTS but possesses a bulky 17 carbon alkyl tail. The last group of surfactants are shown in **Figure 4.3**.

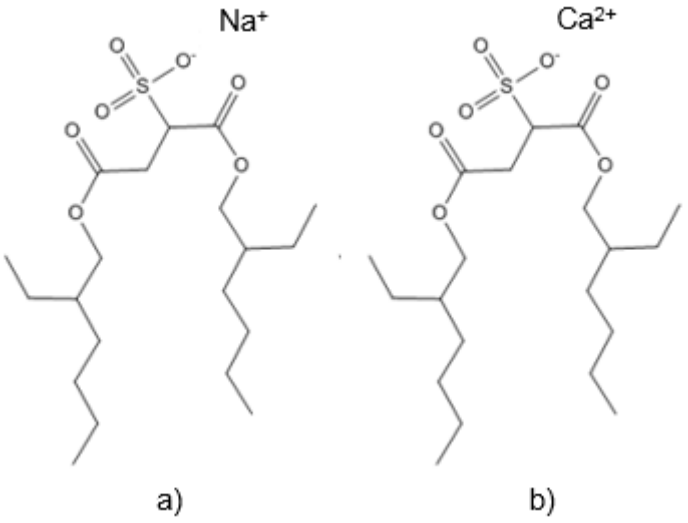

Figure 4.3. Group 3 structures a) sodium (Na) AOT and b) calcium (Ca) AOT. Note that there are two surfactant per calcium due to its divalent charge.

The two AOT surfactants shown in **Figure 4.3** were chosen to isolate the effect of counterion charge on micelle formation and charging in nonpolar liquids. Na AOT and Ca AOT are identical ionic surfactants that differ only in counterion identity. Na AOT is a univalent surfactant while Ca AOT is a divalent surfactant.

The majority of the surfactants were synthesized through esterification reactions of two long chain alcohols (Sigma-Aldritch) by aspartic acid (Sigma-Aldrich). The reactions are catalyzed by *para*-toluene sulfonate (Sigma-Aldrich) which remained in the ionic surfactant products as the counterion. The synthesis reaction was carried out under reflux in toluene for 4 hours so as to remove the undesirable side product water. A list of long chain alcohols and amino acid linkers used for each synthesized surfactant is shown in **Table 4.1**. $(C_8b)_2$-Asp-Methyl and $(C_8b)_2$-Asp-COOH required additional reaction steps beyond the esterification reaction to generate the final product structure. $(C_8b)_2$-Asp-COOH was synthesized from acylation of $(C_8b)_2$-Asp-PTS with succinic anhydride in the presence of excess trimethylamine. $(C_8b)_2$-Asp-Methyl was synthesized

from acylation of $(C_8b)_2$-Asp-PTS with monomethyl succinate in a solvent consisting of dichloromethane and dimethylformamide with N,N-diisopropylethylamine and 2-hydroxybenzothiazole acting as catalysts. Details regarding both reactions are further discussed by Haverstick.[17]

Table 4.1. Alcohol tail used in synthesis of each surfactant.

Surfactant	Alcohol Tail
C_6-Asp-PTS	hexanol
$(C_8b)_2$-Asp-PTS	2-ethyl-1hexanol
$(C_8b)_2$-Asp-COOH	2-ethyl-1hexanol
$(I\text{-}34T)_2$-Asp-PTS	I-34T

Ca AOT was produced from a liquid-liquid ion-exchange method described by Eastoe.[12] In this technique, equal volumes of a Na AOT in heptane solution and aqueous CaCl (Sigma-Aldrich) were prepared at a concentration of 1 M and 100 mM respectively. Next, the aqueous and nonpolar solutions were shaken together in a flask, forming a Winsor II emulsion.[12] Over a period of 1-3 days, the emulsion would settle into two distinct phases – an oil rich phase and a water rich phase. The organic phase was then carefully siphoned off and shaken with fresh aqueous solution two further times. Upon completion, the organic solvent was removed using rotary evaporation (Buchi) for one day.

All product surfactants were purified using flash column chromatography (Combiflash) in a silica gel column and subsequently placed in a rotary evaporator for 5 hours. Molecular weights of products were validated via electrospray ionization spectroscopy (Thermo Scientific LTQ-XL Linear Ion Trap Mass Spectrometer). Surfactants were stored in a lyophilizer for one week prior to experiments to allow

evaporation of volatile impurities.

4.2.2 Methods

The impedance cell consists of a pair electrodes made of ITO coated glass slides overlaid on top of each other with sample fluid is injected between the slides as seen in **Figure 2.3**. The two electrodes are held apart at a uniform distance by 8 μm silica spacer beads (Co-spheric LLC). The ITO coating of the electrode slides are further coated with a 33 nm thickness layer of fluoropolymer to prevent undesirable charge adsorption during the impedance experiment. Details of the procedure for assembly of the impedance cell and manufacture of the fluoropolymer coating are rigorously described in Chapter 2.[18,19] Next, the impedance cell is connected to a VersaSTAT 3 potentiostat (Princeton Applied Instruments) equipped with a low current Interface. All impedance cells are assembled in a nitrogen-blanked glove bag, and impedance experiments take place in a nitrogen blanketed Faraday cage.

Analysis of the impedance data is intensively described in Chapters 2 and 3. For brevity, the analysis method can be summarized as deriving the value of impedance elements C_g, R_f, and C_{dl} which are in turn used to infer the physical parameters of the sample solution K (conductivity), I (ionic strength), and D_h (hydrodynamic diameter). The parameters C_g, C_{dl},, and R_f are related to the fluid electrical properties by the following equations.

$$R_f = \frac{d}{A_f K} \tag{4.1}$$

$$C_g = \frac{\varepsilon_f A_f}{d} \tag{4.2}$$

$$C_{dl} = \frac{\varepsilon_f}{\lambda_D} \cosh\left(\frac{e\zeta}{2k_B T}\right) \tag{4.3}$$

where *d* is the gap distance between the electrodes, A_f is the area of the solution held between the two electrodes, *K* is the conductivity of the solution, and ζ is the zeta potential of the electrode surface. The ionic strength of the bulk fluid can then be calculated from equation (3.5).

$$\lambda_D = \sqrt{\frac{\varepsilon_f k_B T}{2e^2 n_0}} \tag{4.4}$$

Where ε_f is the permittivity of the solution, k_B is Boltzmann's constant, *T* is absolute temperature, *e* is the charge on one proton, and n_0 is the ionic strength (number per volume). The hydrodynamic radius of charge carriers can be calculated from the conductivity and ionic strength of the sample and the Stokes-Einstein equation. C_g, C_{dl}, and R_f, are obtained from the ratio of the extrema of *Im(Z)* according to equation (3.7) of Chapter 3.

In order to calculate the number of charge carriers in solution from the impedance spectra, Zetaspin™ was used to determine the zeta potential of the fluoropolymer coated ITO slides. Zetaspin™ involves measurement of the streaming potential between two inert, glassy carbon electrodes immersed in surfactant solution. The software (LabVIEW, National Instruments) then calculates the zeta potential of the electrode surface from the measured streaming potential.[20] The sample preparation and procedure for these Zetaspin™ experiments were as described by the previous work.[20] All solutions were maintained at a water content below 10 ppm according to a coulometric Karl-Fisher water titrator.

To compare the EIS-derived charge-carrier sizes to the hydrodynamic micelle size, dynamic light scattering measurements were performed on the surfactant solutions. A Malvern ZetaSizer Nano ZSP (Malvern Instruments, Malvern, UK) used phase analysis light scattering (PALS) to correlate temporal scattering fluctuations to hydrodynamic size information. All solutions were sparged with nitrogen and prepared in a nitrogen glove bag to keep the water content below the detectability limit at all times. Both solvent and solution were filtered prior to light scattering using a 250 nm polytetrafluoroethylene syringe filter (VWR International).

4.3 Results and Discussion

4.3.1 Solubility

All surfactants in Groups 3 were found to be soluble in dodecane. Group 1 surfactants $(C_8b)_2$-Asp-COOH and $(C_8b)_2$-Asp-PTS dissolved spontaneously in dodecane without agitation while $(C_8b)_2$-Asp-Methyl was completely insoluble after sonication and three days of equilibration. Solubility was judged based on optical clarity of the surfactant solutions and absence of sedimented aggregates. All surfactants with ionic or alcohol head groups were soluble in dodecane while the surfactant with the most nonpolar head group $(C_8b)_2$-Asp-Methyl was not. Clearly then, the self-assembly behavior of the synthesized surfactants is determined by their head group chemistry and some degree of head group polarity is essential to solubility in nonpolar solvents. Amongst the group 2 surfactants, C_6-Asp-PTS was the only sample that was insoluble in surfactant. Despite being an ionic surfactant, the lack of branching points within the surfactant structure may have prevented assembly into micelles in solvent. One rationale for this behavior is that non-branched surfactants lack curvature, making

aggregation into non-monolayer structures difficult. Such trends were seen in a systematic study of AOT-like surfactants studied by Eastoe.[11]

4.3.2. Conductivity

Of the six dodecane soluble surfactants, only four had measurable conductivities (>10 pS/cm) in dodecane. For Group 1 surfactants, all candidates were conductive in dodecane with the exception of C_6-Asp-PTS as it was insoluble in dodecane. Group 2 surfactants showed the most diverse conductivity behavior. Despite being soluble in dodecane, I-28 and $(I\text{-}34T)_2$-Asp-PTS showed no conductivity enhancing behavior. This could arise if surfactants do not form micelles and exist merely as monomer surfactants in solution. Without the ability to solvate charge in a polar micelle interior, the surfactants cannot act as vehicles for charging. Dye studies on I-28 in dodecane solutions indicate that this is a likely possibility. When 20 mL vials of I-28 solutions were doped with 0.5 mg of bromothymol red, a water soluble pH indicator, no significant solvation of dye was observed according to UV-Vis measurements. Without formation of I-28 micelles, there was no suitably polar environment for solvation of dye particles. Amongst the Group 2 surfactants, I-28 has the least polar head group. Consequently, there may not be sufficient amphiphilic character in the chemical structure of I-28 to form micelles. Such an explanation is further bolstered by experiments from the literature. Dukhin[16] observed that octanol raised the conductivity of poly-α-olefin at alcohol concentrations above 20 weight percent. He hypothesized that octanol formed micellar structures in poly-α-olefin, and that these octanol micelles raised the conductivity of the olefin by solvating charge in their interiors.[16] Examining the structure of I-28 and octanol, one notes the large difference in hydrophile to lyophile balance

between the two. I-28 has a 28 carbon backbone forming its tail structure while octanol has only 8 carbons in its backbone. I-28 is less amphiphilic and therefore predominately nonpolar compared to its octanol counterpart. Dukhin's observations thus add credibility to the conclusion that I-28 is not sufficiently amphiphilic to form micelles that solvate charge in nonpolar liquids. $(I\text{-}34T)_2$-Asp-PTS was also non-conductive in dodecane. Comparing the hydrophile to lyophile balance amongst Group 2 surfactants, $(I\text{-}34T)_2$-Asp-PTS distinguishes itself as the surfactant with the most lyophiles as it possesses the most numerous and longest hydrocarbon tails. Beyond the decrease in amphiphilic character that results from its predominately lyophilic nature, the steric challenge of four long hydrocarbon tails may prevent aggregation of $(I\text{-}34T)_2$-Asp-PTS into charged micelles.

Conductivity of the remaining surfactant solutions were derived from EIS impedance spectra. This was accomplish through using the equivalent circuit described in Chapters 2 and 3 to calculate the impedance element R_f. Afterwards, R_f is used to derive the fluid conductivity K according to equation (3.2) and is subsequently plotted in **Figure 4.4**.

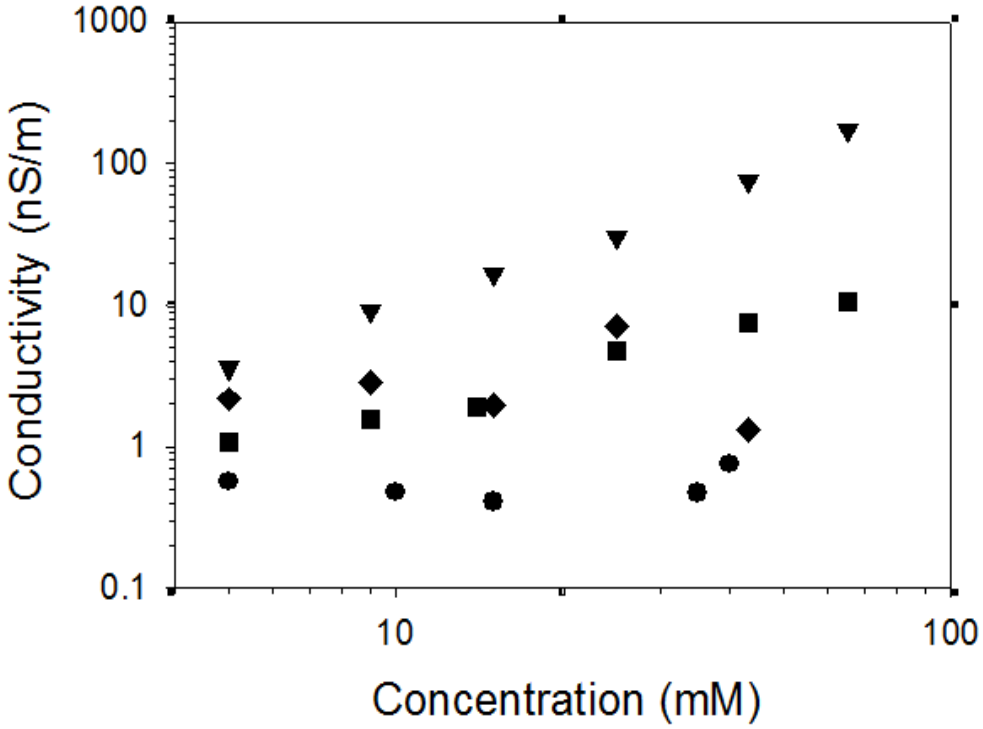

Figure 4.4. Plot of conductivity as a function of surfactant concentration for sodium AOT (filled squares), calcium AOT (filled diamonds), $(C_8b)_2$-Asp-PTS (filled triangles), and $(C_8b)_2$-Asp-COOH (filled circles).

Of the surfactant candidates included in this study, only $(C_8b)_2$-Asp-PTS, $(C_8b)_2$-Asp-COOH, calcium AOT, and sodium AOT were measurably conductive. Their EIS derived conductivities are shown in **Figure 4.4** as a function of surfactant concentration. Evaluating differences in conductivity between surfactants of Group 2, one observes that $(C_8b)_2$-Asp-PTS is between one and two orders of magnitude more conductive than $(C_8b)_2$-Asp-COOH. Furthermore, $(C_8b)_2$-Asp-PTS displays linear increases in conductivity as a function of surfactant concentration. In contrast, the conductivity of $(C_8b)_2$-Asp-COOH is relatively consistent at 0.5 nS/m at all surfactant concentrations. Differences in charging of $(C_8b)_2$-Asp-PTS micelles relative to $(C_8b)_2$-Asp-COOH micelles can be rationalized in terms of head group dissociability. Prior experiments described in Chapter 3 of this thesis has shown that $(C_8b)_2$-Asp-PTS are more likely to

form charged micelles in solution than sodium AOT. Given that surfactant structures are almost identical between the two surfactants, this difference in micelle charging can be attributed to the surfactant counterion. That is, the small sodium counterions were less likely to dissociate and form free charges that could be solvated in micelle interiors than the bulkier para-toluene sulfonate counterions. Following that reasoning, the covalently bonded proton in the carboxyl group of $(C_8b)_2$-Asp-COOH is less likely to dissociate than the ionic bound para-toluene sulfonate counterion of $(C_8b)_2$-Asp-PTS. In a polar environment such as a micelle interior, salts are far more likely to dissociate than nonionic covalently bonded species. Through head group modification, we have successfully changed the surfactant dissociability and hence charging behavior of $(C_8b)_2$-Asp-PTS to resemble that of sodium AOT. **Figure 4.4** also contains the conductivity behavior of sodium AOT and calcium AOT. In contrast to the two Asp-PTS surfactants, calcium AOT and sodium AOT have similar conductivities. Given that calcium is a divalent ion of similar size to sodium, it is reasonable that the dissociability and hence the conductivity of the two AOT surfactants are comparable.

4.3.3 Ionic Strength

The ionic strength of the surfactant solutions were derived from C_{dl} interpreted from the impedance spectra and λ_D using equations (4.3) and (4.4). Ionic strengths for all four conductive surfactants are plotted in **Figure 4.5**.

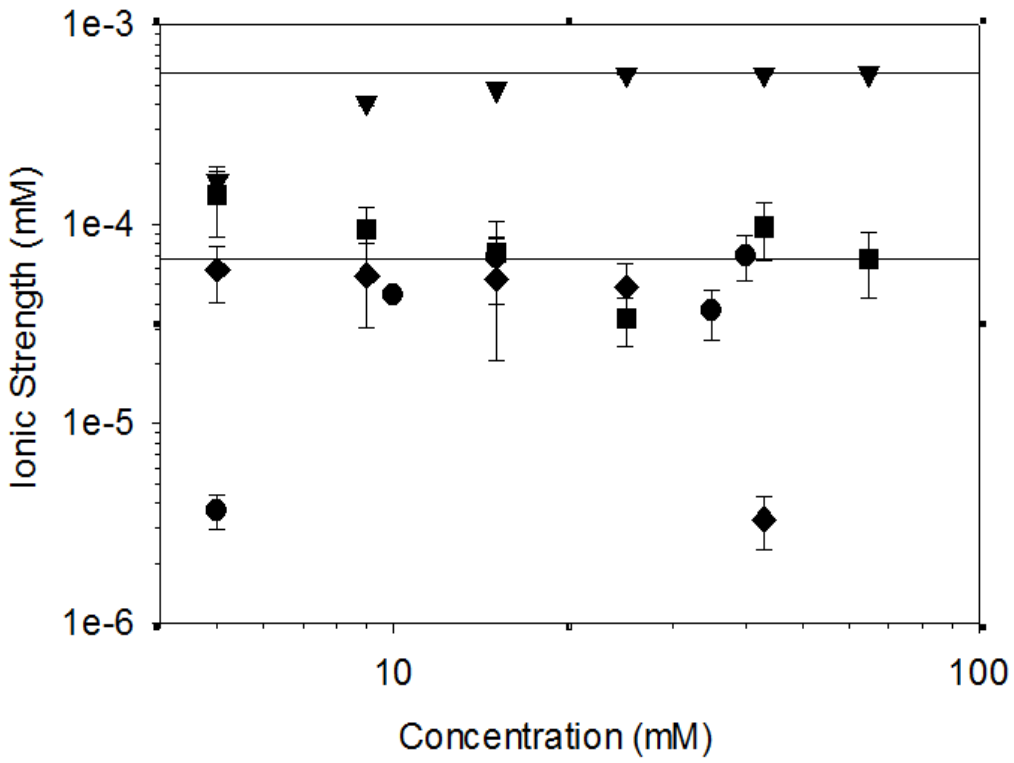

Figure 4.5. Ionic strength as a function of surfactant concentration for sodium AOT (filled squares), calcium AOT (filled diamonds), $(C_8b)_2$-Asp-PTS (filled triangles), and $(C_8b)_2$-Asp-COOH (filled circles). Top line is the average ionic strength of $(C_8b)_2$-Asp-PTS while bottom line is the average ionic strength of sodium AOT, calcium AOT and $(C_8b)_2$-Asp-COOH excluding the two outliers at 3 x 10^6 mM.

The ionic strengths in **Figure 4.5** are all relatively constant as a function of surfactant concentration. This behavior is in accordance with ionic strength trends seen in Chapter 3. The extremely low water content of surfactant solutions may limit the number of solvated ions in the micelle core. Even as the concentration of surfactant and hence micelles available for Brownian collisions increase, there is no additional dissociated ions in the polar core available for micelle to micelle transfer. The ionic strengths of calcium AOT, sodium AOT, and $(C_8b)_2$-Asp-COOH are similar at all surfactant concentrations. The average ionic strength of the three surfactants is 7 ± 3 x 10^5 mM when excluding the two outliers at 3 x 10^6 mM. $(C_8b)_2$-Asp-PTS has an average ionic strength of 6 ± 1 x 10^{-4} mM which is an order of magnitude larger than the other

three surfactants. Overall, **Figure 4.5** demonstrates that small changes in surfactant chemistry has strong effects on the number of charged micelles in solution. These effects can largely be understood as a result of head group chemistry and surfactant dissociability. For example, a bulk organic counterion such as para-toluene sulfonate is ten times more likely to be a free ion within the micelle core and be exchanged during a Brownian collision than small, high charge density counterions like sodium or calcium. Of particular interest is that although we expect sodium AOT, calcium AOT, and $(C_8b)_2$-Asp-COOH to have lower ionic strengths than $(C_8b)_2$-Asp-PTS due to surfactant dissociability, there is no clear reason why the ionic strengths of the three surfactants are largely the same. Given that the variation in surfactant chemistry represented by these three surfactants include ionic versus covalent bonds, univalent versus divalent counterions, it is intriguing that the ionic strength is surprisingly insensitive.

4.3.4 Hydrodynamic Diameter

Hydrodynamic diameters of charged micelles were calculated from the Stokes-Einstein equation presented as equation (3.6) in Chapter 3. Micelle sizes for the entire population, both charged and uncharged, were obtained from dynamic light scattering experiments. Comparisons of the charged micelle diameter and the total micelle diameter are shown in **Figure 4.6**.

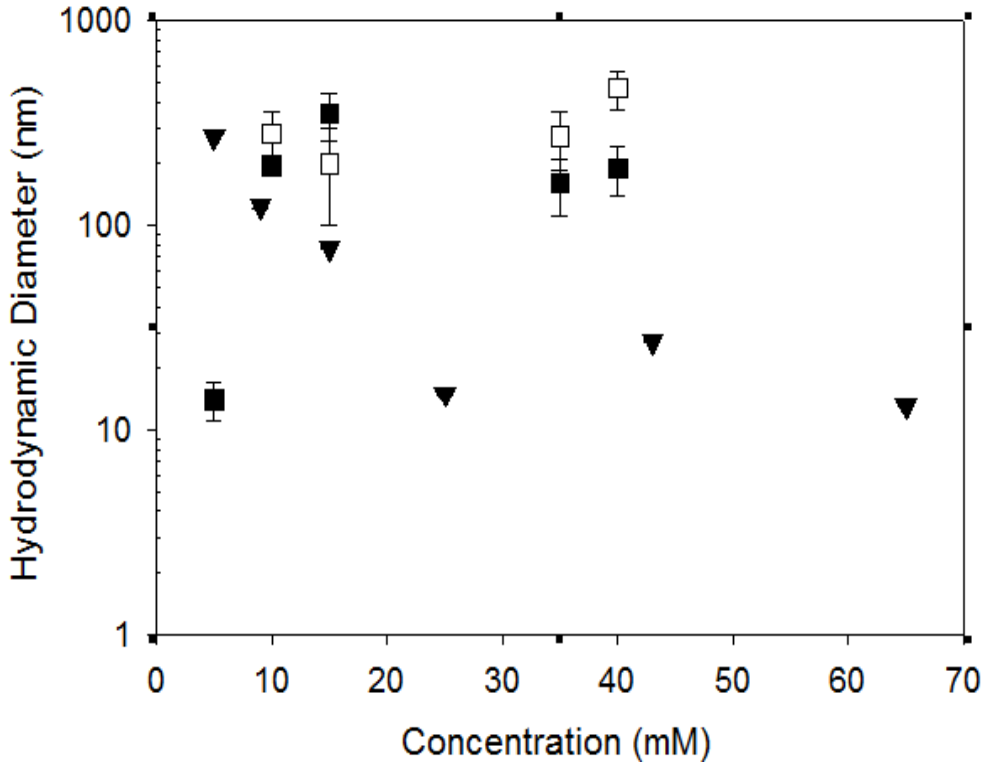

Figure 4.6. The hydrodynamic diameter of charged micelles obtained from EIS for $(C_8b)_2$-Asp-PTS (filled triangles), and $(C_8b)_2$-Asp-COOH (filled squares). Hydrodynamic diameter of entire micelle population, charged and uncharged, obtained from DLS for $(C_8b)_2$-Asp-COOH are shown as open squares.

From **Figure 4.6**, the size of the entire population of micelles obtained from DLS is about the same as the size of the charged micelles obtained from EIS. That is, hydrodynamic diameters from both EIS and DLS are within three standard deviations of each other. Overall, the similarity in size between the two measurements verifies EIS as a reliable method of obtaining size of charge carriers. The biggest difference amongst the three plots shown in **Figure 4.6** is that the micelles of $(C_8b)_2$-Asp-COOH are much larger than micelles of $(C_8b)_2$-Asp-PTS. According to the charge fluctuation theory of micelle charging, larger micelles are more likely to become charged than smaller micelles because larger micelles require less energy to charge. The data in **Figure 4.6** directly contradicts such charging predictions from the charge fluctuation theory.

Although $(C_8b)_2$-Asp-COOH forms micelles that are an order of magnitude larger than $(C_8b)_2$-Asp-PTS, it has an order of magnitude lower ionic strength than its PTS counterpart. Examining the chemical structures of the two surfactants, this discrepancy in charging behavior can be attributed to the difference in head group chemistry between the two surfactants. As discussed when rationalizing ionic strength trends amongst the studied surfactants, the carboxyl head group structure of $(C_8b)_2$-Asp-COOH is far less dissociable than the PTS counterion of $(C_8b)_2$-Asp-PTS. As a result, solutions of $(C_8b)_2$-Asp-PTS may have a bigger reservoir of micelles with a dissociated charge in the polar interior than those of $(C_8b)_2$-Asp-COOH. These dissociated charges in the micelle interior are ultimately the limiting factor in determining the extent of charging possible in a given micelle solution.

Similar size information for micelles of sodium and calcium AOT are shown in **Figure 4.7**.

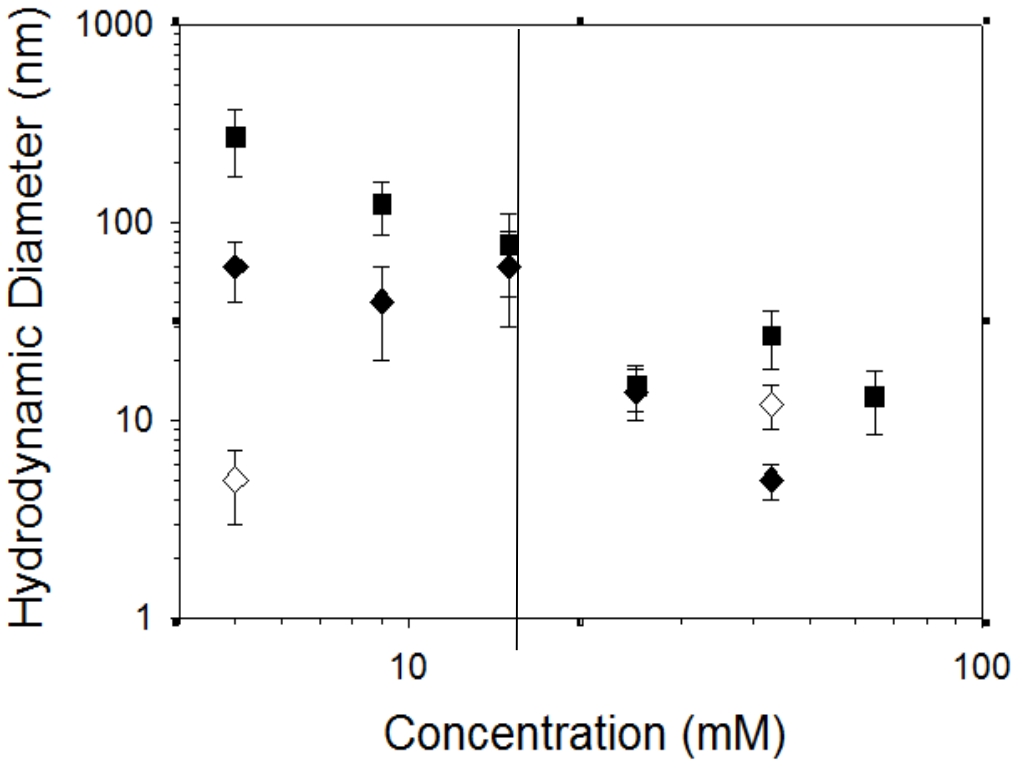

Figure 4.7. Hydrodynamic diameter of charged micelles obtained from EIS for sodium AOT (filled squares) and calcium AOT (filled diamonds). DLS derived diameters for all micelles of calcium AOT is shown as open diamonds.

The size of charged micelles for sodium AOT and calcium AOT from data presented in **Figure 4.7**. As discussed in Chapter 3, the micelle population of sodium AOT undergo a bimodal to unimodal transition at a surfactant concentration of approximately 20 mM. Below 20 mM, the charged species consist of the larger of the two micelle populations; above 20 mM, this larger micelle population disappears. As a result, the charged micelle population abruptly decreases in size above a surfactant concentration of 20 mM. For micelles of calcium AOT, there is no sharp transition from a bimodal to unimodal micelle population. As evident in the dynamic light scattering data of calcium AOT, there is only a single size population of micelles which grow slightly larger in size with surfactant concentration. Similarly, the charged micelles of calcium

AOT do not abruptly change size with surfactant concentration. Overall, while the ionic strengths of calcium AOT and sodium AOT are similar, the self-assembly behavior of the two surfactants are very different. The disparate self-assembly mechanisms are likely responsible for the distinct conductivity trends of each surfactant.

4.4 Conclusions

Previous studies in the literature have studied homologues of commercial surfactants to elucidate how surfactant chemistry impacts micelle charging in nonpolar media. Many of these studies focus on scattering techniques to characterize micelles; however, only about one in one million micelles are charged. Thus, scattering studies are biased towards the non-charged micelles and interpretation of the charged micelle behavior from scattering is often inaccurate. In contrast, studies that involve electrical measurements are often limited in surfactant scope. That is, they are focused exclusively on either ionic or nonionic surfactants, and the surfactant homologue structures are limited to close variations of existing commercial surfactants. In this study, we use synthesis and ion exchange techniques to produce high purity surfactants with incremental variations in surfactant head group, counterion, and tail structure.

Impedance-spectroscopy-derived conductivities and ionic strengths for the surfactants revealed a strong relationship between surfactant dissociability and surfactant charging. For a series of $(C_8b)_2$- Asp surfactants, an increase in surfactant dissociability through incremental modification of the polar head group was correlated with increased solvent solubility and ionic strength. This trend was observed in both ionic and non-ionic surfactants. Ionic surfactants with bulkier organic counterions had larger ionic strengths than metallic counterion surfactants. Non-ionic surfactants with

carboxyl terminated head groups were more conductive than those with methyl terminated head groups. Surfactant tail modifications revealed that some degree of branching was necessary for surfactant solubility in nonpolar liquids; however, there was no straightforward relationship between tail chemistry and ionic strength. While longer tails did result in soluble surfactants, the majority of tail modified surfactants were not conductive in dodecane. This is because while longer tails increased the nonpolar nature of surfactants allowing for easier dissolution in dodecane, the steric hindrance imposed by increasingly bulkier and longer surfactant tails prevented self-assembly into reverse micelles.

4.5 Acknowledgements

We thank Norman Gottron and Mason Risley at the Carnegie Mellon Nanofabrication Facility for the plasma deposition expertise and manufacturing of the C_4F_8 coating. Thanks to Bugra Ozutemiz and Dr. Burak Ozdoganlar at the mechanical engineering department at Carnegie Mellon for access and training on the white light interferometer. Another thank you to undergraduate researcher Eileen Kim for helping with synthesis of the AOT analogs. We also gratefully acknowledge financial support through NSF grant #1511619.

4.6 References

(1) Nikakhtari, H.; Vagi, L; Choi, P.; Liu, Q.; Gray, M. R.; Univ, A. Solent Screening For Non-Aqueous Extraction of Alberta Oil Sands. *Can. J. Chem. Eng.* **2013**, *91* (6), 1153–1160.

(2) Chen, Y.; Au, J.; Kazlas, P.; Ritenour, a; Gates, H.; McCreary, M. Electronic Paper: Flexible Active-Matrix Electronic Ink Display. *Nature* **2003**, *423* (6936), 136.

(3) Comiskey, B.; Albert, J. D.; Yoshizawa, H.; Jacobson, J. An Electrophoretic Ink for All-Printed Reflective Electronic Displays. *Nature* **1998**, *394* (6690), 253–255.

(4) Jones, S. A.; Martin, G. P.; Brown, M. B. Manipulation of Beclomethasone-Hydrofluoroalkane Interactions Using Biocompatible Macromolecules. *J. Pharm. Sci.* **2006**, *95* (5), 1060–1074.

(5) Morrison, I. D. Electrical Charges in Nonaqueous Media. *Colloids and Surfaces A: Physicochemical and Engineering Aspects*. 1993, pp 1–37.

(6) Smith, G. N.; Eastoe, J. Controlling Colloid Charge in Nonpolar Liquids with Surfactants. *Phys. Chem. Chem. Phys.* **2012**, 424–439.

(7) Morrison, I. D. Electrical Charges in Nonaqueous Media. *Colloids Surfaces A Physicochem. Eng. Asp.* **1993**, *71* (1), 1–37.

(8) Eicke, H. F.; Borkovec, M.; Das-Gupta, B. Conductivity of Water-in-Oil Microemulsions: A Quantitative Charge Fluctuation Model. *J. Phys. Chem.* **1989**, *93* (1), 314–317.

(9) Hall, D. G. Conductivity of Microemulsions: An Improved Charge Fluctuation Model. *J. Phys. Chem.* **1990**.

(10) Michor, E. L.; Berg, J. C. Extension to the Charge Fluctuation Model for the Prediction of the Conductivity of Apolar, Reverse Micellar Systems. *Langmuir* **2012**, *28* (45), 15751–15755.

(11) Nave, S.; Eastoe, J.; Heenan, R. K.; Steytler, D.; Grillo, I. What Is so Special about Aerosol-OT? 2. Microemulsion Systems. *Langmuir* **2000**, *16* (23), 8741–8748.

(12) Eastoe, J.; Towey, T. F.; Robinson, B. H.; Williams, J.; Heenan, R. K. Structures of Metal Bis(2-Ethylhexyl) Sulfosuccinate Aggregates in Cyclohexane. *J. Phys. Chem.* **1993**, *97*, 1459–1463.

(13) Smith, G. N.; Brown, P.; James, C.; Kemp, R.; Khan, A. M.; Plivelic, T. S.; Rogers, S. E.; Eastoe, J. The Effects of Counterion Exchange on Charge Stabilization for Anionic Surfactants in Nonpolar Solvents. *J. Colloid Interface Sci.* **2016**, *465*.

(14) Steytler, D. C.; Jenta, T. R.; Robinson, B. H.; Eastoe, J.; Heenan, R. K. Structure of Reversed Micelles Formed by Metal Salts of Bis(Ethylhexyl) Phosphoric Acid. *Langmuir* **1996**.

(15) Parent, M. E.; Yang, J.; Jeon, Y.; Toney, M. F.; Zhou, Z. L.; Henze, D. Influence of Surfactant Structure on Reverse Micelle Size and Charge for Nonpolar Electrophoretic Inks. *Langmuir* **2011**, *27* (19), 11845–11851.

(16) Bombard, A. J. F.; Dukhin, A. Ionization of a Nonpolar Liquid with an Alcohol. *Langmuir* **2014**, *30* (15), 4517–4521.

(17) Haverstick, K. Fundamental Behavior of a Model Biomolecular Amphiphile System, University of Minnesota, 1999. Thesis

(18) Yezer, B. A.; Khair, A. S.; Sides, P. J.; Prieve, D. C. Determination of Charge Carrier Concentration in Doped Nonpolar Liquids by Impedance Spectroscopy in

the Presence of Charge Adsorption. *J. Colloid Interface Sci.* **2016**, *469*, 325–337.

(19) Yezer, B. A.; Khair, A. S.; Sides, P. J.; Prieve, D. C. Use of Electrochemical Impedance Spectroscopy to Determine Double-Layer Capacitance in Doped Nonpolar Liquids. *J. Colloid Interface Sci.* **2015**, *449*, 2–12.

(20) Yezer, B. A. Determination of Charge Concentration in Surfactant Doped Nonpolar Liquids, Carnegie Mellon University, 2016. Thesis.

Chapter 5 Zetapotential of AOT and AOT analog surfactant doped nonpolar liquids on fluoropolymer and mica

5.1 Introduction

Colloidal particles in nonpolar liquids are used in electrophoretic displays,[1,2] oil-based printing toners,[3] electrorheological fluids,[4] and drug formulations.[5] Despite our understanding of surface charging in aqueous conditions, similar mechanisms in nonpolar liquids remain abstruse. One method of characterizing surface charge is the zeta potential which measures the voltage drop across the diffuse layer of counterions next to a charged surface. Surfactants in nonpolar liquids have been known to facilitate surface charging; however, the identity of adsorbed charged species are unclear.[6,7] Ionic surfactant monomer and counterion are thought to be preferentially adsorbed onto the surface leading to surface charging. However, nonionic surfactants have also been observed charging surfaces in nonpolar liquids despite the lack of dissociable ions.[8,9] Furthermore, not only are the identity of adsorbed charges varied and highly surfactant specific, the sign of surface charging is difficult to predict and rationalize. For example, the same surfactant may induce opposite signs of surface charging depending on the surface.[10] Due to the specific nature of surfactant – surface interactions, a popular mechanism to rationalize the zeta potential is the acid-base mechanism first introduced by Fowkes.[11] Such analyses have yielded mixed results perhaps due to the presence of charged impurities in commercial surfactants as well as the role of contaminant water (from ambient air) during zeta potential measurements.[8,10,12]

Zetaspin^{TM} has been used to measure the zeta potential of surfaces in surfactant doped dodecane in prior literature.[13] This experimental technique consists of a central

spindle holding the sample surface immersed and rotated in a 400 mL reservoir of surfactant solution. The resulting streaming potential of the charged surface is measured between two inert glassy-carbon electrodes which can be used to derive the zeta potential given some solution properties.[13] The advantages of the Zetaspin™ are that a nitrogen sparger can be used in-situ to dewater the surfactant solution prior to measurements and that the measured zeta potential is not electric-field dependent.[13] The synthesis method outlined in Chapters 3 and 4 produces high purity surfactant that are ideal candidates for Zetaspin™. The surfactants are synthesized to isolate small difference in chemical structures such as variations in counterion charge and surfactant dissociability. Another motivation for Zetaspin™ studies is that impedance spectroscopy experiments described in Chapter 2-4 require zeta potential values in order to obtain correct values of ionic strengths measured by the potentiostat.[14] The Zetaspin™ is particularly suitable for this measurement because the sample must be a planar solid, just as the electrodes in EIS. Zeta potential of the electrode surface must be accounted for when inferring Debye length from the double layer capacitance. The Debye length is then used to infer the solution ionic strength.

Using the Zetaspin™, the zeta potential of mica and fluoropolymer in dodecane solutions of sodium AOT, calcium, AOT, $(C_8b)_2$-Asp-PTS, $(C_8b)_2$-Glu-PTS, and $(C_8b)_2$-Asp-COOH were measured. The chemical structures for these surfactants can be found in **Figure 3.1** for aspartic acid derived surfactants and **Figure 4.3** for AOT surfactants. These surfactants were rigorously purified and dewatered using nitrogen sparging, rotary evaporation (Buchi), and flash chromatography (Combiflash). The combination of ionic and nonionic surfactants span across a range of counterion sizes and

conductivities. Water from sample exposure to ambient air as well as contact time between surface and solution was also measured and determined to greatly change the zeta potential depending on surface. Finally, acid-base mechanisms from polymer-surface adhesion theory was applied to the experimental results in order to rationalize the zeta potential results.

5.2 Materials and Methods

5.2.1 Materials

Four noncommercial surfactants and sodium AOT (Sigma-Aldrich) were studied in this chapter. Synthesized surfactants consisted of $(C_8b)_2$-asp-PTS, $(C_8b)_2$-glu-PTS, and $(C_8b)_2$-asp-COOH. These surfactants were synthesized through esterification of two 2-ethyl-1hexanol with glutamic and aspartic acid respectively.[15] The reactions are catalyzed by para-toluene sulfonate which remained in the $(C_8b)_2$-asp-PTS and $(C_8b)_2$-glu-PTS products as counterions. An additional step was necessary for synthesis of the $(C_8b)_2$-asp-COOH. $(C_8b)_2$-asp-PTS was acylated with succinic anhydride in the presence of excess trimethylamine to synthesize $(C_8b)_2$-asp-COOH. The last surfactant tested was the calcium salt of AOT which was achieved via ion-exchange in the method described by Eastoe as described in Chapter 4.[16] Equal volumes of sodium AOT in heptane and CaCl in water were shaken together in a flask and allowed to come to equilibrium. Once the flask had settled into two distinct phases, the top heptane phase was siphoned off and shaken with fresh CaCl aqueous solutions two more times. Afterwards, the organic phase was put in a rotary evaporator (Buchi) to recover the calcium AOT from solution.

All surfactants including commercial sodium AOT were purified using flash

column chromatography (Combiflash) in a silica gel column with a solvent consisting of dichloromethane and methanol in a 9:1 ratio. After purification, surfactants were put in a rotary evaporator for five hours. Molecular weights of surfactants were confirmed through electrospray ionization spectroscopy (Thermo Scientific LTQ-XL Linear Ion Trap Mass Spectrometer). The surfactant peak for $(C_8b)_2$-asp-PTS in positive mode was m/z = 358.29 (expected: 358.30 g/mol) and in negative mode m/z=171.01 g/mol (expected 171.19 g/mol). Similarly, peaks for $(C_8b)_2$-glu-PTS positive mode was m/z=372.31 (expected: 372.31 g/mol) and negative mode m/z= 171.01 g/mol (expected 171.19 g/mol). Finally, for calcium AOT and sodium AOT, the negative mode was m/z=421.23 and m/z = 421.33 respectively (expected 421.57 g/mol). Ions in positive mode could not be discerned for calcium and sodium AOT due to the extremely small m/z value of the sodium and calcium ions. Peaks for those two surfactants in positive mode consisted of noise and contaminant peaks from previous samples.

5.2.2 Methods

Zetapotential of surfactants were determined using Zetaspin™. This apparatus measures the streaming potential between two inert, glassy carbon electrodes immersed in surfactant solution. The software (LabVIEW, National Instruments) then calculates the zeta potential of the electrode surface from the measured streaming potential. The sample preparation and procedure for these Zetaspin™ experiments were as described by Chapters 2 and 3. In order to measure zetapotential, 400 mL of surfactant solution was prepared and poured into the Zetaspin™ liquid reservoir. Next, a circular ITO slide, coated with a 33 nm fluoropolymer coating, was mounted onto a central spindle using a concentrated sugar syrup as the adhesive. The thickness of the

fluoropolymer coating was measured using white light interferometry as described in Chapter 2. The fluoropolymer layer was deposited in a plasma polymerization process using a C_4F_8 precursor in a STS Multiplex DRIE ICP system. The fluoropolymer surface is then contacted with the surfactant solution reservoir, and a motor rotated the spindle at a rate of 2000 rpm for between 500 to 2000 seconds. The streaming potential is then measured by two inert, glassy carbon electrodes immersed in surfactant solution and converted into a zetapotential by the software (LabVIEW, National Instruments).[13] The carbon electrodes are placed such that one is located upon the central axis of the spinning surface and another is located at a radial distance to the edge of the solution reservoir. While streaming potentials are instantaneously established in aqueous solutions, nonpolar solutions do not behave in the same way. Hence, the surface mount was spun up to 2000 seconds for the streaming potential to reach an equilibrium value due to the low conductivity of the surfactant solutions. The solution is continuously sparged with nitrogen gas to remove water from the solution prior to measurements. All solutions were maintained at a water content below 10 ppm according to a coulometric Karl-Fisher water titrator.

5.3 Results and Discussion

5.3.1 Effect of Surface Contact Time on Zeta Potential of AOT Doped Dodecane

The first series of experiments focused on the zeta potential of sodium AOT in dodecane and are shown in **Figure 5.1**.

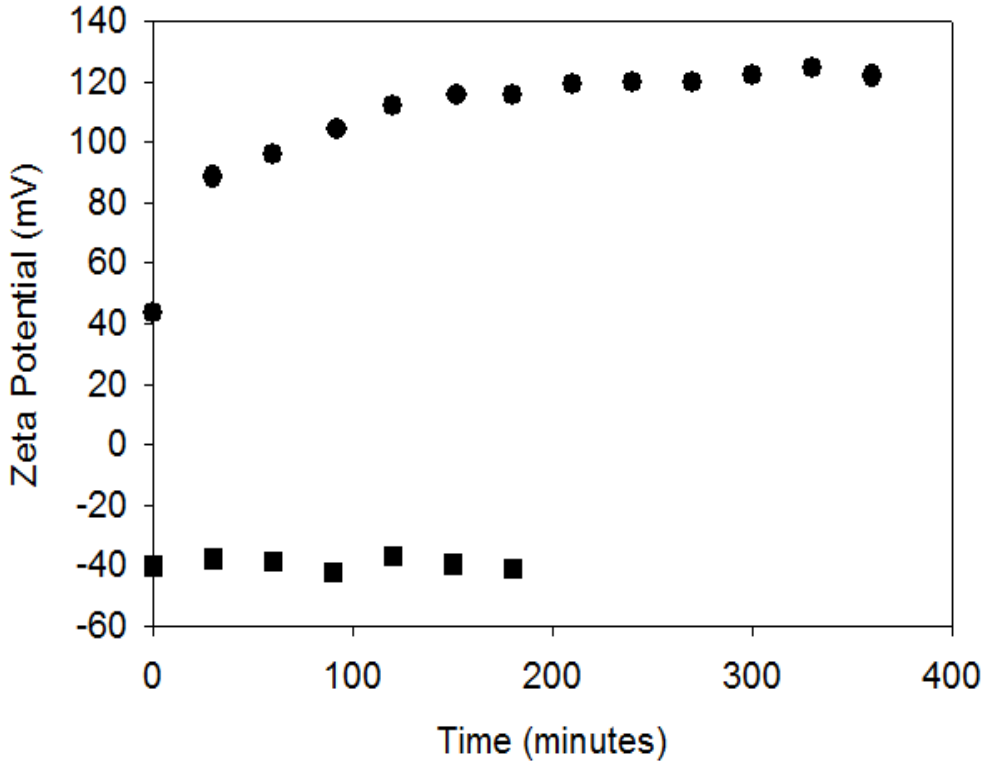

Figure 5.1. Zeta potential of 30mM AOT in dodecane on freshly cleaved mica (filled circles) and 10mM AOT in dodecane on fluoropolymer (filled squares) as a function of contact time between surfactant solution and surface.

Figure 5.1 displays the zeta potential for the mica and fluoropolymer surface for an AOT in dodecane solution. Mica and fluoropolymer surface behave radically different in response to contact with the AOT solution. In water, mica has a negative zeta potential because the potassium ions within mica are leached out by water. The positive potassium ions leave the mica surface and are dissolved into the bulk aqueous solution leaving a net negative zeta potential on the mica surface.[17] In contrast, the zeta potential of mica in AOT in a nonpolar solution is large and positive. Comparing with a similar study in the literature, AFM measurements between a mica particle and a planar mica surface immersed in an AOT/decane solution revealed a repulsive force between the particle and surface.[17] Thus, our experiment agrees with literature in that both experimental methods corroborate charging of the mica surface by AOT in nonpolar

media. However, the literature study concludes that the net charge of the AOT surfaces are negative from a phase analysis light scattering experiment (Zeta-PALS) indicating a small negative mobility of magnitude 10^{-10} m^2/Vs.[17]

In light of these differing results, it is useful to consider the experimental differences between the two methods. The experiments in **Figure 5.1** were performed under extremely low water conditions (less than 10 ppm) while the AFM experiments were conducted using untreated AOT stock solutions which are known to be hygroscopic (1wt. % water). Lack of water could would facilitate a positive zeta potential by preventing solvation of potassium ions from the mica surface. The Zeta-PALS experiments from literature were conducted on ground mica particles which may have considerably different surface chemistry than freshly cleaved mica sheets used in Zetaspin™ experiments. Another key difference between the two techniques is that for AFM experiments, the total volume of the apparatus was sufficiently small such that all charges are assumed to be around the mica particle and mica surface. Zetaspin™ experiments however require a large volume of surface solution such that there exists a bulk reservoir of solution to replenish any ions adsorbed onto the mica surface. Given the long time equilibration needed for the zeta potential to settle to a consistent value (~125 minutes) in **Figure 5.1**, there is likely some effect on zeta potential from the transport of ions from the bulk fluid onto the mica surface. Also shown in **Figure 5.1** is the zeta potential of AOT in dodecane on a fluoropolymer surface. Unlike mica surface, the fluoropolymer surface has a large negative zeta potential in AOT/dodecane. Furthermore, the zeta potential is established almost instantaneously after contact with the fluoropolymer surface.

5.3.2 Effect of Water Content on Zeta Potential of AOT Doped Dodecane

The effect of water exposure was also explored for both the mica and fluoropolymer surface and are shown in **Figure 5.2** and **Figure 5.3** respectively.

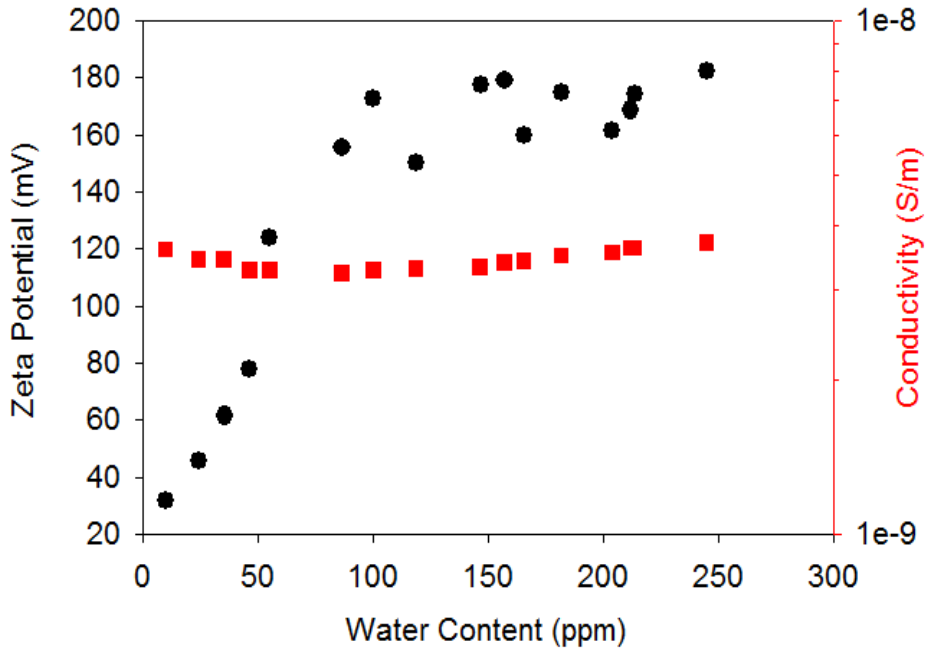

Figure 5.2. Zeta potential (filled circles) and conductivity (filled squares) of a 30 mM AOT in dodecane solution in contact with a mica surface. Water content strongly affects the zeta potential compared to conductivity.

Figure 5.2 plots the relationship between zeta potential and water content of solution as measured by the KF water titrator. For these measurements, a solution of AOT in dodecane was nitrogen sparged until the water content was below the measurable limit of the KF water titrator. Then, water was re-introduced into the solution via exposure to ambient humidity while the spindle mount was stationary. Water content and zeta potential measurements were taken at various time intervals and graphed in **Figure 5.2**. As seen in a previous study in the literature, water strongly affects the zeta potential of the mica surface but has much less effect on surfactant conductivity.[17] Given the hydrophilic nature of the mica surface and its change in surface charge with

increased water content, it is highly probable that the water is accumulating at the mica / solution interface. This is surprising as the response of the mica surface in aqueous solutions is solvation of potassium ions within the mica layers resulting in a net negative charge surface charge. In contrast, the role of water in charging of the mica surface in AOT doped dodecane is to facilitate positive surface charging. Another interesting effect of water is to introduce noise and irreproducibility in the measurement of the zeta potential. While the zeta potential in **Figure 5.1** asymptotes to a consistent value at long equilibration times, there is a ± 20 mV variance in the zeta potential at high water contents. Since zeta potential measurements are essential to analysis of impedance spectroscopy data, any measurement error in the zeta potential will propagate to the electrical properties derived from impedance spectroscopy. That is, an unsteady zeta potential arising from fluctuating water contents would complicate the conductivity and ionic strength analyses. Thus, water was removed during sample prep and impedance spectroscopy experiments described in Chapters 2 through 4. Zeta potential data as a function of water content for the fluoropolymer surface is shown in **Figure 5.3.**

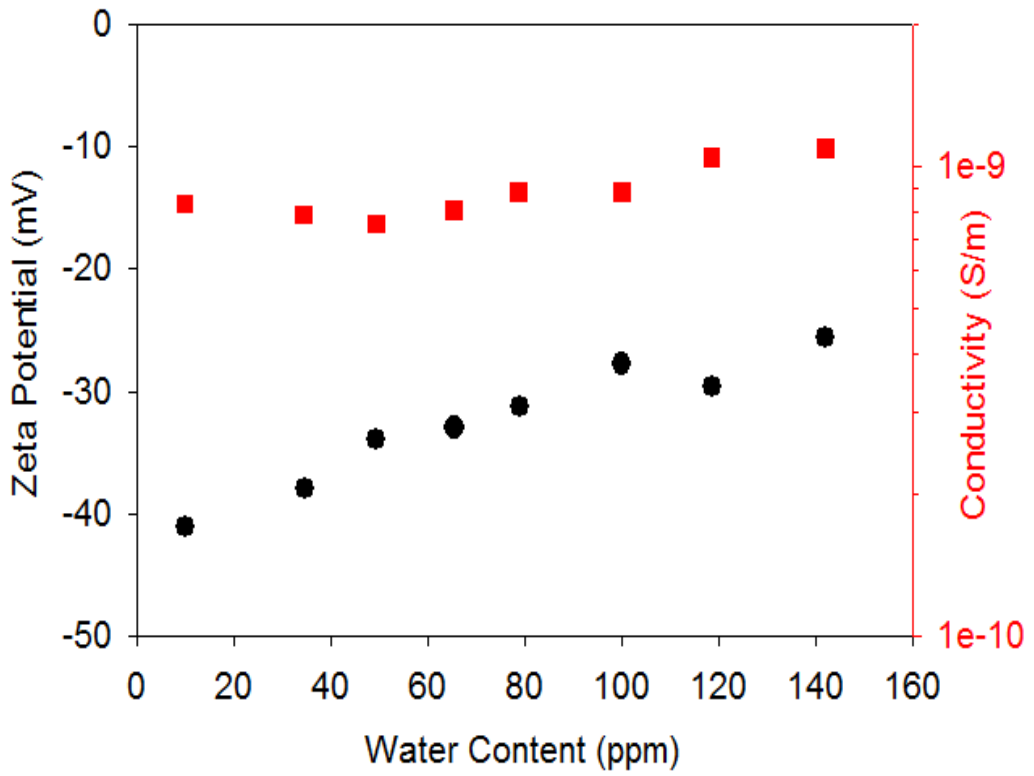

Figure 5.3. Zeta potential (filled circle) and conductivity (filled square) as a function of water content for fluoropolymer surface in AOT/dodecane solution. Water content strongly affects the zeta potential despite having negligible effect on the conductivity.

Figure 5.3 plots the zeta potential of the fluoropolymer surface in contact with the AOT doped dodecane solution. These measurements were taken in the same manner as the AOT/dodecane on mica measurements. An AOT/dodecane solution was sparged until the water content was below the detection limit of the KF water titrator. Then, water was slowly allowed back into the solution by exposing it to ambient humidity with conductivity and zeta potential measurements taken periodically throughout this process. The zeta potential of the fluoropolymer surface was determined to be moderately negative as confirmed by **Figure 5.1**. Unlike the mica surface, the introduction of water into the surface solution had a relatively weak effect on the zeta potential of the fluoropolymer surface. The water content also appeared to have a negligible effect on the conductivity of the AOT solution.

5.3.3 Zeta Potential of Fluoropolymer in AOT and AOT Analog Doped Dodecane

The mechanisms behind charging of the fluoropolymer surface in surfactant solutions is further explored and shown in **Figure 5.4**.

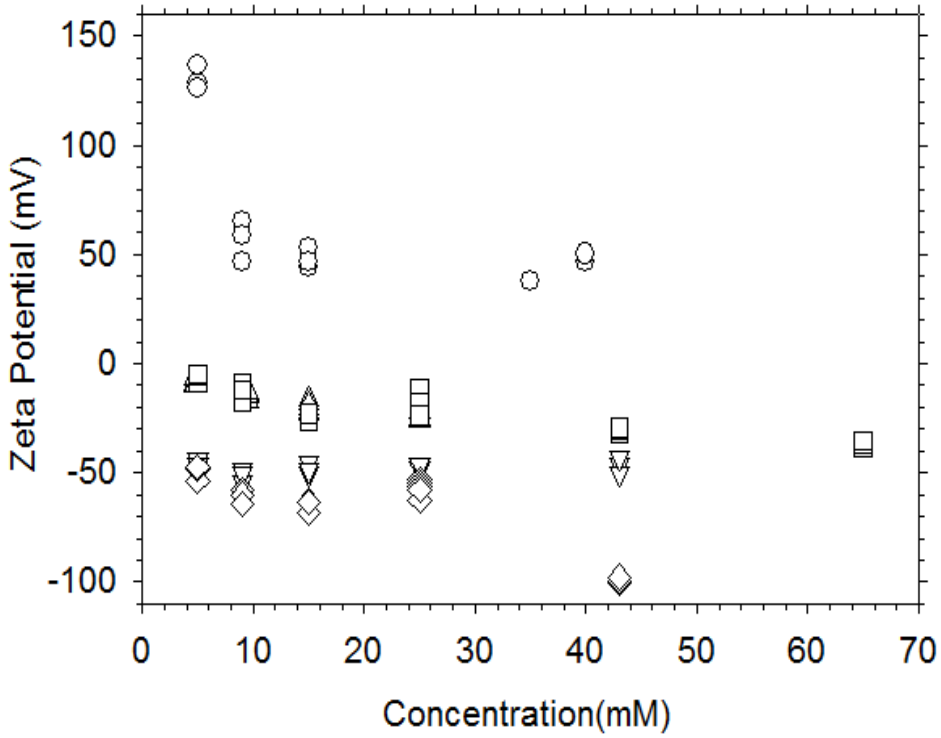

Figure 5.4. Zeta potential of the fluoropolymer surface as a function of surfactant concentration for $(C_8b)_2$-Glu-PTS (upright triangle), $(C_8b)_2$-Asp-PTS (downward triangle), sodium AOT (square), calcium AOT (diamond), and $(C_8b)_2$-Asp-COOH (circle).

The zeta potential of a variety of surfactant solutions in contact with the fluoropolymer surface is shown in **Figure 5.4**. The zeta potential of fluoropolymer is negative except when it is immersed in (C8b)2-Asp-COOH solutions. A proposed mechanism of surface charging was developed by Fowkes for polymeric adsorption in nonpolar liquids based on adhesion forces arising from acid-base interactions.[11] Behrens introduced a modification of this acid-base mechanism for charging of surfaces in surfactant doped nonpolar solutions.[18] In this mechanism, the surface and the surfactant are evaluated based on the work required to separate the surfactants from

the surface. This energy is termed the work of adhesion (W_{SL}) and is defined as the change in Helmholtz free energy per unit area of interface where

$$W_{SL} = W_{SL}^{LW} + W_{SL}^{AB} \quad 5.1)$$

W_{SL} is composed of the work due to Lifshitz-van der Waals (W^{LW}) attractive forces and work due to acid-base interactions (W^{AB}). These parameters are be rewritten as interfacial tensions between the solid and liquid phases such that

$$W_{SL} = 2(\gamma_S^{LW}\gamma_L^{LW})^{1/2} + 2(\gamma_S^-\gamma_L^+)^{1/2} + 2(\gamma_S^+\gamma_L^-)^{1/2} \quad (5.2)$$

Where γ_S^{LW} is the interfacial tension arising from the Lifshitz-van der Waals attractive forces for the solid, γ_L^{LW} is the interfacial tension arising from the Lifshitz-van der Waals attractive forces for the liquid, $2(\gamma_S^-\gamma_L^+)^{1/2}$is the ease of transferring an electron from the solid phase into the liquid phase, and $2(\gamma_S^+\gamma_L^-)^{1/2}$ is the ease of transferring a proton from the solid phase into the contacting liquid phase. Properties of the contacting solid γ_S^{LW}, γ_S^-, γ_S^+ can be derived from a variation of equation (5.2).

$$\gamma_R(1 + cos(\theta_{SR})) = 2(\gamma_S^{LW}\gamma_R^{LW})^{1/2} + 2(\gamma_S^-\gamma_R^+)^{1/2} + 2(\gamma_S^+\gamma_R^-)^{1/2} \quad (5.3)$$

where R denotes the reference fluid, γ_R, γ_R^{LW}, γ_R^-, γ_R^+, are interfacial parameters of the reference fluid obtained from literature, and θ_{SR} is the contact angle between the test surface and the reference fluid. Since there are three unknown solid parameters, contact angle between the solid and three reference fluid must be measured to deduce values for γ_S^{LW}, γ_S^-, γ_S^+. Next, interfacial parameters must be derived for the surfactant solution contacting the test surface. A variation of equation (5.2) is again constructed such that

$$\gamma_{RL} = \left[\left(\gamma_R^{LW}\right)^{\frac{1}{2}} + \left(\gamma_L^{LW}\right)^{\frac{1}{2}}\right]^2 + 2\left[\left(\gamma_R^{+}\right)^{\frac{1}{2}} - \left(\gamma_L^{+}\right)^{\frac{1}{2}}\right]\left[\left(\gamma_L^{-}\right)^{\frac{1}{2}} - \left(\gamma_R^{-}\right)^{\frac{1}{2}}\right] \quad (5.4)$$

where R denotes the reference fluid, L denotes the surfactant solution, and γ_{RL} is the interfacial tension between the surfactant solution and the reference fluid. Given that $\gamma_R, \gamma_R^{LW}, \gamma_R^{-}, \gamma_R^{+}$, are interfacial parameters of the reference fluid tabulated in literature, equation (5.4) can be solved for the properties of the surfactant solution $\gamma_L^{LW}, \gamma_L^{-}, \gamma_L^{+}$. Once the acid and base properties of the solid surface and surfactant solution are derived, values for $2(\gamma_S^{-}\gamma_L^{+})^{1/2}$ and $2(\gamma_S^{+}\gamma_L^{-})^{1/2}$ can be calculated and used to predict the sign of surface charging.

Applying this technique to the fluoropolymer data shown in **Figure 5.4**, $2(\gamma_S^{-}\gamma_L^{+})^{1/2}$ and $2(\gamma_S^{+}\gamma_L^{-})^{1/2}$ values can be derived where S is the fluoropolymer surface and L is the surfactant solution. These parameters would typically be calculated from reference fluids using the technique outlined in the preceding paragraph; however, for a qualitative assessment, they can also be found in the literature. Such values are shown in **Table 5.1**.

Table 5.1. Acid-base interfacial parameters for mica, fluoropolymer, and AOT from literature.

Sample	γ^+ (mJ/m^2)	γ^- (mJ/m^2)
Mica	45[19]	3[19]
Fluoropolymer	0.01[20]	0.1[20]
AOT	>0[10]	>0[10]

Fluoropolymer has more basic character than acidic character ($\gamma^- > \gamma^+$). Thus, it will tend to donate electrons and be positively charged in contact with a surfactant solution. Such is the case for the surfactant $(C_8b)_2$-Asp-COOH in **Figure 5.4**. In

contrast, all other zeta potentials in **Figure 5.4** indicate negative charging of the fluoropolymer surface. For acid-base mechanisms to predict a negative charge for the fluoropolymer surface, $\gamma_L^+ < 0.1\ \gamma_L^-$ where L is the surfactant solution. Examining the mica/AOT system, mica has more acidic than basic character ($\gamma^- < \gamma^+$). Thus it will tend to donate protons or be negatively charged in contact with a surfactant solution. For acid-base mechanisms to predict a positive charge for the mica surface, $\gamma_{AOT}^+ > 15\gamma_{AOT}^-$.

5.4 Conclusions

Existing zeta potential experiments in the literature use low purity commercial surfactants and do not actively exclude water from the sample. Zetaspin™ allows one to measure an electric field independent zeta potential in a low humidity, nitrogen rich environment. The synthesis methods in Chapters 3 and 4 are used to produce high purity surfactants with incremental changes in surfactant chemistry. The charging of mica and fluoropolymer by these surfactants is investigated using the Zetaspin™. Mica was determined to have different charging behavior than fluoropolymer. Mica surfaces required two hours of equilibration time with the surfactant solution to reach a steady zeta potential value. Furthermore, the mica surface was hygroscopic and the zeta potential of the surface increased with water content of the solution. In contrast, fluoropolymer surfaces were determined to reach a steady zeta potential value within minutes and had a steady zeta potential that was independent of solution water content. The acid-base mechanism for adhesion forces between the surfactant solution and the surface was used to rationalize charging of the mica and fluoropolymer surfaces. Such analyses could not predict the sign of charging of the surfaces indicating that additional mechanisms beyond acid-base interactions were responsible for surface charging of

mica and fluoropolymer in nonpolar liquids.

5.5 Acknowledgements

We thank Norman Gottron and Mason Risley at the Carnegie Mellon Nanofabrication Facility for the plasma deposition expertise and manufacturing of the C_4F_8 coating. Thanks to Bugra Ozutemiz and Dr. Burak Ozdoganlar at the mechanical engineering department at Carnegie Mellon for access and training on the white light interferometer. Another thank you to master's degree researcher JK Oh for some of the AOT on mica Zetaspin™ measurements. We also gratefully acknowledge financial support through NSF grant #1511619.

5.6 References

(1) Chen, Y.; Au, J.; Kazlas, P.; Ritenour, a; Gates, H.; McCreary, M. Electronic Paper: Flexible Active-Matrix Electronic Ink Display. *Nature* **2003**, *423* (6936), 136.

(2) Comiskey, B.; Albert, J. D.; Yoshizawa, H.; Jacobson, J. An Electrophoretic Ink for All-Printed Reflective Electronic Displays. *Nature* **1998**, *394* (6690), 253–255.

(3) Pearlstine, K.; Page, L.; El-Sayed, L. Mechanism of Electric Charging of Toner Particles in Nonaqueous Liquid with Carboxylic Acid Charge Additives. *J. imaging Sci.* **1991**.

(4) Hao, T. Electrorheological Fluids. *Advanced Materials*. 2001.

(5) Jones, S. A.; Martin, G. P.; Brown, M. B. Manipulation of Beclomethasone-Hydrofluoroalkane Interactions Using Biocompatible Macromolecules. *J. Pharm. Sci.* **2006**, *95* (5), 1060–1074.

(6) Morrison, I. D. Electrical Charges in Nonaqueous Media. *Colloids and Surfaces A: Physicochemical and Engineering Aspects*. 1993, pp 1–37.

(7) Smith, G. N.; Eastoe, J. Controlling Colloid Charge in Nonpolar Liquids with Surfactants. *Phys. Chem. Chem. Phys.* **2012**, 424–439.

(8) Lee, J.; Zhou, Z. L.; Alas, G.; Behrens, S. H. Mechanisms of Particle Charging by Surfactants in Nonpolar Dispersions. *Langmuir* **2015**, *31* (44).

(9) Parent, M. E.; Yang, J.; Jeon, Y.; Toney, M. F.; Zhou, Z. L.; Henze, D. Influence of Surfactant Structure on Reverse Micelle Size and Charge for Nonpolar Electrophoretic Inks. *Langmuir* **2011**, *27* (19), 11845–11851.

(10) Guo, Q.; Lee, J.; Singh, V.; Behrens, S. H. Surfactant Mediated Charging of Polymer Particles in a Nonpolar Liquid. *J. Colloid Interface Sci.* **2013**.

(11) Fowkes, F. M. Role of Acid-Base Interfacial Bonding in Adhesion. *J. Adhes. Sci. Technol.* **1987**.

(12) Lee, J.; Zhou, Z. L.; Behrens, S. H. Charging Mechanism for Polymer Particles in Nonpolar Surfactant Solutions: Influence of Polymer Type and Surface Functionality. *Langmuir* **2016**, *32* (19).

(13) Yezer, B. A. Determination of Charge Concentration in Surfactant Doped Nonpolar Liquids, Carnegie Mellon University, 2016.

(14) Yezer, B. A.; Khair, A. S.; Sides, P. J.; Prieve, D. C. Use of Electrochemical Impedance Spectroscopy to Determine Double-Layer Capacitance in Doped Nonpolar Liquids. *J. Colloid Interface Sci.* **2015**, *449*, 2–12.

(15) Haverstick, K. Fundamental Behavior of a Model Biomolecular Amphiphile System, University of Minnesota, 1999.

(16) Steytler, D. C.; Jenta, T. R.; Robinson, B. H.; Eastoe, J.; Heenan, R. K. Structure of Reversed Micelles Formed by Metal Salts of Bis(Ethylhexyl) Phosphoric Acid. *Langmuir* **1996**.

(17) Briscoe, W. H.; Horn, R. G. Direct Measurement of Surface Forces Due to Charging of Solids Immersed in a Nonpolar Liquid. *Langmuir* **2002**.

(18) Guo, Q.; Lee, J.; Singh, V.; Behrens, S. H. Surfactant Mediated Charging of Polymer Particles in a Nonpolar Liquid. *J. Colloid Interface Sci.* **2013**, *392* (1).

(19) Jurak, M.; Chibowski, E. Topography and Surface Free Energy of DPPC Layers Deposited on a Glass, Mica, or PMMA Support. *Langmuir* **2006**.

(20) Kraus, E.; Orf, L.; Heilig, M.; Baudrit, B.; Starostina, I.; Stoyanov, O. Characterization of Polymer Surfaces by the Use of Different Wetting Theories Regarding Acid-Base Properties. *Int. J. Polym. Sci.* **2017**.

Chapter 6 Conclusions

6.1 Conclusions

Surface charging by surfactant dopants in nonpolar liquids has been the impetus behind many emerging and new technologies such as electrophoretic displays,[1,2] prevention of petrochemical aggregation in tar sands,[3] and stabilization of pharmaceutical ingredients in drug delivery applications.[4] While the mechanisms of surfactant and surface charging in aqueous solutions have been well studied in the literature, the models and mechanisms in nonpolar liquids are developed on a limited surfactant or surface specific basis. The experimental and synthetic techniques outlined in this thesis expand the catalogue of surfactants available for study and demonstrate surfactant charging relationships not observed in the existing literature.

In Chapter 2, a charge suppression coating is introduced to the impedance spectroscopy technique. This coating improves the resolution and sample accessibility of impedance spectroscopy experiments. Both alternating and direct current experiments of surfactant doped nonpolar liquids note the problems caused by undesirable electrode surface charging. In DC experiments, this manifests as a “surface charge” that complicates the integration analysis necessary to derive the ionic strength.[5–8] In AC experiments, this effect is so severe that it completely prevents measurement of the ionic strength for certain surfactants or concentrations.[9] Through polymer polymerization of a C_4F_8 precursor, a passivating coating was created on the electrode surface such that adsorption phenomenon disappears from the impedance spectra. The coating is therefore vital to electrical measurements of surfactant doped nonpolar liquids because it ensures an electrochemically inert electrode surface.

Another significant contribution in Chapter 2 is the design and implementation of a sample preparation and impedance spectroscopy procedure that severely limits sample exposure to water. This was accomplished through a rigorous system of nitrogen spargers, glove bags, and Faraday cages to limit exposure to ambient humidity or actively remove water from the samples. Such measures also had the added benefit of preventing water bridging between spacer particles that resulted in a short circuit inside the impedance cell, a common source of experiment failure. Some hygroscopic surfactants such as AOT were also prone to this type of experiment failure as they actively absorbed moisture from the air during impedance spectroscopy runs. The water exclusion precautions were therefore instrumental in measurement of surfactants previously never studied using impedance spectroscopy.

Considerable theoretical modeling achievements were also accomplished in Chapter 2. Previous impedance spectroscopy spectra were analyzed using an equivalent circuit that included a complex phase element (CPE). Such analyses were problematic because there was no physical rationale for the CPE. CPE behavior is thought to arise from the non-uniformity of the gap distances between the impedance electrodes; however, the CPE broadly characterizes this behavior under a single ambiguous parameter α. Such characterizations are not representative of any physical charge transfer processes within the impedance cell and are instead only mathematical fitting parameters with no basis in reality. Through impedance measurements of a soldered circuit, some of the CPE behavior was discovered to arise from instrumental bias within the potentiostat. As a result, the EIS analysis technique introduced by Yezer was changed to a procedure that fit impedance extrema to exact analytical solutions

arising from the revised equivalent circuit with no CPE. Mathematical manipulation of the analytical solutions of the impedance spectra allowed one to derive a “universal curve” that were composed of all possible solutions predicted by the equivalent circuit model and Yezer’s transport model. Errors for derived conductivities and ionic strengths were then calculated through extrapolation of the data extrema to the universal curve.

In Chapter 3, we introduced a synthetic technique for production of high purity surfactants that allows for easy control of surfactant tail length, degree of branching, head group chemistry, and counterion composition. We then synthesized a series of AOT analogs were used to isolate specific structure-function relationships between surfactant structure and charging behavior. Determination of the ionic strength, conductivity, and charge carrier size of AOT analogs compared to commercial AOT indicated that surfactant tail length had minimal effect on surfactant charging. However, counterion size strongly correlated with surfactant ionic strength and hence surfactant conductivity. Such behavior is not predicted by the leading theory of surfactant charging in nonpolar liquids, charge fluctuation theory. The experiments indicated that charge fluctuation theory for reverse micelles should be amended with some consideration towards the counterion size and overall surfactant dissociation likelihood. Comparisons between the conductivity of AOT from literature and experimental AOT demonstrated that water had negligible effect on AOT conductivity in contrast to previous results from literature.[10,11] Such measurements also represented the first instance of electrical characterization of AOT in low water environments.

The surfactant synthesis technique in Chapter 4 was expanded upon in Chapter 5. Three different groups of surfactant structures were synthesized and measured with

impedance spectroscopy. The first group of surfactants were synthesized to have varying degrees of dissociability but otherwise similar surfactant chemistry. This was accomplished through head group modifications while maintaining the same tail chemistry. Solubility tests demonstrated a strong correlation between surfactant dissociability and nonpolar solvent solubility. As the head group dissociability increased, the surfactant became increasingly soluble in dodecane. A similar trend was found for ionic strength. Surfactant structures that had greater dissociability possessed larger ionic strengths in solution with dodecane. The next group of surfactants were synthesized to discern whether surfactant tail length and degree of branching impacted micelle charging and solubility in nonpolar liquids. Branching was determined to be a key attribute to surfactant solubility which correlated with other studies in the literature.[12] Surfactant branching increases the degree of curvature of the surfactant and therefore promotes charge micelle formation. Surfactants with long tails were also synthesized and resulted in the discovery of several surfactants that were soluble in dodecane but were nonconductive. Dye studies indicated that at least one of these surfactants did not form micelles despite its solubility in nonpolar liquids. The last group of surfactants evaluated the micelle charging differences between a univalent and divalent metallic counterion. Under dry conditions, the ionic strengths, charge carrier size, and conductivities of the two surfactants were comparable despite the difference in counterion charge; however, the divalent surfactant was much more hygroscopic than its univalent counterpart, and the divalent surfactant conductivity varied by orders of magnitude depending on the water content.

The focus of Chapter 5 was the surface charging of mica and fluoropolymer by

the surfactants synthesized in Chapters 3 and 4. Each surface had different surface charging properties. The zeta potential of mica was large and positive while the zeta potential of fluoropolymer was large and negative. Exposure to ambient humidity during the course of the measurement increased the zeta potential of the mica surface while having negligible effect on the fluoropolymer surface. The mica surface also required a longer period of time in contact with the surfactant solution to reach a steady zeta potential compared to fluoropolymer. The acid-base surface charging mechanism introduced by Fowkes and amended by Behrens was used to model the surface charging of both the fluoropolymer and mica surface.[13–16] Examining the acid-base properties of the surface and surfactant yielded interfacial parameters that predicts a negative charge on the mica surface and a positive charge on the fluoropolymer surface, the opposite of experimental observations. Such calculations indicated that there must be additional properties beyond acid-base chemistry of the surface and surfactant that is responsible for the charging of the mica and fluoropolymer surfaces in low water conditions.

6.2 Future Work

The impedance derived ionic strength and conductivities in this thesis have errors that are calculated from the discrepancy between the equivalent circuit and the experimental data. The discrepancy between the circuit model and the experimental data is likely due to error in the gap distance between electrodes. Ideally, the gap distance between electrodes should be directly measured in order to fit the impedance spectra with minimal error. This is challenging because there is not a single gap distance between the two electrodes but rather a distribution of gap distance. Such

behavior arises from the inherent surface roughness of the ITO coated glass electrodes as well as polydispersity of the spacer particles. Interference fringes can be seen on the fully assembled impedance cells which could be used to determine the distribution of gap distances using interferometry. Another method would be to assemble the impedance using the spacer particles and some sort of UV-curable gel in place of surfactant solution. After the cell is assembled, it should be placed under a UV light until the gel is hardened. Then the gap distance profile can be obtained from thickness measurements of the hardened gel.

Other methods of obtaining the size and number of charged micelles should also be explored. Light scattering with the aid of a polarizer could discern micelle shapes in addition to size. Other ways of obtaining charged micelle concentration such as TIRM or ATM could be pursued to confirm the Debye lengths measured by EIS. Alternately, electrophoretic light scattering could be used to discern charged micelles; however, the presence of equal numbers of oppositely charged micelles must be considered.

Additional surfactants can also be synthesized using the flexible synthetic techniques and ion exchanging procedures described in Chapter 3 and 4. A greater variety of soft, inorganic counterions should be synthesized to confirm the findings discussed in Chapter 3 and 4. Literature results indicate successful micelle assembly of imidizolium DEHP surfactant in nonpolar liquid. Now that the assembly of surfactants in low water environments have been established, it would be useful to compare those results to water added conditions. This could be accomplished by doping in controlled quantities of water and examining the effect on micelle assembly and charging through conductivity, DLS, and impedance spectroscopy measurements.

New classes of surfactants in additional to products of the synthetic methods described in this thesis should be investigated with EIS. A possible candidate is polymers especially block co-polymers. Experiments in the literature indicate that block co-polymers of poly(ethylene oxide), poly(propylene oxide), and poly(butylene oxide) were able to charge xylene by forming micelles.[17] The advantage of polymeric materials is that the length and chemical composition could be easily tailored through existing polymer chemistry methods. Another sample of interest is salts. Experiments in the literature demonstrate the charging of nonpolar liquids by salts under high electric fields.[18] Such experiments would be of great theoretical interest because it allows one to explore the nonlinear regime of the EIS method.

The addition of charged impurities into surfactant solutions would be the most direct method of raising the conductivity of nonpolar liquids. Rather than formulating surfactants that dissociate, it would be more efficient to design charged impurities that could then use surfactant micelles as vehicles for charge solubilization. For example, Span surfactants have high conductivities that are thought to come from charged impurities such as fatty acids arising from the decomposition of the surfactant itself.

6.3 References

(1) Chen, Y.; Au, J.; Kazlas, P.; Ritenour, a; Gates, H.; McCreary, M. Electronic Paper: Flexible Active-Matrix Electronic Ink Display. *Nature* **2003**, *423* (6936), 136.

(2) Comiskey, B.; Albert, J. D.; Yoshizawa, H.; Jacobson, J. An Electrophoretic Ink for All-Printed Reflective Electronic Displays. *Nature* **1998**, *394* (6690), 253–255.

(3) Nikakhtari, H.; Vagi, L; Choi, P.; Liu, Q.; Gray, M. R.; Univ, A. Solent Screening For Non-Aqueous Extraction of Alberta Oil Sands. *Can. J. Chem. Eng.* **2013**, *91* (6), 1153–1160.

(4) Jones, S. A.; Martin, G. P.; Brown, M. B. Manipulation of Beclomethasone-

Hydrofluoroalkane Interactions Using Biocompatible Macromolecules. *J. Pharm. Sci.* **2006**, *95* (5), 1060–1074.

(5) Karvar, M.; Strubbe, F.; Beunis, F.; Kemp, R.; Smith, N.; Goulding, M.; Neyts, K. Investigation of Various Types of Inverse Micelles in Nonpolar Liquids Using Transient Current Measurements. *Langmuir* **2014**, *30* (41), 12138–12143.

(6) Strubbe, F.; Verschueren, A. R. M.; Schlangen, L. J. M.; Beunis, F.; Neyts, K. Generation Current of Charged Micelles in Nonaqueous Liquids: Measurements and Simulations. *J. Colloid Interface Sci.* **2006**, *300* (1), 396–403.

(7) Beunis, F.; Strubbe, F.; Karvar, M.; Drobchak, O.; Brans, T.; Neyts, K. Inverse Micelles as Charge Carriers in Nonpolar Liquids: Characterization with Current Measurements. *Current Opinion in Colloid and Interface Science*. 2013, pp 129–136.

(8) Karvar, M.; Strubbe, F.; Beunis, F.; Kemp, R.; Smith, N.; Goulding, M.; Neyts, K. Charging Dynamics of Aerosol OT Inverse Micelles. *Langmuir* **2015**, *31* (40), 10939–10945.

(9) Yezer, B. A.; Khair, A. S.; Sides, P. J.; Prieve, D. C. Determination of Charge Carrier Concentration in Doped Nonpolar Liquids by Impedance Spectroscopy in the Presence of Charge Adsorption. *J. Colloid Interface Sci.* **2016**, *469*, 325–337.

(10) Eicke, H. F.; Borkovec, M.; Das-Gupta, B. Conductivity of Water-in-Oil Microemulsions: A Quantitative Charge Fluctuation Model. *J. Phys. Chem.* **1989**, *93* (1), 314–317.

(11) Michor, E. L.; Berg, J. C. Extension to the Charge Fluctuation Model for the Prediction of the Conductivity of Apolar, Reverse Micellar Systems. *Langmuir* **2012**, *28* (45), 15751–15755.

(12) Nave, S.; Eastoe, J.; Heenan, R. K.; Steytler, D.; Grillo, I. What Is so Special about Aerosol-OT? 2. Microemulsion Systems. *Langmuir* **2000**, *16* (23), 8741–8748.

(13) Fowkes, F. M. Role of Acid-Base Interfacial Bonding in Adhesion. *J. Adhes. Sci. Technol.* **1987**.

(14) Lee, J.; Zhou, Z. L.; Alas, G.; Behrens, S. H. Mechanisms of Particle Charging by Surfactants in Nonpolar Dispersions. *Langmuir* **2015**, *31* (44).

(15) Guo, Q.; Lee, J.; Singh, V.; Behrens, S. H. Surfactant Mediated Charging of Polymer Particles in a Nonpolar Liquid. *J. Colloid Interface Sci.* **2013**, *392* (1).

(16) Lee, J.; Zhou, Z. L.; Behrens, S. H. Charging Mechanism for Polymer Particles in

Nonpolar Surfactant Solutions: Influence of Polymer Type and Surface Functionality. *Langmuir* **2016**, *32* (19).

(17) Alexandridis, P.; Andersson, K. Reverse Micelle Formation and Water Solubilization by Polyoxyalkylene Block Copolymers in Organic Solvent. *J. Phys. Chem. B* **1997**, *101* (41), 8103–8111.

(18) Pontiga, F.; Castellanos, A. Electrical Conduction of Electrolyte Solutions in Nonpolar Liquids. *IEEE Trans. Ind. Appl.* **1996**, *32* (4), 816–824.

Chapter 7 Appendix

7.1 Universal Curve

Error bars for EIS measurements were derived from the universal curve shown in **Figure 7.1**.

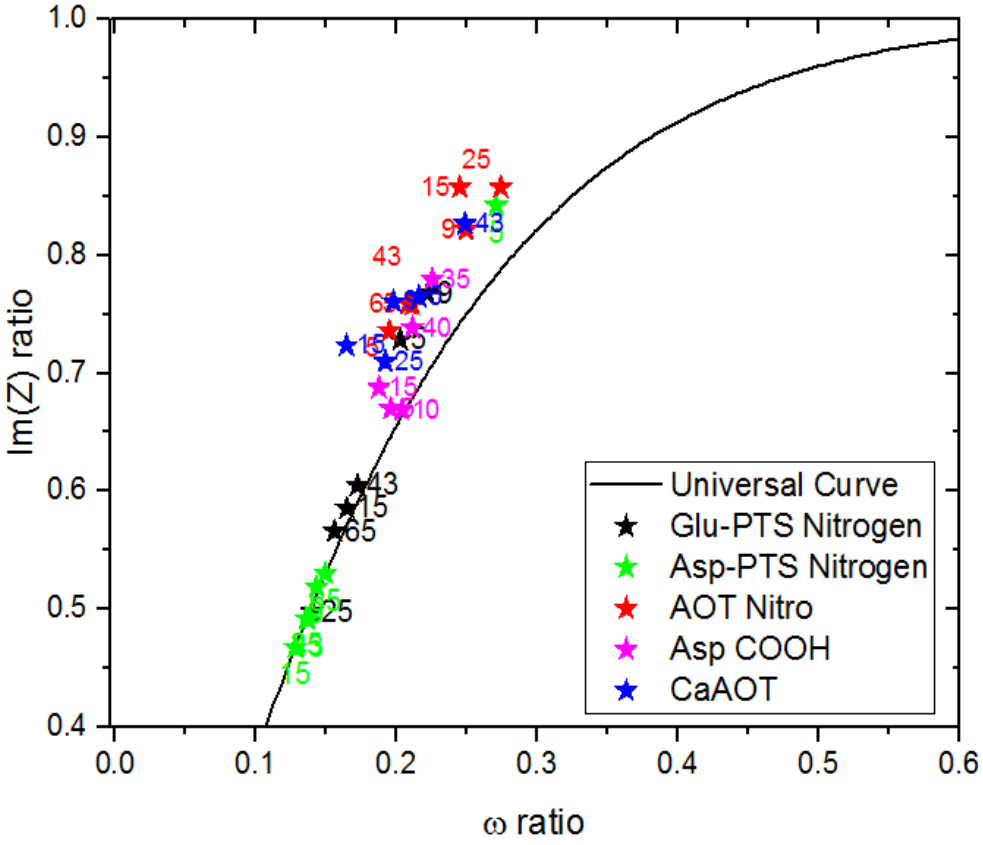

Figure 7.1. Universal curve and experimental Im(Z) and ω ratio for surfactants in this work.

The universal curve shown in **Figure 7.1** is derived from plotting $r_{Im(Z)}$ from equation (2.18) and r_ω from equation (7.1) for all possible c and b values.

$$r_\omega = \frac{\omega_{max}}{\omega_{min}} = \sqrt{\frac{1-4[(2c+1)b+c]-\sqrt{1-16[(2c+1)b+c]}}{1-4[(2c+1)b+c]+\sqrt{1-16[(2c+1)b+c]}}} \tag{7.1}$$

where c and b are as defined in Chapter 2, ω_{max} is the frequency of the local maxima in the EIS spectra, ω_{min} is the frequency of the local minima in the EIS spectra. All possible

solutions of the equivalent circuit shown in **Figure 2.2** lie on the universal curve. As a result, error bars for all EIS data in this thesis was determined through extrapolation back to the universal curve. First, the double layer capacitance was derived from the experimental $r_{Im(Z)}$ and equation (2.18). Next, the double layer capacitance was derived from the experimental r_{ω} and equation (7.1). The final double layer capacitance was calculated as the average and standard deviation of both methods. The experimental ratios shown in **Figure 7.1** begin to deviate from the universal curve at r_{ω} values of 0.2 and larger. The experimental data appear to be clustered in such a way that the data follows its own curve.